

LARGE AREA CZOCHRALSKI SILICON

Texas Instruments Report No. 03-77-23

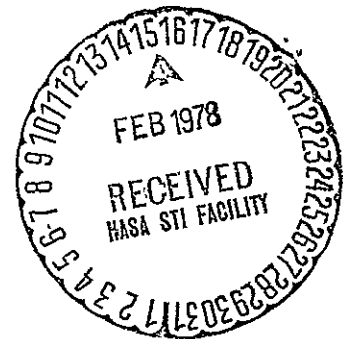
Final Report

Samuel N. Rea
Paul S. Gleim

April 1977

JPL Contract No. 954475

Texas Instruments Incorporated
P.O. Box 5012
Dallas, Texas 75222



This work was performed for the Jet Propulsion Laboratory, California Institute of Technology, under NASA Contract NAS7-100 for the U.S. Energy Research and Development Administration, Division of Solar Energy.

The JPL Low-Cost Silicon Solar Array Project is funded by ERDA and forms part of the ERDA Photovoltaic Conversion Program to initiate a major effort toward the development of low-cost solar arrays.

(NASA-CR-155590) LARGE AREA CZOCHRALSKI
SILICON Final Report (Texas Instruments, Inc.) 151 p HC A08/MF A01 CSCL 10A
N78-16441
G3/44 04184
Unclass

This report contains information prepared by Texas Instruments under a JPL subcontract. Its content is not necessarily endorsed by the Jet Propulsion Laboratory, California Institute of Technology, the National Aeronautics and Space Administration or the Energy Research and Development Administration.

ABSTRACT

The major purpose of this program was to determine the overall cost effectiveness of the Czochralski process for producing large-area silicon. To this end, the feasibility of growing several 12-cm diameter crystals sequentially at 12 cm/h during a furnace run and the subsequent slicing of the ingot using a multiblade slurry saw were investigated. The goal of the wafering process was a slice thickness of 0.25 mm with minimal kerf. A slice + kerf of 0.56 mm has been achieved on 12-cm crystal using both 400 grit B₄C and SiC abrasive slurries.

Crystal growth experiments were performed at 12-cm diameter in a commercially available puller with both 10 and 12-kg melts. Several modifications to the puller hot zone were required to achieve stable crystal growth over the entire crystal length and to prevent crystallinity loss a few centimeters down the crystal. The maximum practical growth rate for 12-cm crystal in this puller design was 10 cm/h, with 12-14 cm/h being the absolute maximum range at which melt freeze occurred.

A nugget polysilicon feeder was fabricated, assembled, and successfully tested on several multicharge runs. A grow yield of 93.5% was achieved in one 12-cm run, but not all was good, single crystal growth. Excessive oxide and carbon contamination in the nugget melts contributed to crystal growth problems.

A number of 12-cm crystals were sawed in the multiblade slurry saw. A 100% saw yield was obtained with B₄C abrasive at a slice + kerf of 0.56 mm and an average cutting rate of 6.1 mm/h. Silicon carbide abrasive has demonstrated 3-5 mm/h sawing rates on 12-cm crystal, although yields have run lower (73%) than those with B₄C at the 0.56 mm dimension. A slightly thicker slice, 0.30 mm, can be sawed with SiC abrasive at 100% yield.

Experiments in laser scribing silicon wafers into hexagons showed that a 10-W YAG laser can penetrate 0.2 mm at a scribe rate of 10 cm/s. Much higher writing rates on the order of 30-40 cm/s can penetrate 0.05 mm which is sufficient for scribe-and-break of 0.25-mm slices.

Czochralski economics were examined using realistic estimates of technical parameters and a sheet cost in the \$45/m² area is indicated for a semicontinuous puller in the early 1980 time frame. This represents an add-on cost (exclusive of polysilicon) of around \$30/m². To impact sheet cost in late 1970s, a multicharge growth mode is all that is technically possible and a sheet cost of \$55/m² is forecast.

TABLE OF CONTENTS

<i>Section</i>	<i>Title</i>	<i>Page</i>
I.	INTRODUCTION	1
II.	TECHNICAL DISCUSSION	5
A.	Crystal Growth	5
1.	Thermal Modeling	5
2.	Pull Rate Experiments	16
3.	Multicharge Analysis	19
4.	12-cm Growth	22
5.	Multicharge Process	25
B.	Crystal Slicing	29
1.	Introduction	29
2.	Experimental	30
3.	Saw Blade Mechanics	65
a.	Torsional Rigidity	66
b.	Buckling Load	67
c.	Blade Vibration	72
4.	Sawing Summary	73
C.	Characterization	76
1.	Crystal	76
2.	Slice Thickness, Bow, and Taper	76
3.	Saw Damage Depth	77
4.	Cell Fabrication	83
D.	Wafer Shaping	83
1.	Laser Scribing	83
2.	Edge Beveling	84
E.	Economic Modeling	84
1.	Crystal Growth Cycle Times	91
a.	Single Charge (12-kg Crucible)	91
b.	Single Charge (18-kg Crucible)	91
c.	Multicharge (Three Crystals)	92
d.	Semicontinuous (Three Crystals)	92
2.	Crystal Growth Cost Assumptions	93

PRECEDING PAGE BLANK NOT FILMED

TABLE OF CONTENTS (Continued)

<i>Section</i>	<i>Title</i>	<i>Page</i>
II.	E. 3. Crystal-Growth-Costs	94
	a. Single Charge (12-kg Crucible)	94
	b. Single Charge (18-kg Crucible)	95
	c. Multicharge (Three Crystals)	96
	d. Semicontinuous (Three Crystals)	97
	e. Crystal Cost Discussion	97
	4. Crystal Slicing Cycle Time	100
	5. Crystal Slicing Cost Assumption	102
	6. Crystal Slicing Costs	103
	a. Baseline Process	103
	b. Slicing Cost Discussion	103
	7. Other Costs	106
	a. Crystal Grind	106
	b. Wafer Clean	107
	c. Laser Scribe	108
	d. Edge Beveling	109
	8. Czochralski Sheet Cost	110
III.	CONCLUSIONS AND RECOMMENDATIONS	115
IV.	NEW TECHNOLOGY	117
V.	REFERENCES	119

APPENDICES

A.	THERMAL PROPERTY DATA	A-1
B.	CRYSTAL THERMAL CONVECTION	B-1
C.	METHOD OF COMPUTING RADIATION VIEW FACTORS FOR CYLINDRICAL GEOMETRIES	C-1
D.	MULTIBLADE SAWING RATES WITH CRYSTAL ROTATION	D-1
E.	SAW BLADE MECHANICAL PROPERTIES	E-1
F.	PULLER HOT ZONE COSTS	F-1
G.	CRYSTAL GROWTH POWER REQUIREMENTS	G-1
H.	SELECTED METRIC CONVERSION FACTORS	H-1

LIST OF ILLUSTRATIONS

<i>Figure</i>	<i>Title</i>	<i>Page</i>
1.	Typical Czochralski Silicon Puller	2
2.	Czochralski Crystal Thermal Model	6
3.	Silicon Pull Rates Predicted by Various Models	9
4.	Experimentally Determined Crucible Side Temperature as a Function of Melt Level for a 12-kg Crucible	12
5.	Theoretical Pull Rates for a 12-kg Crucible Czochralski Furnace	13
6.	Theoretical Crystal Axial Temperature Profiles	14
7.	Effects of Puller Interior Ambient Conditions on Pull Rate	14
8.	Effect of Crucible Radius on Pull Rate	15
9.	Influence of the Crucible Liner Emittance (Side Heat Shields) on Pull Rate	16
10.	Crystal Cooling Coil Configuration	17
11.	Theoretical Influence of Crystal Cooling Coil Position on Pull Rate	18
12.	Technique for Hot-Charging on a Czochralski Puller	26
13.	Silicon Kerf Volume versus Blade Travel as a Function of Blade Load	30
14.	Kerf Volume versus Blade Travel as a Function of Blade Speed	32
15.	Slurry-Sawing Three 5.0-cm Crystals Simultaneously	33
16.	Simultaneous Sawing of Three 5-cm Silicon Crystals	33
17.	Three-Crystal Slurry Sawing Experimental Results	35
18.	Boron Carbide Abrasive Slurry Sawing Results	36
19.	Effect of Slurry Flow Rate on Silicon Cutting Rate	38
20.	Crystal Spinner Alignment Fixture	41
21.	Crystal Spinning System	42
22.	SEMs of New and Used 400-Grit B ₄ C Abrasive	45
23.	SEMs of New and Used 400-Grit SiC Abrasive	46
24.	SEM of Blade from Experiment 15 — 400-Grit B ₄ C (500X)	47
25.	SEM (500X) of Blade After Cutting 7.6-cm Silicon Crystal Using SiC-PC Oil Slurry (Blade from Experiment 1)	47
26.	Experimental Slurry Sawing Results	48
27.	Photomicrographs of Diamond Blade Cutting Surface (240X)	51
28.	Slice From Experiment 20 Cut with Diamond-Plated Blades	52
29.	Surfaces of Both Sides of a Slice from Experiment 21	52

ORIGINAL PAGE IS
OF POOR QUALITY

LIST OF ILLUSTRATIONS (Continued)

<i>Figure</i>	<i>Title</i>	<i>Page</i>
30.	Experiment 16 — Sawing a 12-cm Crystal	56
31.	12-cm Slices from Experiment 26 After Slice Cleanup	57
32.	Cross Section From Experiment 30	60
33.	Experiment 32	62
34.	Model of a Thin Blade Undergoing Lateral Buckling Instability	65
35.	Theoretical Maximum Loads of Multiblade Saw Blades	69
36.	Diamond-Plated Blade Showing Evidence of Buckling	70
37.	Blade Problem Catalog	71
38.	Blade Misalignment Sufficient to Cause Buckling	71
39.	Effect of Blade Wear on the Critical Buckling Load	72
40.	Effects of Multiblade Saw Slurry Parameters on Silicon Cutting Rates	73
41.	Multiblade Saw Silicon Cutting Rates	75
42.	Talysurfs from Experiment 13 — 400-Grit B ₄ C Abrasive, 2.4 N/Blade Load	78
43.	Talysurfs from Experiment 16 — 400-Grit B ₄ C Abrasive, 2.0 N/Blade Load	79
44.	7.6-cm Diameter Sawed Slice Prepared for Transmission X-ray Topography	80
45.	Transmission X-ray Topography of a Step-Etched Slice	81
46.	Computer Printout of the Transmission X-ray Topograph	82
47.	Laser Scribed Slices	85
48.	Photomicrographs of Laser Scribed Silicon Slices — Continuous Mode	86
49.	Cross Section of Line Laser Scribed at 5.1 cm/s (300X)	87
50.	Laser Shaping Rate of 1 cm/s	88
51.	Laser Shaping Rate of 5 cm/s	89
52.	Laser Shaping Rate at 10 cm/s	90
53.	Czochralski Silicon Costs	98
54.	Silicon Crystal Cost	99
55.	Silicon Crystal Costs as a Function of Pull Rate	100
56.	Variation of Semicontinuous Growth Costs with the Number of Crystals/Run	101
57.	Influence of Crystal Length/Pull on Semicontinuous Growth Costs	101
58.	Multiblade Slurry Sawing Costs	104
59.	Effect of Sawing Rate on Multiblade Slurry Sawing Costs	105
60.	Czochralski Silicon Sheet Cost	111
61.	Czochralski Silicon Sheet Cost Exclusive of Polysilicon	111
62.	Czochralski Silicon Sheet Cost	112
63.	Czochralski Silicon Sheet Cost Exclusive of Polysilicon	113

LIST OF TABLES

<i>Table</i>	<i>Title</i>	<i>Page</i>
1.	12-cm Crystal Summary	23
2.	Multicharge Crystal Pulls	27
3.	Slurry Sawing Experiment Summary	31
4.	Slurry Sawing Experiment Summary	31
5.	Slurry Sawing Experiment Summary	34
6.	Slurry Sawing Experiment Summary	34
7.	Slurry Sawing Experiment Summary	39
8.	Slurry Sawing Experiment Summary	39
9.	Slurry Sawing Experiment Summary	40
10.	Slurry Sawing Experiment Summary	40
11.	Slurry Sawing Experiment Summary	44
12.	Slurry Sawing Experiment Summary	44
13.	Slurry Sawing Experiment Summary	50
14.	Slurry Sawing Experiment Summary	50
15.	Slurry Sawing Experiment Summary	53
16.	Slurry Sawing Experiment Summary	53
17.	Slurry Sawing Experiment Summary	55
18.	Slurry Sawing Experiment Summary	55
19.	Slurry Sawing Experiment Summary	58
20.	Slurry Sawing Experiment Summary	58
21.	Slurry Sawing Experiment Summary	63
22.	Slurry Sawing Experiment Summary	63
23.	Slurry Sawing Experiment Summary	64
24.	Slurry Sawing Experiment Summary	64
25.	Diamond-Plated Blade Cutting Rates	74
26.	12-cm Crystal Characterization	77
27.	12-cm Radial Resistivity Gradients	77

SECTION I INTRODUCTION

Silicon crystal pulled by the Czochralski technique (Cz silicon) provides over 90% of the single crystal wafers utilized by the worldwide semiconductor industry. This large market base has resulted in continual improvements over the years in Cz silicon technology. Concurrently, the average crystal diameter increased to the current industry standard of 7.6 cm with 10-cm wafers becoming an established trend and 12-cm and larger wafers available in evaluation quantities. Conceptually, there are few problems envisioned in growing even larger diameter crystal although there undoubtedly is an upper limit imposed by crucible size, puller hot zone design common to current commercial furnaces, and technical problems in slicing huge crystals. From a practical standpoint, wafer diameters in the 10 to 12-cm range are attractive at present for terrestrial solar cells since this diameter range is compatible with existing Cz furnaces and processing equipment and at 12.5% AM1 such cells have outputs around 1 to 1.4 W. This power output offers a convenient building block for subsequent assembly of cells into modules, panels, and arrays.

Figure 1 depicts a Czochralski crystal being pulled from its melt in a conventional furnace. The crucible, crucible liner, melt, heater, heat shield assembly, and attendant insulation in the lower chamber are collectively called the "hot zone." The crystal is pulled into the upper chamber and is removed from a large door in this chamber. During a run, the puller interior is maintained at 10-30 mm Hg absolute pressure with argon used as a purge gas. Counterrotation is employed for the crucible and seed shaft at nominal rates of 12 and 18 rpm respectively.

A major technical bottleneck in achieving cost-effective large-area Cz silicon lies in the wafering process which results in considerable material waste. Crystal ingot is sliced at present almost exclusively by ID saws. The kerf loss produced by these saws on 7.6-cm crystal is typically 0.31 mm and there appears little possibility of reducing this figure; in fact, the kerf probably will increase at larger crystal diameters due to the need for stiffer blades to maintain slice bow and taper at acceptable levels. For solar silicon wafers required around 0.25-mm thick, the kerf loss using conventional sawing represents over half the crystal ingot. The economic impact of the kerf will be lessened considerably, however, with reduced raw material polycrystalline silicon costs, particularly the advent of \$10/kg polysilicon.

In addition to minimizing kerf, it is necessary to increase sawing productivity to lower wafering costs. ID saws produce approximately 25 7.6-cm wafers per hour and can be expected to slice around 15 12-cm slices per hour. The actual productivity figures are highly dependent on

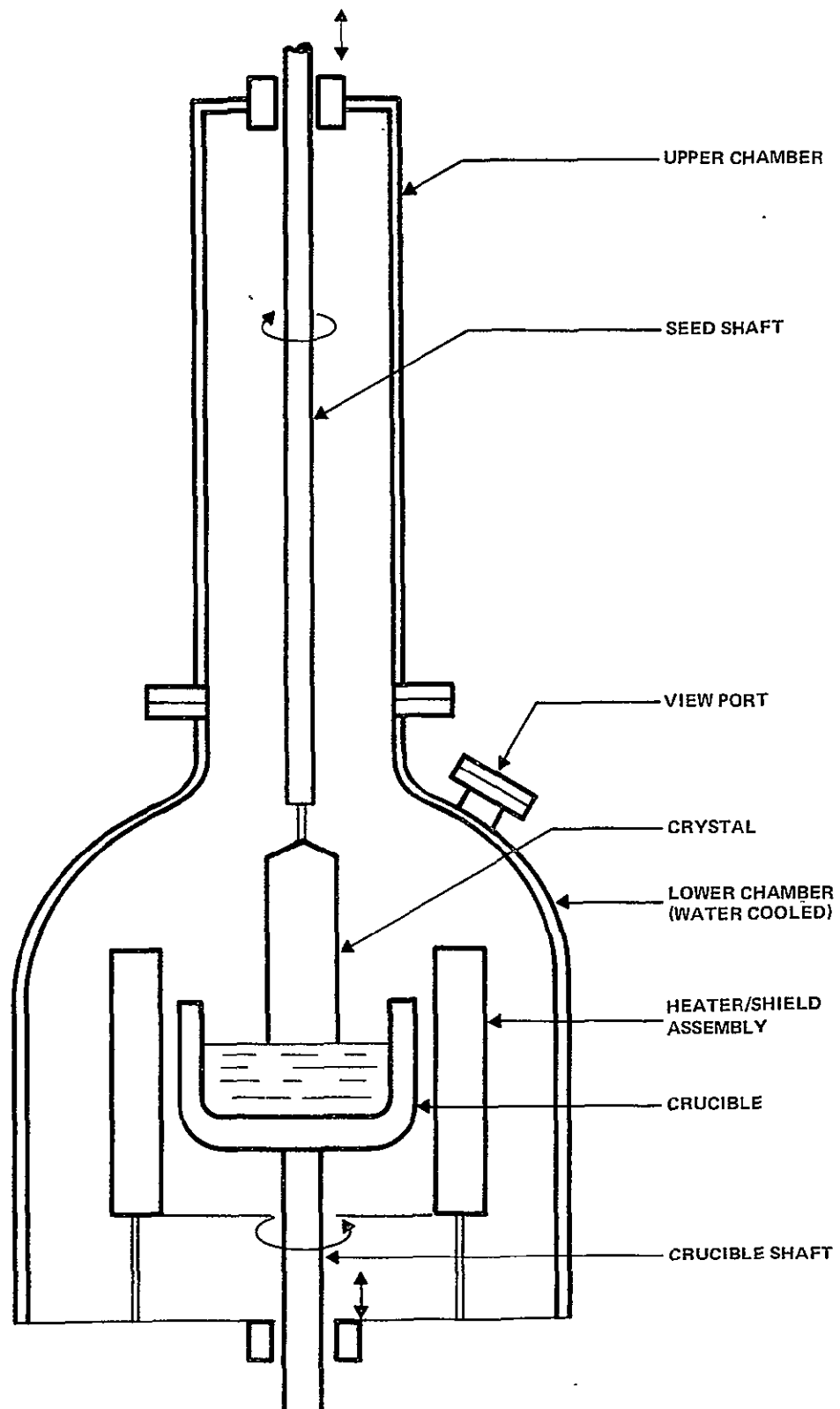


Figure 1. Typical Czochralski Silicon Puller

allowable bow, taper, slice thickness, and surface damage depth; parameters which have not been established firmly with regard to producing efficient solar cells. Nevertheless, economic modeling indicates that a substantial increase in slicing productivity along with a decrease in materials costs over that of ID sawing is needed to achieve an acceptable wafering cost.

The current market price of as-sawed 7.6-cm Cz slices for solar cell applications is around \$700/m². This price is at least a factor of 20 too high to meet the 1980's solar array cost goals. Detailed economic modeling of the Czochralski process indicates that this factorial cost improvement can be approached provided:

- 1) Polysilicon cost is reduced to the \$10/kg level
- 2) Semicontinuous crystal pulling is achieved, or, at least a multicharge process capable of producing four crystals per run
- 3) Minimum crystal diameter is 12 cm
- 4) Puller design is optimized to allow pull rates approaching theoretical limits
- 5) Crystal grinding is not required
- 6) Multiblade slurry saws can be scaled up 50%
- 7) Saw blade costs can be reduced 80%.

Add-on costs of Cz silicon are split roughly 50-50 between crystal growth and wafering so both areas merit close attention to effect cost savings. _____

SECTION II TECHNICAL DISCUSSION

A. CRYSTAL GROWTH

1. Thermal Modeling

The maximum Czochralski crystal pull rate, V_{\max} , assuming a flat growth interface and no radial temperature gradients is given by:

$$V_{\max} = - \frac{k}{h_{if} \rho} \left(\frac{dT}{dx} \right) \quad (1)$$

where

k = thermal conductivity

h_{if} = heat of fusion

ρ = crystal density

(dT/dx) = temperature gradient in the solid crystal at the growth interface

The physical parameters k and ρ in Eq. (1) are evaluated for the crystal at the melting point. The maximum pull rate according to Eq. (1) depends only on the temperature gradient at the growth interface and in order to predict V_{\max} , it is necessary, therefore, to determine (dT/dx) .

Figure 2 depicts the thermal model assumed in this investigation.

The temperature in a crystal being pulled from its melt is described by the equation:

$$\frac{\partial}{\partial x} \left(k \frac{\partial T}{\partial x} \right) - V \rho c \frac{\partial T}{\partial x} - \frac{2h}{r} (T - T_a) - \frac{2}{r} q_R = \rho c \frac{\partial T}{\partial t} \quad (2)$$

PRECEDING PAGE BLANK NOT FILMED

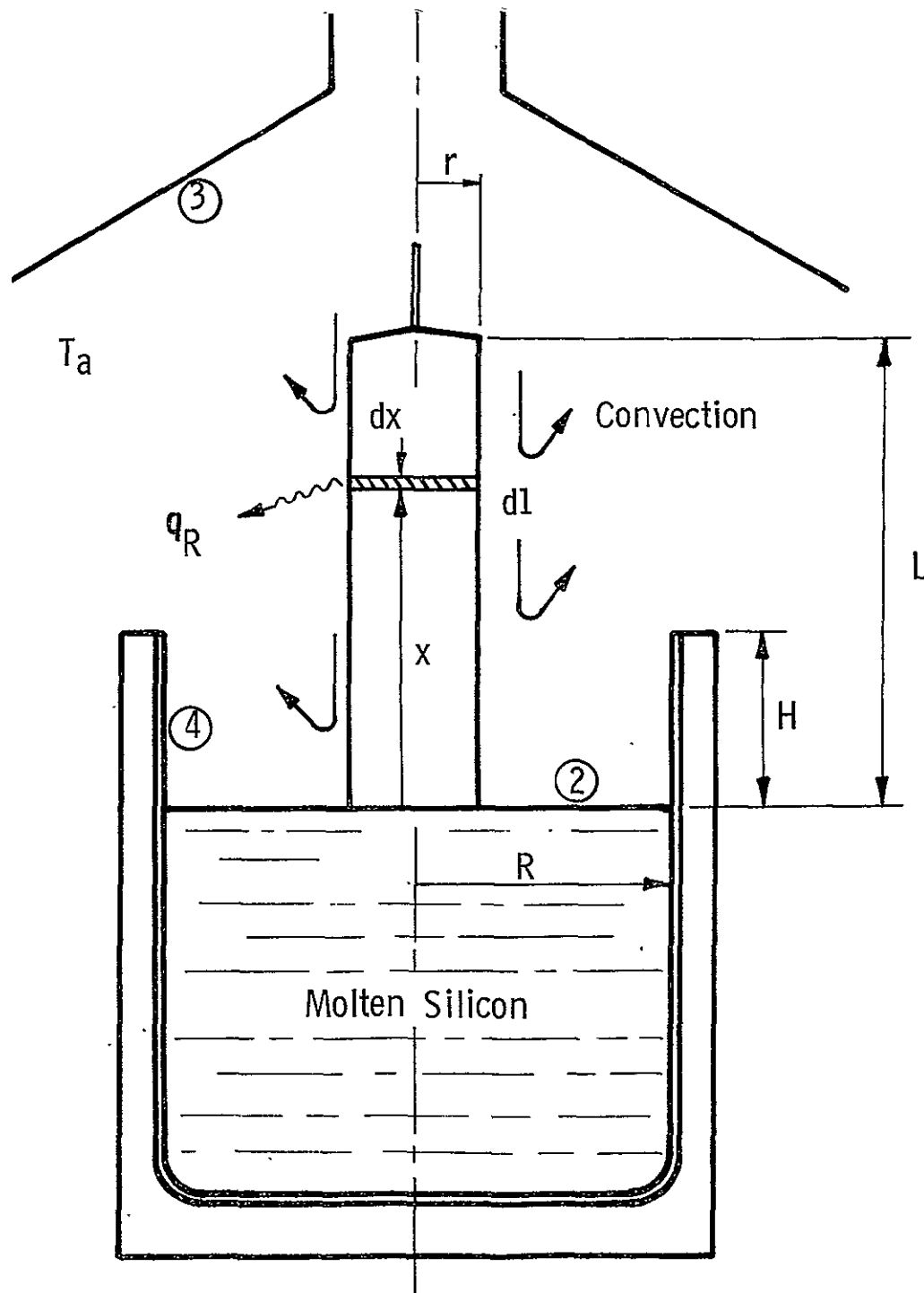


Figure 2. Czochralski Crystal Thermal Model

in which

T = crystal temperature at x

k = crystal thermal conductivity

V = pull rate

ρ = crystal density

c = specific heat

h = thermal convective coefficient

r = crystal radius

T_a = average furnace interior ambient temperature

q_R = radiation heat flux from the crystal at x

t = time

Boundary conditions on Eq. (2) are:

$$x = 0: T = T_m \quad (3)$$

$$x = L: \frac{dT}{dx} = -\frac{\epsilon\sigma}{k} (T^4 - T_a^4) - \frac{h}{k} (T - T_a) \quad (4)$$

where

T_m = melting point

ϵ = emissivity

σ = Stefan-Boltzmann constant

The initial condition for Eq. (2) is:

$$t = 0: T = T_m \quad (5)$$

ORIGINAL PAGE IS
OF POOR QUALITY

The major assumptions made in deriving Eq. (2) are:

1. The crystal temperature varies only in the axial or x-direction.
2. The crystal diameter is constant.
3. The pull rate, V , is constant.
4. Crystal density and specific heat are constant with temperature.

In Eq. (2) the first term represents axial conduction up the crystal; the second term describes the rate at which heat is transported due to the crystal motion; the third term represents thermal convection from the crystal's surface; the fourth term involves the thermal radiation from the crystal surface; and the right-hand side is the transient change in temperature at position x relative to the melt level due to the constantly increasing crystal length, L . Boundary condition (3) states that the crystal temperature at the growth interface is the melting point and Eq. (4) relates the temperature gradient at the seed end to the thermal radiation and convective heat transfer from the crystal top. The initial condition, Eq. (5), states that the crystal at the beginning (vanishingly short) is everywhere at the melting point. The radiative term q_R is proportional to temperatures to the fourth power and can have a variety of values depending upon the assumptions employed and these will be discussed below.

Equation (2) cannot be solved in closed form due to the inherent nonlinearities. In fact, it is extremely difficult to solve numerically for a material such as silicon which has a high melting point and, therefore, can span many hundreds of degrees over a fairly short length. Consequently, various simplifying assumptions are made in order to obtain solutions.

An order-of-magnitude analysis on Eq. (2) indicates that the transient term, $\partial T / \partial t$, is approximately 1% as large as the conduction term. Therefore, setting $\partial T / \partial t = 0$ results in the ordinary differential equation:

$$\frac{d}{dx} \left(k \frac{dT}{dx} \right) - V \rho c \frac{dT}{dx} - \frac{2h}{r} (T - T_a) - \frac{2}{r} q_R = 0 \quad (6)$$

For crystals grown in vacuum, the convective coefficient h vanishes and for small diameter crystals pulled at low growth rates, the term $V \rho c (dT/dx)$ can be neglected.¹ Also, the variation of thermal conductivity with temperature is small in the vicinity of the melting point for silicon and dk/dT can be set to zero. In certain special cases, these assumptions allow closed form solutions to Eq. (6) which can then be utilized to predict maximum growth rates through Eq. (1).

Ciszek² presents a solution to Eq. (6) assuming $h = 0$, $V\rho c(dT/dx)$ negligible, $q_R = \epsilon\sigma T_4$, $T_a = 0$, and k proportional to $1/T$. Boundary condition (3) was employed along with the condition $dT/dx = 0$ at $x = \infty$. The resultant expression for V_{\max} is:

$$V_{\max} = (1/h_{if} \rho_m) (\sigma \epsilon k_m T_m^5 / r)^{1/2} \quad (7)$$

where

ϵ = silicon emissivity at the melting point (0.46)

h_{if} = silicon heat of fusion (0.5027 W-h/g)

ρ_m = silicon density at the melting point (2.29 g/cm³)

σ = Stefan-Boltzmann constant (5.729×10^{-12} W/cm²K⁴)

k_m = 0.22 W/cm-K

T_m = 1685.2 K

r = crystal radius

Equation (7) is shown in Figure 3 and is the curve labeled "Ciszek".

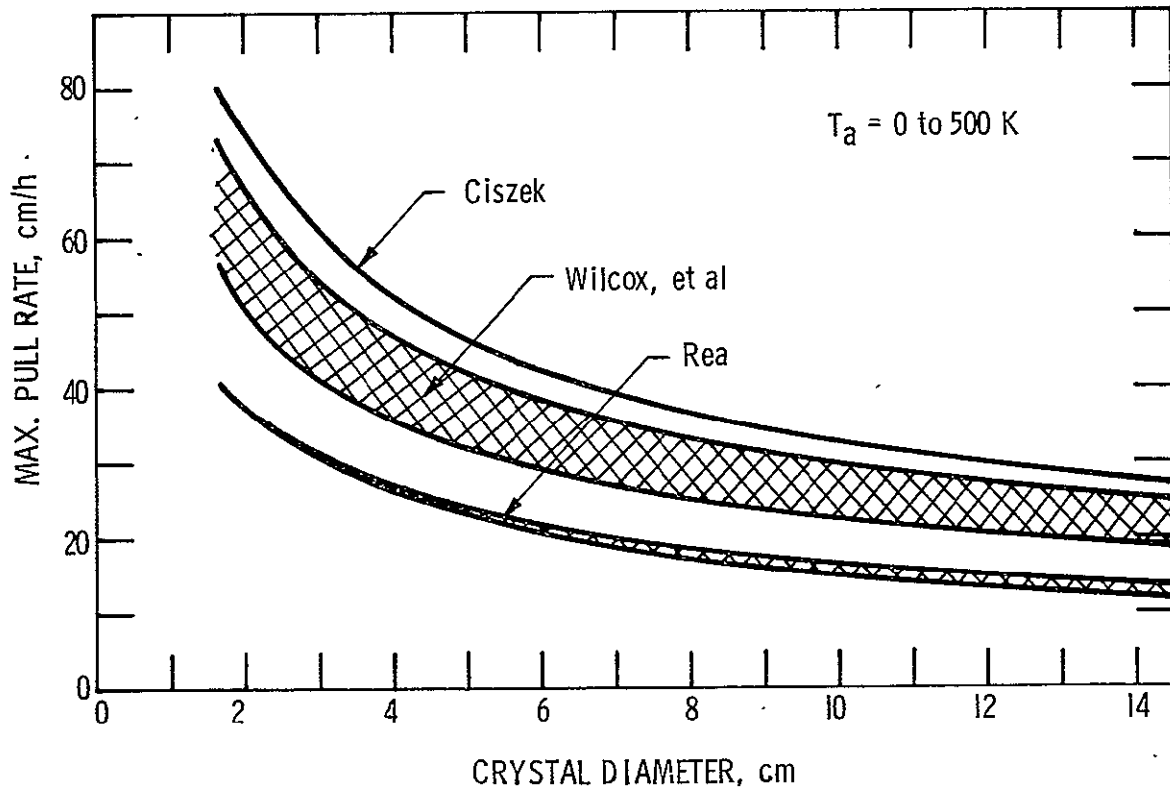


Figure 3. Silicon Pull Rates Predicted by Various Models

Wilcox, et al.^{3,4} assumed $k = \text{constant}$ and combined q_R with h to obtain a linearized Eq. (6). With the same boundary conditions as those of Ciszek², the maximum pull rate becomes:

$$V_{\max} = (1/\rho_m c_m) \left\{ 8 k_m h / [(1 + 2 h_{if}/c_m \Delta T)^2 - 1] \right\}^{1/2} (1/r)^{1/2} \quad (8)$$

where

$$\Delta T = T_m - T_a$$

$$h = \text{approximately } 0.0088 \text{ W/cm}^2\text{K}$$

Equation (8) is shown also in Figure 3 for values of T_a from 0 to 500K.

The two simplified thermal models discussed above result in significant variations in maximum pull rates (Figure 3). At 12-cm crystal diameter, maximum pull rates varying from 20 to 30 cm/h are predicted by Eqs. (7) and (8). In view of the uncertainty in maximum pull rates predicted by simplified theory, Eq. (6) was programmed for numerical solution with the boundary conditions given by Eqs. (3) and (4). The silicon thermal conductivity and emissivity were functions of temperature as indicated in Appendix A with density and specific heat held constant at 2.31 g/cm^3 and 0.000254 W-h/g-K respectively.

Of particular significance in the solution of Eq. (6) is an accurate representation of the radiation term, q_R . A puller operating under partial vacuum will have negligible thermal convection between the crystal and its ambient (see Appendix B). Consequently, the crystal cooling and, hence, the maximum pull rate is governed by the thermal radiation from the crystal surface. With the surfaces and nomenclature indicated in Figure 2 and by use of enclosure theory,⁵ a reasonable approximation of q_R is given by:

$$[A] \begin{Bmatrix} q_R \\ q_2 \\ q_4 \\ T_1 \end{Bmatrix} = \sigma \begin{bmatrix} T_1^4 - F_{d1-2} T_2^4 - F_{d1-3} T_a^4 - F_{d1-4} T_4^4 \\ T_2^4 - F_{2-3} T_a^4 - F_{2-4} T_4^4 \\ (1 - F_{4-4}) T_4^4 - F_{4-2} T_2^4 - F_{4-3} T_a^4 \\ F_{1-2} T_2^4 + F_{5-3} T_a^4 + F_{1-4} T_4^4 \end{bmatrix} \quad (9)$$

The coefficients of the matrix A in Eq. (9) are:

$$a_{11} = 1/\epsilon_1 \quad (10)$$

$$a_{12} = -(1 - \epsilon_2) F_{d1-2}/\epsilon_2$$

$$a_{13} = -(1 - \epsilon_4) F_{d1-4}/\epsilon_4$$

$$a_{14} = 0$$

$$\begin{aligned}
a_{21} &= 0 \\
a_{22} &= 1/\epsilon_2 \\
a_{23} &= -(1 - \epsilon_4) F_{2-4}/\epsilon_4 \\
a_{24} &= \sigma F_{2-1} \\
a_{31} &= 0 \\
a_{32} &= -(1 - \epsilon_2) F_{4-2}/\epsilon_2 \\
a_{33} &= 1/\epsilon_4 - (1 - \epsilon_4) F_{4-4}/\epsilon_4 \\
a_{34} &= \sigma F_{4-1} \\
a_{41} &= 0 \\
a_{42} &= (1 - \epsilon_2) F_{1-2}/\epsilon_2 \\
a_{43} &= (1 - \epsilon_4) F_{1-4}/\epsilon_4 \\
a_{44} &= \sigma
\end{aligned}$$

The F_s in Eqs. (9) and (10) are radiation view factors and the ϵ_s are emittances of the surfaces shown in Figure 2. The radiation flux q_R determined from Eq. (9) is a function of both x and T since the F_{d1} factors are functions of x . Appendix C presents the expression for F_{d1-2} and illustrates how several of the other view factors can be determined.

In order to solve Eq. (9) for q_R , the various surface temperatures must be specified. In all modeling work the silicon melt temperature (T_2) was assumed 1698K which is a nominal value experimentally observed for a wide variety of crystal pulls. The crucible liner temperature (T_4) was determined experimentally and its temperature as a function of H is shown in Figure 4. The data in Figure 4 were derived from temperatures obtained by manually scanning the side of a crucible with a PYRO Micro-Optical Pyrometer during crystal growth. The measured crucible liner temperature distributions were averaged over the distance H and these averaged temperatures are shown in Figure 4. Generally, the liner temperature decreases exponentially with distance from the melt level and, therefore, the use of an average liner temperature in the modeling work is an approximation.

The puller interior ambient temperature (T_3) varies widely so that use of a single value for this temperature is a gross approximation. Fortunately, as will be shown later, this temperature has a surprisingly minor influence on pull rate so the value used in modeling is not critical.

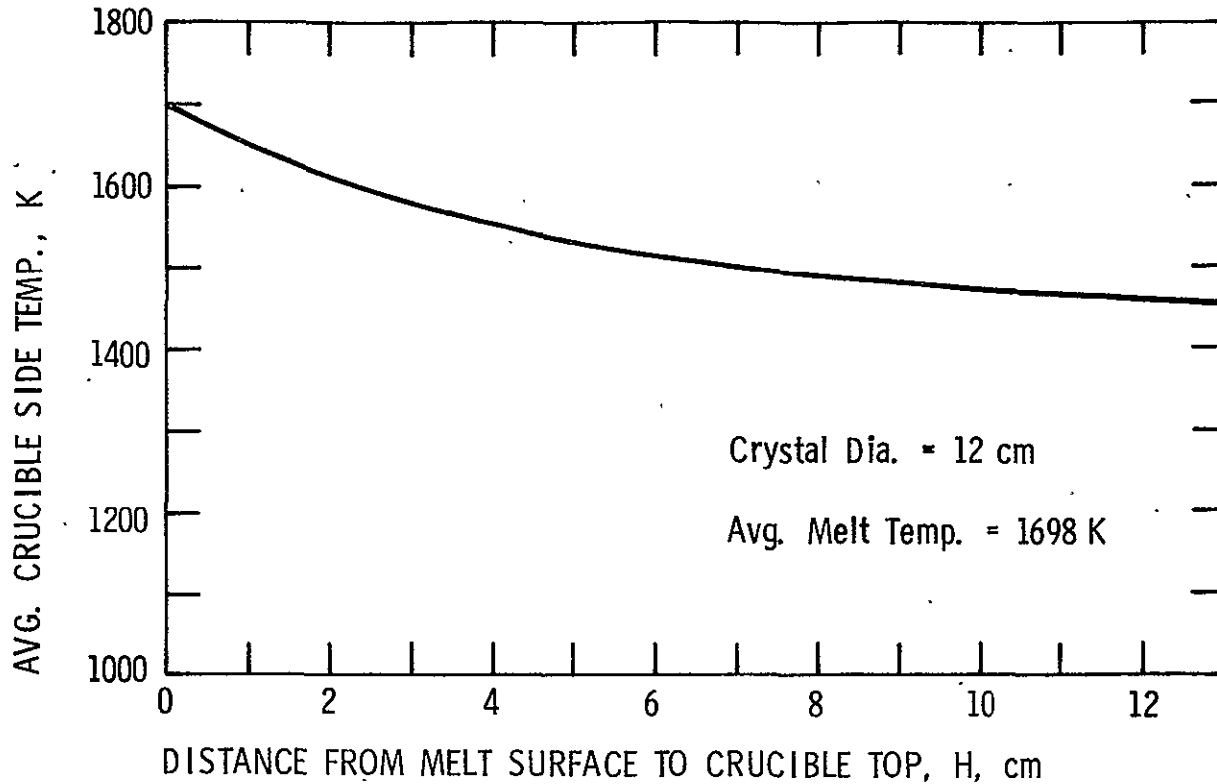


Figure 4. Experimentally Determined Crucible Side Temperature as a Function of Melt Level for a 12-kg Crucible

Figure 3 compares results of this modeling effort with those of Ciszek² and Wilcox^{3,4}. The Rea band in that figure is based on a 40-cm long crystal being grown from the 12-kg crucible used in the Varian Model 2848A Furnace, whereas the other two solutions are independent of the crucible configuration. The primary reason that the model developed in this investigation predicts lower pull rates than the other solutions is due to the inclusion of the strong thermal radiation interactions between crystal, melt surface, and crucible. These radiation effects decrease the crystal axial temperature gradient in the vicinity of the melt interface and, thereby, decrease the maximum possible pull rate. The maximum pull rates predicted by the Rea model are a function of crystal length, crucible geometry, melt level, ambient conditions, and heat shielding. The influences of these various parameters are discussed below.

The maximum pull rates predicted by the three models shown in Figure 3 are all proportional to $(1/d)^{1/2}$ where d is the crystal diameter.

Figure 5 illustrates the effect of semicontinuous pulling on maximum pull rate. In a single charge, the melt level continually drops relative to the crucible lip. This dropping melt level increases the thermal radiation exchange between crystal and crucible, thereby decreasing the

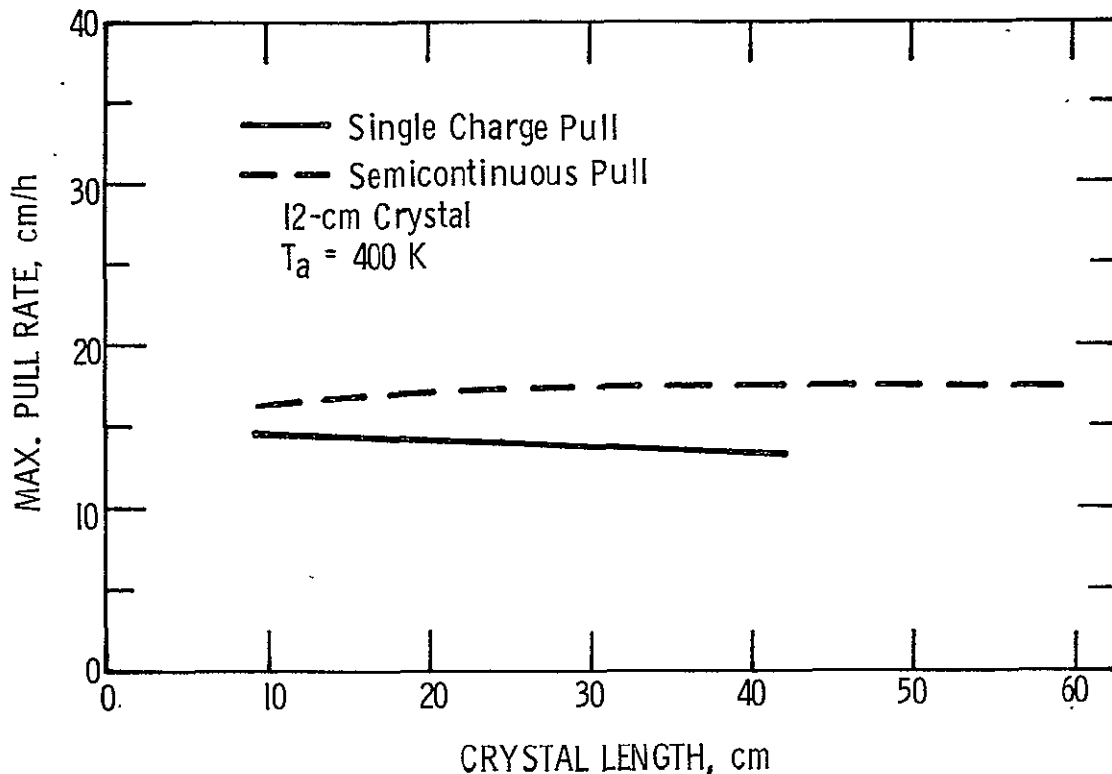


Figure 5. Theoretical Pull Rates for a 12-kg Crucible Czochralski Furnace

thermal gradient at the melt interface. Thus, the maximum pull rate decreases as the crystal grows in a single charge pull. Conversely, if the melt level can be held constant, the pull rate can be held approximately constant with crystal length. The average maximum pull rate for a single charge pull is 13.8 cm/h and the semicontinuous case has a maximum pull rate of 17.7 cm/h.

Figure 6 depicts axial temperature gradients for two crystal lengths for single charge pulls. The pronounced hump in the longer crystal is due to the thermal radiation from the crucible side. The indicated pull rates in the figure are the maximums for the two lengths.

All the results presented assume vacuum conditions within the puller. At higher ambient pressures, thermal convection between the crystal and gas aids in increasing the pull rate. However, as Figure 7 shows, this effect is minor. If 1 atm of argon were utilized, the pull rate could be increased only 0.5 cm/h or so over a wide ambient temperature range. Figure 7 shows that the ambient temperature has a surprisingly minor effect on pull rate. In a vacuum, the pull rate is virtually independent of ambient temperature up to 600 K. Conventional pullers operate at 1-30 mm Hg ambient pressure with argon purge. Convection heat transfer in argon is negligible at these pressures (Appendix B) so the vacuum curve in Figure 7 is appropriate for current pullers.

ORIGINAL PAGE IS
OF POOR QUALITY

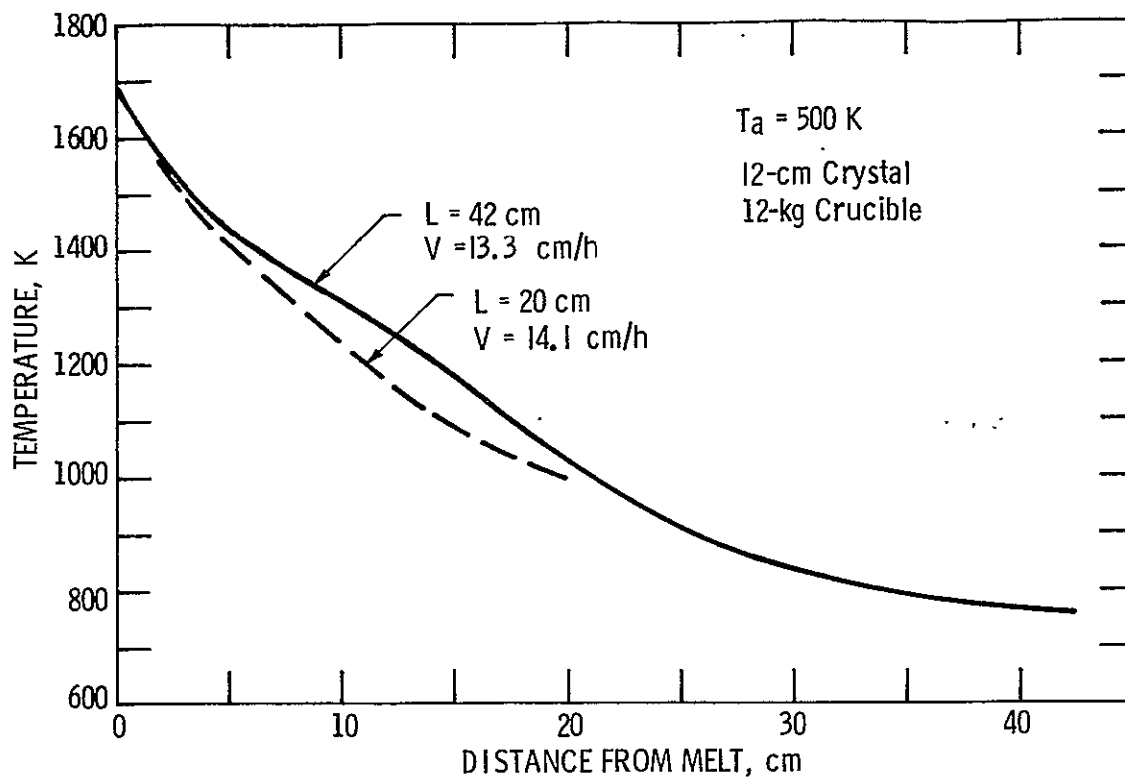


Figure 6. Theoretical Crystal Axial Temperature Profiles

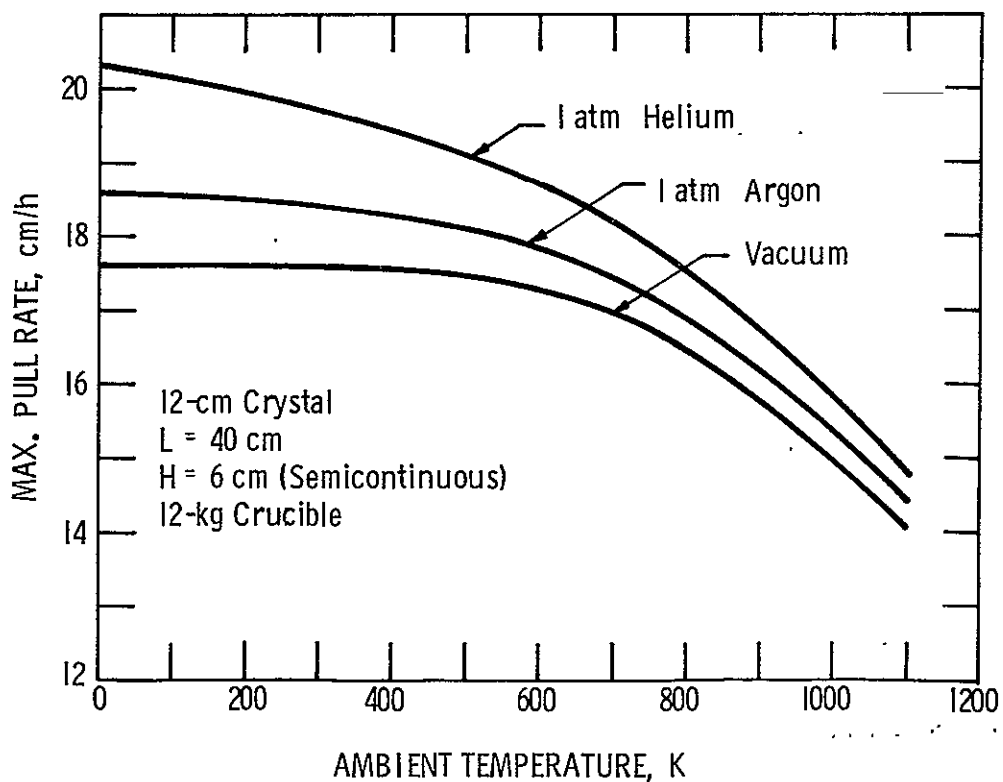


Figure 7. Effects of Puller Interior Ambient Conditions on Pull Rate

Figure 8 illustrates the effect on pull rate of varying the crucible radius. The Varian 12-kg crucible has a radius of 12.3 cm and a slight improvement in pull rate could be achieved with a larger crucible. However, puller power consumption would increase dramatically due to increased heat losses from the melt surface at the larger diameters.

The greatest improvement in potential maximum pull rate could be effected by heat shielding the crucible side. Figure 9 shows the effect on pull rate of varying the crucible emittance. Fused silica crucible liners have an emittance of 0.59 (Appendix A) at the temperatures experienced in a silicon puller. By lowering this emittance through use of heat shields, the maximum pull rate could be increased approximately 10%.

Another scheme for increasing crystal pull rates is to install a cold shield around the growing crystal which would provide a good heat sink to rapidly cool the crystal. One embodiment of this approach is shown in Figure 10 and modeling results are presented in Figure 11. The theoretical pull rate enhancement using a cold shield is slight even at coil distances from the melt as small as 6 cm and even then pull rate improvements on the order of only 6% could be achieved. Operational difficulties in pulling crystals through a coil mounted near the melt surface would be severe due to temperature control problems and lack of diameter control since the coil would obscure the diameter sensor's view of the halo.

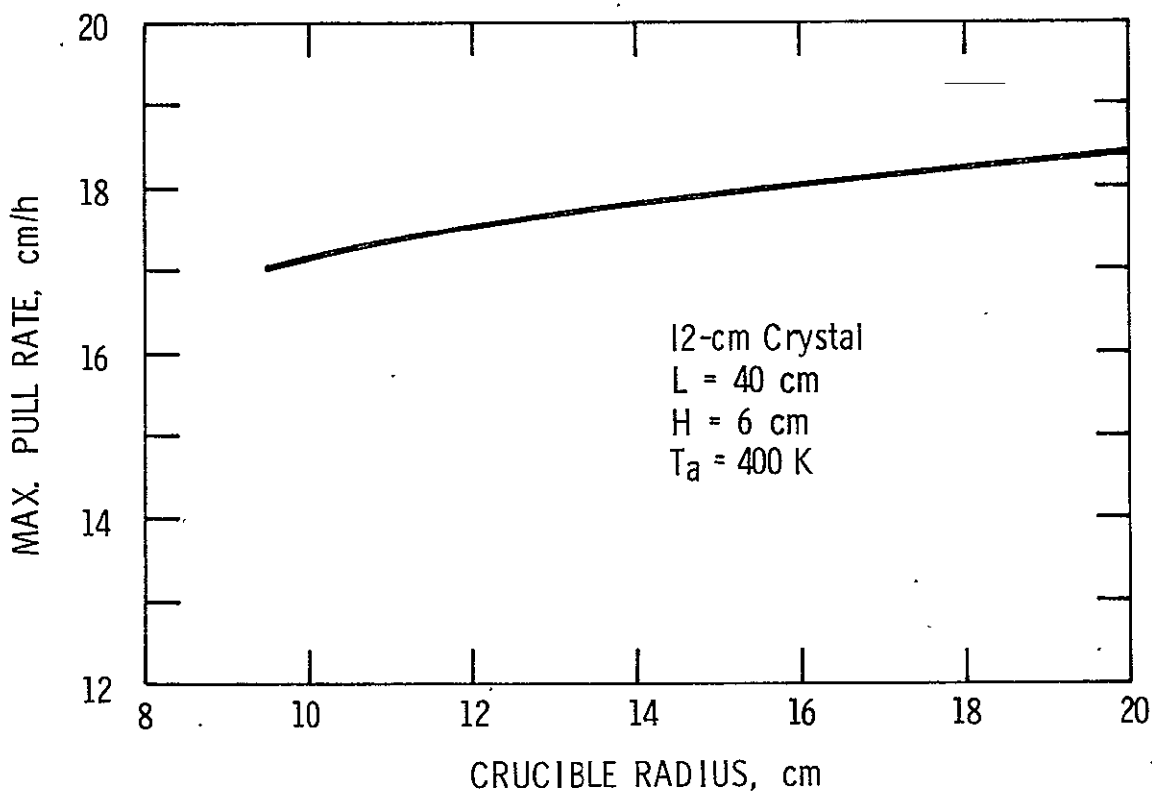


Figure 8. Effect of Crucible Radius on Pull Rate

ORIGINAL PAGE IS
OF POOR QUALITY

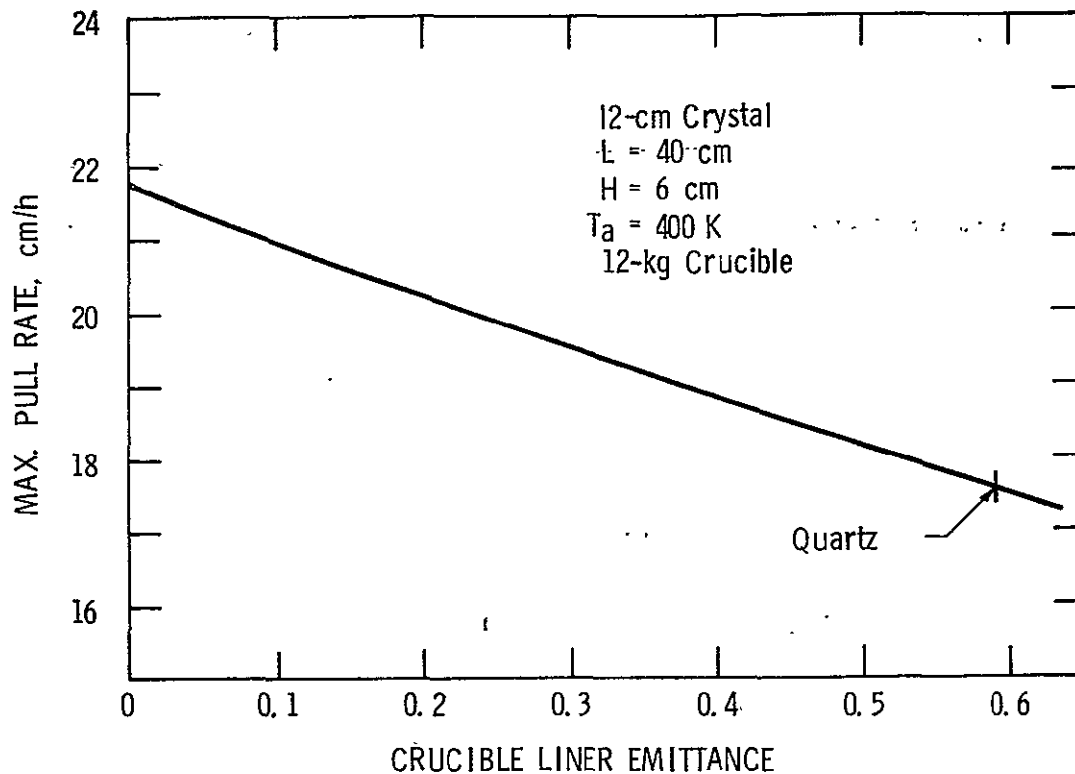


Figure 9. Influence of the Crucible Liner Emittance (Side Heat Shields) on Pull Rate

In summary, the pull rate modeling indicates that little can be done to increase Czochralski pull rates. The pull rate is determined primarily by the crystal diameter and the crucible/melt level geometry. The best approach to achieving high growth rates and, subsequently, high production rates is to develop a semicontinuous puller in which the melt level can be maintained close to the crucible lip during growth. Also, a slightly larger crucible, which will probably be necessary in a semicontinuous puller, will provide additional pull rate headroom.

2. Pull Rate Experiments

One of the goals of this program was to pull 12-cm crystal at 12 cm/h. As Figures 3 and 5 indicate, the theoretical maximum pull rate for single charges is in the 13-14 cm/h range so that a 12 cm/h growth rate represents 90% of the maximum possible. Several runs were made to determine the maximum pull rate and it was found that 12.7-15 cm/h was limiting for 12-cm crystal although the 15 cm/h value is questionable as it was sustained for only a few minutes before freeze-out occurred. These experimental results are in excellent agreement with the theoretical curves in Figures 3 and 5 for single-charge pulls in a vacuum with argon purge. The maximum pull rate sustainable for long periods was found to be 10 cm/h. One crystal was grown at this average pull rate over a 34.3-cm length. Crystals were routinely pulled during this investigation at 8 cm/h and with volume production and experience, pull rates in the 8-10 cm/h range should become standard. In economic modeling of the Czochralski process, a 9-cm/h pull rate was assumed for single and multicharge operation.

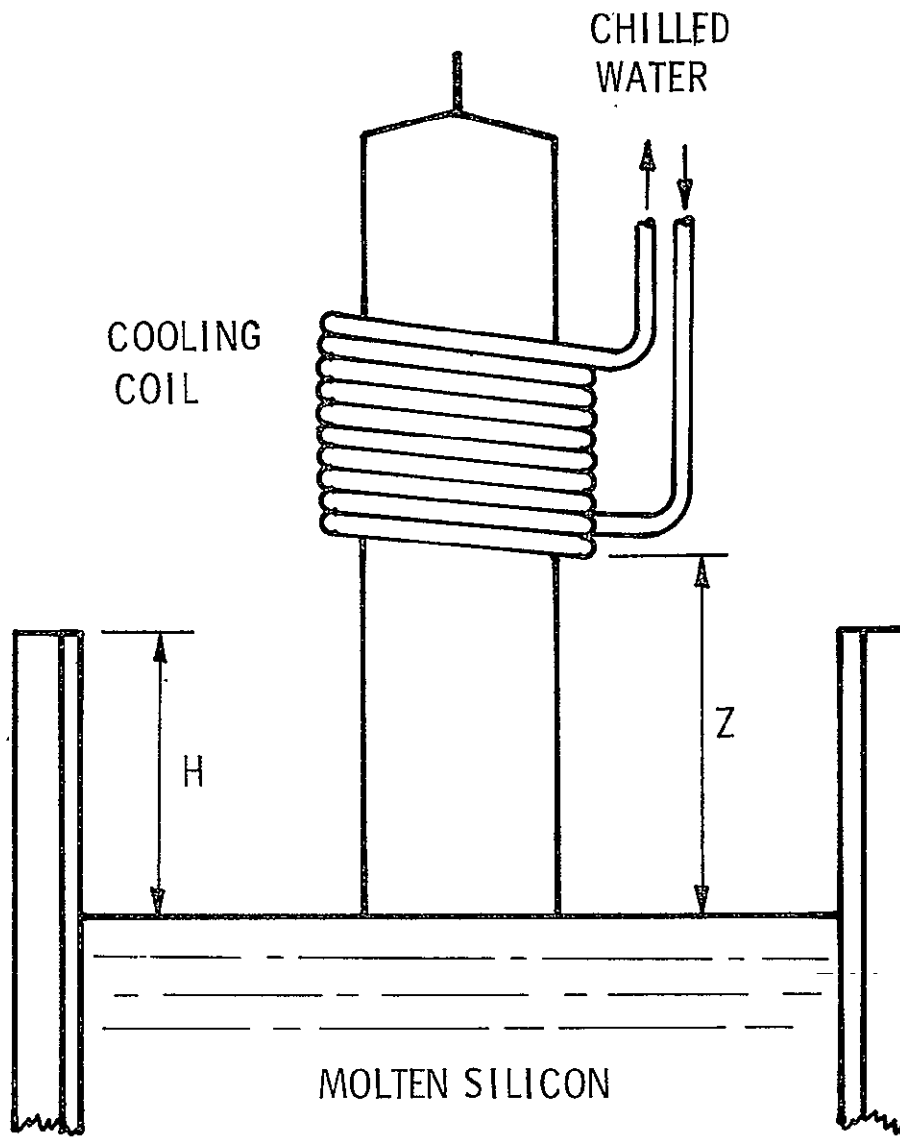


Figure 10. Crystal Cooling Coil Configuration

Several experiments exploring pull rate enhancement were performed with a small research crystal puller in which 7.6-cm silicon crystals were grown from 6-kg crucibles. This puller utilizes a helium ambient at atmospheric pressure. In one series of experiments, the cooling coil scheme of Figure 10 was tried. A coil was fabricated from 10-mm diameter stainless steel tubing with a coil ID of 10 cm. The coil was mounted 14 cm above the melt level.

Three attempts were made to grow crystals with the cold coil. The first two attempts failed due to cracked crucible liners. The cold coil created a large heat sink for the melt and thermal stresses induced in the liners were sufficiently high to cause cracking. A molybdenum heat shield

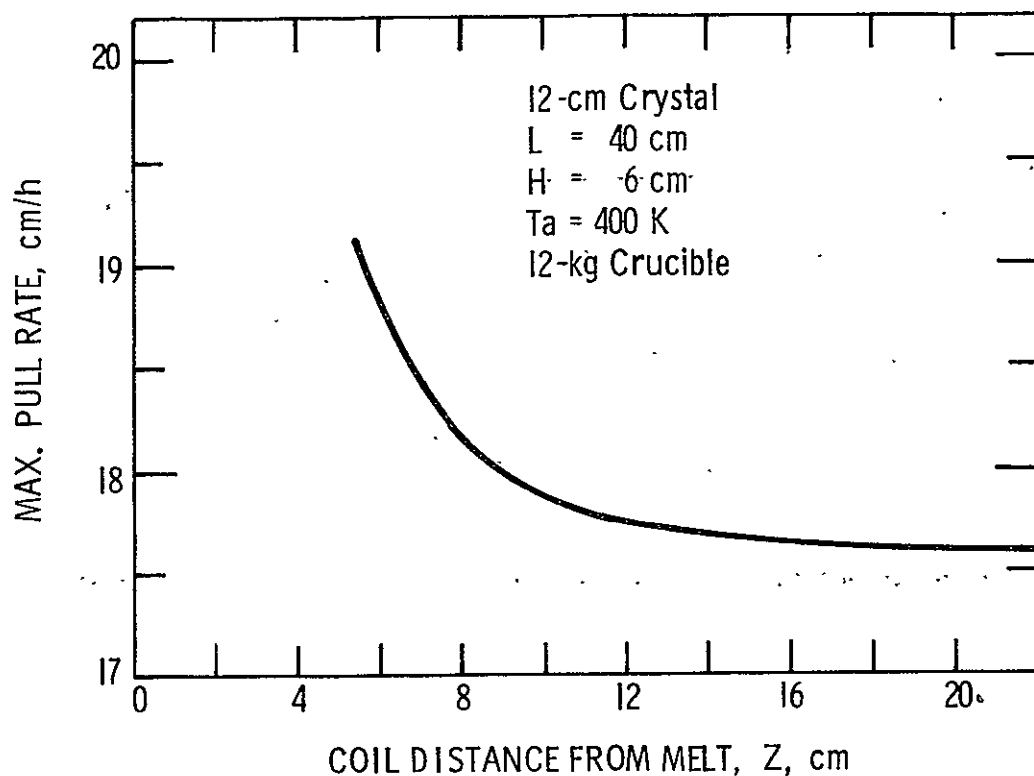


Figure 11. Theoretical Influence of Crystal Cooling Coil Position on Pull Rate

was mounted between the crucible lip and coil to partially shield the liner from the coil and melt-in and growth were achieved on the third attempt. As the growing crystal entered the coil, the pull rate was carefully adjusted to its maximum. Freeze-out occurred at 22-cm/h pull rate. Crystal length at freeze was 28 cm and the gross crystal weight was 3.04 kg.

The theoretical maximum pull rate for a 7.6-cm crystal pulled from a 6-kg crucible in a helium atmosphere is 20.8 cm/h. With a cold coil 14 cm above the melt, the maximum pull rate is computed to be 21.6 cm/h. Thus, the observed 22 cm/h at freeze with cold coil was at the theoretical maximum and the cold coil, at best, contributed only an additional 0.8 cm/h for the puller test conditions. In past work with 7.6-cm crystals pulled from 6-kg helium pullers, a "safe" maximum pull rate of 17-18 cm/h has been sustained for substantial crystal lengths. This pull rate is approximately 86% of the theoretical maximum and it appears that the cold coil did not enhance this practical maximum pull rate. Other drawbacks to the cold coil included a 20% increase in puller power during melt-in over that with no coil and temperature control during growth was not as precise because of the large heat sinking effect with the result that diameter control was very poor. It was decided not to try the cold coil with 12-cm crystal in view of these results and the model prediction of Figure 11.

One attempt was made in the 6-kg helium puller to decrease the crucible side emittance by attaching a molybdenum sheet around the crucible periphery. The moly sheet covered the upper 5 cm of the liner. Molten silicon dissolves moly and in spite of efforts to prevent contact between the silicon and moly, significant areas of the moly sheet were dissolved in the melt and the run was terminated. In view of these and other anticipated difficulties in controlling crucible emittance, this approach was abandoned.

Another approach to pull rate enhancement by crystal cooling is to funnel the ambient gas over the crystal by use of a stainless steel or quartz tube through which the crystal is pulled. This technique was tried in the small puller by installing a 9.2 cm ID quartz tube at a 15-cm distance above the melt level. A helium flow rate of 17 l/min was maintained through the tube as the crystal was grown. Two 7.6-cm crystals were grown in this manner and one froze at a length of 27 cm (12 cm into the funnel) and the other lost perfection 6.6 cm into the funnel. Both these problems are due to the cooling effect at the growth interface caused by the helium impingement on the melt surface. The maximum pull rate achieved was 21 cm/h which was very near the 22 cm/h experienced with the cold coil. In fact, a careful examination of the gas funnel reveals that it is merely a variation on the cold coil concept except gas cooling is employed rather than chilled water.

In a vacuum environment with argon purge the effect of a funnel would be much less pronounced than that for helium at atmospheric pressure due to the greatly reduced heat transfer (Appendix B). Thus, the effect of the funnel should be very similar to that shown in Figure 1.1 for a cold coil and unless the funnel is lowered almost to the growth interface, little pull rate enhancement could be expected. In that case, growth conditions would probably worsen because of the added gas impingement on the melt surface. Consequently, this technique was not pursued on the 12-kg large diameter puller.

Overall, the pull rate experimental work confirmed the theoretical model predictions. No pull rate enhancement scheme appears sufficiently promising to warrant applying to 12-cm diameter growth. All the enhancement techniques considered represent additional cost and maintenance items which quite possibly would outweigh any savings due to slightly higher pull rates.

3. Multicharge Analysis

A procedure involving pulling several crystals from a single crucible liner in one continuous furnace run offers a sizable cost reduction potential for the Czochralski process. In order to estimate the potential yields in such a procedure, the 3-crystal multicharge process assumed in the economic modeling is examined. The initial polysilicon charge is 18 kg from which a 56-cm crystal is grown weighing 14.82 kg. Bottom taper on the crystal is assumed to weigh 700 g based on experience. The melt is replenished with 14.82 kg polysilicon, another 56-cm crystal pulled,

14.54 kg polysilicon added, and a final 56-cm crystal pulled, leaving behind a button weighing 0.8 kg. Thus, in this process 47.36 kg polysilicon is charged with a maximum crystal weight of 44.46 kg. A theoretical yield analysis based on resistivity is given below for both boron and phosphorus-doped crystal in the 0.3 to 1.5 Ω -cm range.

The fraction of melt solidified, g , for the first crystal at start of taper is $14.82/18.0 = 0.823$. By assuming that the crystal top resistivity is 1.5 Ω -cm, the resistivity at taper start is computed from:

$$\rho_B = \rho_T (1 - g)^{1 - k_{\text{eff}}} \quad (11)$$

where

ρ_B = bottom resistivity

ρ_T = top resistivity

k_{eff} = effective segregation coefficient (0.45 for phosphorus and 0.85 for boron)

For $g = 0.823$, the value at start of taper, Eq. (11) yields:

$$\begin{aligned} \rho_B &= 1.16 \text{ } \Omega\text{-cm for boron} \\ &= 0.58 \text{ } \Omega\text{-cm for phosphorus} \end{aligned}$$

Thus, for either dopant, the entire length of the first crystal is within the assumed resistivity range.

The second crystal is pulled from a 17.3-kg melt. Additional dopant must be added to bring the dopant concentration up to a level to hit 1.5 Ω -cm at the crystal top. For a 17.3-kg melt, the initial concentration to provide this resistivity is:

$$C_O (\text{boron}) = 8.89 \text{ E19 atoms} \quad (12)$$

$$C_O (\text{phosphorus}) = 5.71 \text{ E19 atoms.} \quad (13)$$

The amount of dopant, N , incorporated into the first crystal and taper is given by:

$$N = \int_0^{0.862} C dg \quad (14)$$

with

$$C = k_{\text{eff}} C_O (1 - g)^{k_{\text{eff}} - 1} \quad (15)$$

and C_0 is the initial dopant concentration in the 18-kg melt. These initial concentrations are:

$$C_0 = 9.25 \text{ E19 atoms boron} \quad (16)$$

$$= 5.94 \text{ E19 atoms phosphorus.} \quad (17)$$

Equations (14)-(17) give:

$$N = 7.53 \text{ E19 atoms boron} \quad (18)$$

$$N = 3.50 \text{ E19 atoms phosphorus} \quad (19)$$

Equations (12)-(19) must be combined to determine the additional dopant, ΔN , to yield the proper concentration for the second crystal.

$$\Delta N (\text{boron}) = (8.89 + 7.53 - 9.25) \text{ E19 atoms} \quad (20)$$

and

$$\Delta N (\text{boron}) = 7.17 \text{ E19 atoms} \quad (21)$$

Similarly:

$$\Delta N (\text{phosphorus}) = 3.27 \text{ E19 atoms} \quad (22)$$

For $g = 14.82/17.3 = 0.857$, the bottom resistivities of the second crystal from Eq. (11) are.

$$\rho_B = 1.12 \text{ } \Omega\text{-cm for boron}$$

$$= 0.52 \text{ } \Omega\text{-cm for phosphorus}$$

and, again, the entire second crystal is in the assumed resistivity range for either dopant.

The third crystal is pulled from a 16.32-kg melt and the desired initial concentrations are:

$$C_0 = 8.38 \text{ E19 atoms boron}$$

$$= 5.38 \text{ E19 atoms phosphorus}$$

Through the same computational procedure outlined above for the second crystal, the additional dopant required for this last crystal is

$$\begin{aligned}\Delta N &= 7.09 \text{ E19 atoms boron} \\ &= 3.33 \text{ E19 atoms phosphorus}\end{aligned}$$

Bottom resistivities for this third crystal are, from Eq. (11):

$$\begin{aligned}\rho_B &= 1.05 \text{ } \Omega\text{-cm for boron} \\ &= 0.40 \text{ } \Omega\text{-cm for phosphorus}\end{aligned}$$

Thus, the third crystal is also completely within the desired 0.3 to 1.5 $\Omega\text{-cm}$ resistivity range for both dopants.

The maximum theoretical yield is given by the sum of the three crystal weights divided by the total polysilicon charged:

$$\text{Yield} = 44.46/47.36 = 0.939.$$

The maximum yield is, therefore, 93.9% based on weight in-weight out. The 100% yield points in the economic modeling are based on crystal length and correspond to this 93.9% weight yield.

In a production mode, the crystal bottom tapers would be available for recycle. By assuming that 500 g of the 700 g tapers are available for recycle, the total yield on new polysilicon would be $44.46/45.86 = 0.969$. Grind losses on crystals pulled under automatic diameter control should average under 10%. With a 90% grind yield, the overall maximum crystal yield on new polysilicon for the 3-pull process would be 84% to 87% depending upon the amount of recycle utilized.

4. 12-cm Growth

Large diameter growth experiments were performed on a Varian Model 2848A Furnace modified for 12-kg charges. Various puller alterations required to accommodate 12-cm diameter crystal growth included a larger crucible, larger heater, a new lower chamber dome with a 15-cm throat capacity, and a higher capacity vacuum pump. The lower chamber dome was designed and built by Texas Instruments and included a special port for multicharge operation. The interior hot zone parts were purchased from Varian.

A large number of single-charge pulls were made to determine cycle times, yields, maximum pull rate, and various other operating problems and costs associated with 12-cm growth. Table 1 lists pertinent information regarding the majority of these test runs. The crystals were numbered

Table 1. 12-cm Crystal Summary

Crystal	Crystal Orientation	Charge Weight kg	Grow Weight kg	Crystal Diameter cm	Crystal Length cm	Avg. Pull Rate cm/h
12-2	(111)	10	5.9	11.9	20.3	9.7
12-3	(111)	10	7.2	12.0	25.4	8.5
12-4	(111)	12	10.1	12.5	34.3	10.0
12-5	(111)	12	9.5	10.9	39.4	8.8
12-9	(100)	10	8.2	12.4	25.4	8.5
12-11	(100)	10	7.2	12.1	24.1	7.8
12-12	(111)	10	4.7	12.1	17.0	13.6*
12-14	(100)	10	8.3	12.2	29.0	8.7
12-16	(100)	10	8.0	11.2	25.4	8.5
12-17	(100)	10	3.5	12.2	12.7	7.9
12-18	(100)	10	2.3	11.2	7.6	12.7*
12-19	(100)	10	5.2	12.2	17.3	11.5
12-20	(100)	10	4.9	12.2	16.5	7.9
12-21	(100)	10	8.4	13.8	23.6	6.4
12-22	(100)	10	2.5	12.2	8.9	7.4
12-23	(100)	12	2.1	12.2	7.6	5.1
12-24	(100)	12	9.9	12.3	30.5	7.1
12-25	(100)	12	5.7	12.4	20.3	8.1
12-26	(100)	12	9.5	12.1	29.9	6.9
12-27	(100)	10	3.2	12.2	11.4	11.4-12.7*
12-30	(100)	10	4.2	12.2	15.2	10.1-15.2*
12-31	(100)	10	5.8	12.3	21.0	11.0
12-33	(111)	12	11.1	12.7	32.0	7.2

*Melt freeze at this pull rate

sequentially and the missing numbers in Table 1 are principally scrapped charges due to miscellaneous factors such as particulates in the melt, cracked liners, or puller malfunctions. Crystals 12-22 and 12-23 in the table were ruined by particulates falling into the melt during growth and crystals 12-18, 12-27, and 12-30 were prematurely terminated in attempts to maximize their pull rates. The (100) crystal orientation was emphasized in this study for two reasons: (1) it is harder to grow, and (2) slices cut from (100) crystals can be readily texture-etched thereby providing an inexpensive AR coating for solar cells.

Considerable effort was expended in the initial phases of 12-cm growth on improving crystal quality. There was a strong tendency for crystals to lose perfection in the length range 2-12 cm. Often crystallinity loss in this range is due to improper seed growth in which residual dislocations in the seed grow out to the crystal surface, usually within a crystal radius. However, the majority of crystals lost perfection for no apparent reason, a phenomenon referred to as "spontaneous perfection loss" for want of a better explanation.

The cause of spontaneous crystal loss is believed due to the size and stability of the puller hot zone. In order to maintain good control over crystal diameter, it is necessary to keep the melt level constant relative to the diameter sensor. Consequently, the crucible must be continually raised during a pull to compensate for the volume of crystal solidified. The constantly rising crucible coupled with the lengthening crystal continually change thermal conditions within the hot zone and the rate of change is obviously a function of pull rate. The slower the pull rate the more stable the hot zone and the greater the probability that crystal perfection can be maintained.

After considerable experimentation, the puller hot zone was lengthened 5 cm and this improved crystal growth characteristics although at the expense of pull rate. This modification was effected with crystal 12-21 and the average pull rates took almost a step-function decrease at that point (Table 1). The larger hot zone increased the critical length to around 10 cm. If the 10-cm point was negotiated successfully, the crystal could be pulled forever, virtually unattended. However, getting through this critical length required considerable skill and intense operator attention. With greater operator experience along with puller hot zone design improvements, the critical length probably can be reduced greatly in importance if not eliminated entirely. The 5-cm hot zone extension is not necessarily optimal but was the maximum extension possible which would still allow operation of the multicharge feeder. A somewhat longer extension may be preferable although pull rate may be affected adversely.

In Table 1, average pull rate is defined as the crystal length from shoulder to taper start divided by the time to grow this length. Pull rates generally declined during a pull in qualitative agreement with Figure 5. Experiments to determine the maximum pull rate are indicated in Table 1 by the asterisks. The maximum range was experimentally determined to be 12.7-14 cm/h where maximum pull rate is defined as that pull rate at which melt freeze begins. This definition is somewhat imprecise since melt freeze does not occur instantaneously and a qualitative judgment is required. In crystal run 12-30, the pull rate was systematically increased in approximately 1.0 cm/h increments every 30 minutes. Melt freeze was beginning at around 14 cm/h, and reached catastrophic proportions at 15.2 cm/h so that this maximum value is by no means a sustainable rate.

The 12.7 cm/h pull rate is slightly below the theoretical pull rates in Figure 5 for the indicated crystal lengths in Table 1. The thermal modeling assumes that thermal equilibrium exists between the growing crystal and its surroundings. Implicit in this assumption is the idea that the puller can respond instantaneously to melt temperature changes due to crucible location changes. In reality, of course, there is thermal lag in the heater, crucible, and heat shield, all of which limit the crucible lift rate if melt freeze is prevented which, in turn, imposes an additional constraint on the maximum pull rate.

Overall, it appears that 10 cm/h is a practical maximum pull rate for 12-cm diameter, single-charge pulls. Economic modeling of the Czochralski process assumes 9 cm/h which should be readily attainable with experience gained from volume production.

Two goals of this program were to demonstrate grow yields of 80% and final yields of 60% based on polysilicon charged. The 80% grow yield was accomplished in several pulls with run 12-33 exhibiting a 92.5% grow yield. The crystals starting with 12-11 were boron-doped to hit around 1 Ω -cm at the top. Thus, no crystal was lost due to resistivity and final yields were dependent on grind and crop losses. Crystal 12-24 exhibited a 64.5% final yield and 12-26 had a 64.3% overall yield. Crop losses on many of the crystals due to high dislocations cut the final yields below 60%. Also, two crystals, 12-21 and 12-33 exhibited severe thermal stress cracks which reduced the final yield on 12-21 to 36% (ground) and that of 12-33 to 32% unground. Both these crystals were grown at relatively low pull rates so the cracking is puzzling and no explanation is available. Generally, grow yields in excess of 80% are feasible and final yields of 70-80% based on polysilicon input should be attainable provided crystal grind is not required.

5. Multicharge Process

Puller productivity per cycle can be increased substantially and operating supplies per unit of production can be reduced by pulling multiple crystals during a furnace run. In the limit semicontinuous crystal pulling, in which polysilicon is continually fed into the crucible, offers the lowest cost potential but this approach will require considerable development to implement. An intermediate step for achieving multiple crystal growth is to pull crystals from discrete polysilicon batches which are loaded into the heated crucible between crystal pulls. A 3-pull multicharge process can effect approximately a 25% cost reduction over single-charge pulls and this 3-pull process was evaluated in this study.

After examining various alternatives, it was decided to utilize nugget polysilicon with a feed scheme depicted in Figure 12. A 61.8 mm ID stainless steel tube was inserted into a stainless bellows and the tube and bellows were welded together at the upper end through a flange. A 9-kg capacity polysilicon container was attached to this flange by a flexible metal hose through which the polysilicon was fed. During a crystal pull the flexible hose and container were removed to allow refilling of the container with polysilicon. The bellows assembly was connected to a port on the lower chamber and the feed tube could be extended about 40 cm into the chamber. After charging the crucible, the feed tube was retracted by extending the bellows which was then locked in place and the feed tube was completely out of the way for crystal growth. An argon purge was maintained through the feed assembly during charging.

Three initial runs were made to determine a procedure for feeding the nugget polysilicon into the crucible. In these runs, which are 12-27, 12-28, and 12-29 in Table 2, 3-kg polysilicon was melted and then 7 kg of nuggets were dropped into the melt. During charging, the puller was at atmospheric pressure with argon purge. In 12-27 the nuggets were fed into the melt fairly rapidly

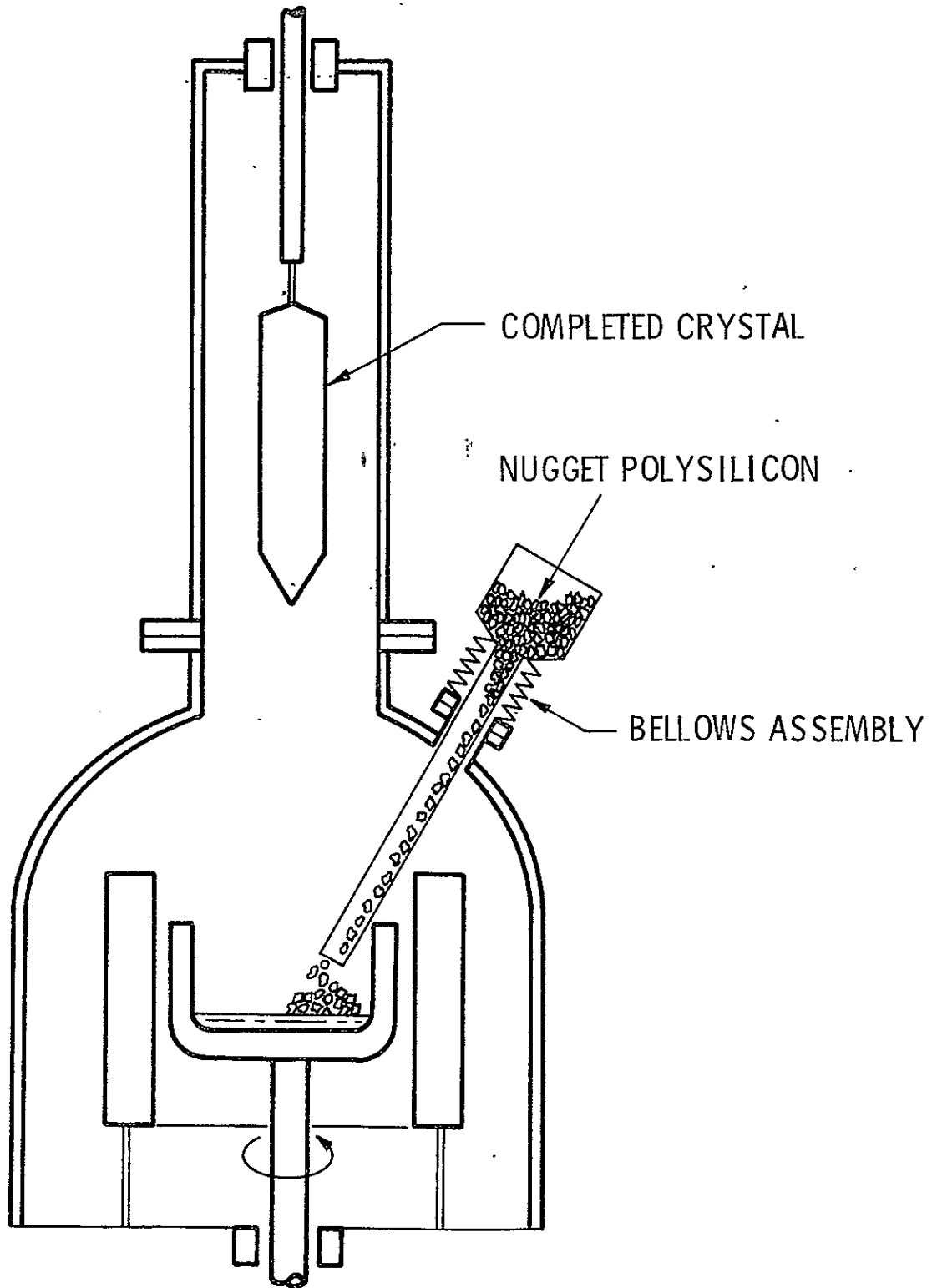


Figure 12. Technique for Hot-Charging a Czochralski Puller

ORIGINAL PAGE IS
OF POOR QUALITY

Table 2. Multicharge Crystal Pulls

Crystal	Crystal Orientation	Charge Weight kg	Grow Weight kg	Crystal Diameter cm	Crystal Length cm	Avg. Pull Rate cm/h
12-27	(100)	10	3.2	12.2	11.4	11.4-12.7*
12-28	(100)	10		Scrapped — liner buckled		
12-29	(100)	10	3.5	12.2	12.7	3.6
12-30	(100)	10	4.2	12.2	15.2	10.1-15.2*
12-31	(100)	10	5.8	12.3	21.0	11.0
12-32(A)	(100)	12	8.5	12.2	27.9	7.5
12-32(B)	(100)	7	7.7	12.6	25.4	9.0
12-32(C)	(100)	7	8.1	12.3	25.9	6.1
12-34(A)	(111)	8	4.4	8.4	31.8	10.0
12-34(B)	(111)	4.5		Run terminated — puller malfunction		
12-35(A)	(111)	8	3.8	9.2	24.3	4.4
12-35(B)	(111)	4.5	3.8	8.3	30.5	7.0
12-35(C)	(111)	4	3.5	8.3	26.7	6.2
12-36	(100)	4	3.4	7.9	25.4	10.2

* Melt freeze at this pull rate

while the crucible was rotated. The 7 kg required 15 minutes to feed, the puller was back under vacuum in 18 minutes, and the silicon was fully melted within 32 minutes from start of feed. The resulting melt was clean-looking but three attempts to grow a single-crystal top failed and a polysilicon plug was pulled.

In run 12-28 a very slow feed was used such that the nuggets were given sufficient time to melt before additional ones were added. Toward the end of the charging process, considerable melt splashing occurred which greatly reduced the rate at which the nuggets could be added and the total charge time was a lengthy 1.3 h. The resulting 10-kg melt was very dirty and, in addition, the liner developed a severe buckle along one side making melt temperature control virtually impossible. A short plug was pulled before freezing occurred and the charge was scrapped.

A different charging approach was used in run 12-29. Power to the 3-kg melt was lowered until the melt surface froze. The 7-kg nugget charge was then fed into the crucible rapidly (5 minutes). Full power was restored and the 10-kg charge melted within 20 minutes. Unfortunately, as in run 12-28 the resulting melt was fairly dirty and a single crystal could not be grown.

Of the three feed techniques tried, that of run 12-27 offered the most promise and was selected for multicharge runs. The charge procedure was:

- 1) Lower the crucible
- 2) Increase puller power approximately 25%
- 3) Shut vacuum valve
- 4) Flood lower chamber with argon to one atmosphere
- 5) Lower charge feed tube
- 6) Couple nugget container flexible hose to the bellows flange
- 7) Feed nuggets into the rotating crucible
- 8) Disconnect flexible hose from bellows
- 9) Retract feed tube
- 10) Open vacuum valve
- 11) Increase puller power to 80 kW.

Three multicharge runs were made: 12-32, 12-34, 12-35 in Table 2. In each run the initial charge was large-piece polysilicon followed by nugget refills. In 12-32, the total crystal weight was 24.3 kg out of a 26-kg charge weight for a grow yield of 93.5%. However, the two crystals grown from nugget charges were high dislocation. Run 12-32 required 26.8 h including 20 minutes consumed in repairing the upper chamber seed shaft seal after the first crystal. A major time-consuming factor in this run involved cool-down of the completed crystal in the upper chamber before removal. This time averaged 1.9 h for crystals 12-32(A) and 12-32(B). Cool-down time could be decreased by directing argon jets onto the crystal as it is raised into the upper chamber.

Prior to multicharge run 12-32, runs 12-30 and 12-31 were made to attempt good crystal pulls from nugget polysilicon. Run 12-30 produced 5.1 cm dislocation-free crystal before losing perfection but 12-31 was high-dislocation its entire length. In view of this difficulty in growing good 12-cm crystal from nugget polysilicon melts, it was decided to try smaller crystal with a $\langle 111 \rangle$ orientation, runs 12-34 and 12-35. However, these crystals also were high-dislocation. In run 12-34(B) the heat shield sagged against the heater causing severe arcing and the run was terminated.

Crystal 12-36 was pulled from a nugget polysilicon melt in a small RF-heated puller utilizing a helium ambient at one atmosphere pressure. This crystal was dislocation-free to the taper end and indicates that nugget polysilicon is a suitable starting material. Out of ten attempts to use nuggets in the Varian puller, only one crystal was perfect and that for only 5.1 cm (12-30). Thus, there appears to be a fundamental problem in utilizing nugget polysilicon in an RH-heated puller. The major cause of this problem is believed to be excessive carbon incorporation in the nugget poly melts. Crystal 12-32C had SiC precipitates evident on the surface and IR measurements of carbon in 12-32(B) and 12-32(C) indicated very high carbon levels of $4 \times 10^{17}/\text{cm}^3$. At this carbon level, single crystal growth is difficult if not impossible. It is essential to find a growth technique or loading procedure which minimizes carbon in the melts for successful multicharge or semicontinuous Cz growth.

B. CRYSTAL SLICING

1. Introduction

In order to achieve minimum cost Cz silicon sheet, the ingot slicing process must: (1) produce minimal kerf thickness, (2) provide thin slices, (3) exhibit high yields, and (4) offer high slice production rates. In surveying slicing approaches to meet these criteria, it appears that multiblade abrasive slurry sawing has the greatest potential, at least for large diameter ingot. Slurry sawing can provide good slice thickness control and the as-sawed surfaces are sufficiently smooth so that chemical etching can provide an acceptable surface for solar cell fabrication. The elimination of costs associated with lapping or polishing coupled with an anticipated 2X cost advantage of the basic sawing process indicate slurry sawing to be significantly cheaper than conventional ID slicing.

A Varian Model 686 Wafering Machine was used in the sawing experiments. This saw will accept 12-cm crystals up to 19 cm long although much of the experimental work was done on 5 and 7.6-cm crystals around 10 cm long. The maximum blade head reciprocation rate of the Varian saw is 100 cycles/min but a practical maximum is around 80 cycles/min with 60 cycles/min being the speed at which most of the experiments were performed. The major emphasis of the slicing activity, described below, was to minimize slice plus kerf thickness while maximizing cutting rates. Various parameters such as blade dimensions, blade force, blade speed, and slurry composition were investigated with regard to optimization.

2. Experimental

Experiment 1. Cutting Rate versus Feed Force

A 7.64-cm crystal was mounted on a 5.08-cm wide by 1.27-cm thick glass plate using Cenco wax. The blade thickness was 0.2 mm with a spacer thickness of 0.74 mm. The stroke length was 20.0 cm at 56 cycles/min providing a blade speed of 37 cm/s. Kerf volume versus blade travel for 0.37, 0.75, and 1.12-N blade loads are plotted in Figure 13. The average slice thickness was 0.60 mm with an average kerf of 0.34 mm. Total cycle time was 32 hours. Additional data are given in Table 3.

Experiment 2. Cutting Rate versus Feed Force

The crystal was mounted as in Exp. 1 and used similar blades, spacer dimensions, and blade speed. Kerf volume versus blade travel are shown in Figure 13 for 1.1, 1.5, and 1.9 N/blade. The average slice thickness was 0.60 mm with an average kerf of 0.34 mm. Additional data are given in Table 4. Total cycle time was 19 hours, an improvement over Exp. 1 by 41% due to the higher blade loads.

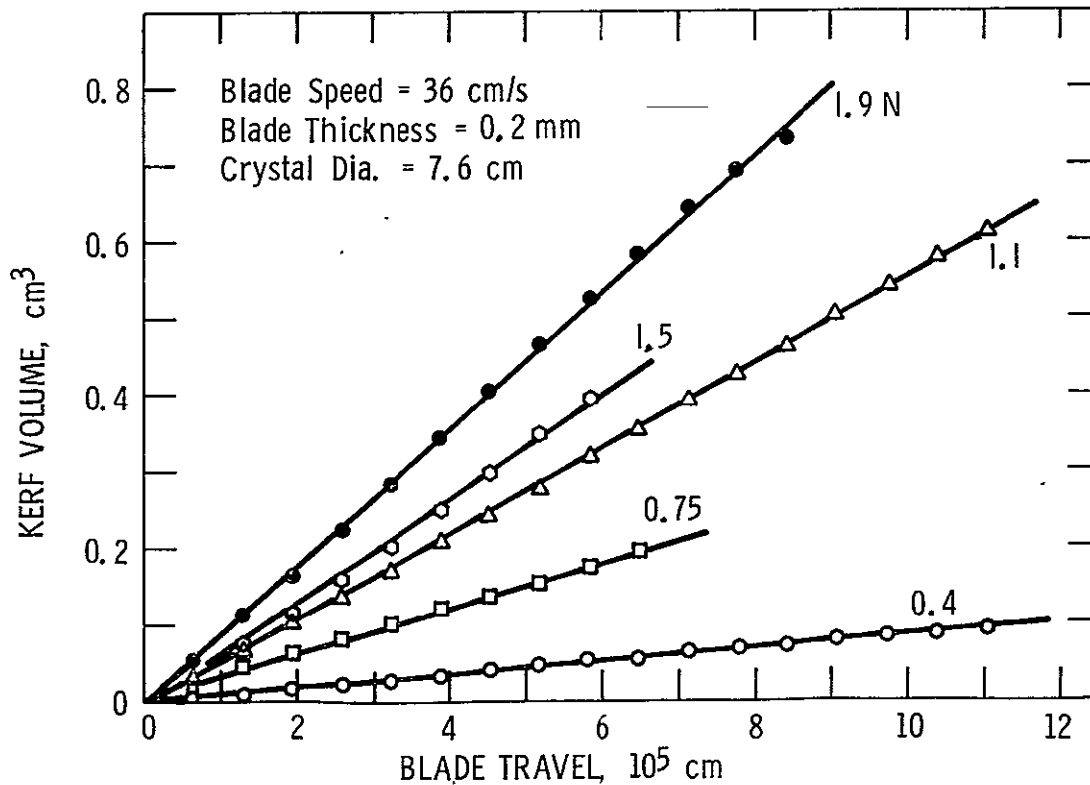


Figure 13. Silicon Kerf Volume versus Blade Travel as a Function of Blade Load

TABLE 3
SLURRY SAWING EXPERIMENT SUMMARY

Experiment No. 1

Experiment Description Blade Load vs. Cutting Rate

Material Sawed 7.64 cm Silicon - 15.7 cm long (111)

Abrasive 400 Grit SiC Crystolon

Slurry Mixture 240 g/liter PC oil

Slurry Flow Rate (ml/s) 42

Blade Material 1095 steel

Blade Dimensions (mm) Length: 412.8 Thickness 0.2 Height 6.4

Blade Spacer Thickness (mm) 0.74 No. Blades in Array: 167

Blade Elongation (mm) 2.95 Elongation (%) 0.71

Stroke Length (cm) 20 Head Reciprocation (cycles/min) 56

Blade Speed (cm/s) 38 Slice + Kerf (mm) 0.94

Blade Load (g/blade): 38, 76, 114 Blade Wear (mm) 1.6

Cycle Time (h): 32.5 Avg. Cutting Rate (mm/h) 2.35

No Slices Sawed 166 Sawing Yield (%) 94.0

Slice Thickness (mm): Avg. 0.60 Max 0.62 Min 0.58

Max Surface Planarity (μm) 12.7 Avg. Kerf Loss (mm) 0.34

Bow (μm) Avg 2.8 Max 25.4 Min 0

Taper (μm) Avg 52.3 Max 62.0 Min 34.8

Comments: Mount Wax - Cenco, Crystal mounted on 5 cm wide glass plate. Slices started clustering when blade array entered glass.

TABLE 4
SLURRY SAWING EXPERIMENT SUMMARY

Experiment No. 2

Experiment Description Blade Load vs. Cutting Rate

Material Sawed 7.65 cm Silicon - 16.2 cm Long (111)

Abrasive: 400 Grit SiC Crystolon

Slurry Mixture 240 g/liter PC oil

Slurry Flow Rate (ml/s) 42

Blade Material 1095 steel

Blade Dimensions (mm) Length 412.8 Thickness 0.2 Height 6.4

Blade Spacer Thickness (mm) 0.74 No Blades in Array: 172

Blade Elongation (mm) 2.95 Elongation (%) 0.71

Stroke Length (cm): 20 Head Reciprocation (cycles/min) 56

Blade Speed (cm/s) 38 Slice + Kerf (mm) 0.94

Blade Load (g/blade) 114, 152, 190 Blade Wear (mm) 1.6

Cycle Time (h): 19 Avg Cutting Rate (mm/h) 4.03

No Slices Sawed 171 Sawing Yield (%) 100

Slice Thickness (mm) Avg 0.60 Max 0.62 Min 0.55

Max Surface Planarity (μm) 30.5 Avg. Kerf Loss (mm) 0.34

Bow (μm) Avg 8.6 Max 33.0 Min 0

Taper (μm) Avg 52.3 Max 96.5 Min 7.6

Comments: Clustering of slices with 4 to 6 slices per cluster.

Experiment 3. High-Speed Sawing

A 7.65-cm crystal was sawed as in Exps. 1 and 2. The blade array used in Exp. 2 was used in this experiment (1.6-mm blade wear) with no additional tensioning. The stroke length was 20.0 cm at 88 cycles/min. Kerf volume versus blade travel is plotted in Figure 14. The average slice thickness was 0.60 mm with an average kerf of 0.34 mm. Cycle time for cutting was 6.9 hours but the cutting had to be terminated prematurely due to slices demounting. A possible cause was vibration from the rapid reciprocation rate.

Experiment 4. Cutting Rate for Three Crystals

Three 5.08-cm diameter crystals with a length (each section) of 15.2 cm were mounted in a special stainless steel mounting fixture shown in Figure 15. The crystals were attached to phenolic strips using epoxy cement. The stroke length was 16.5 cm at 70 cycles/min. This gave a blade speed equivalent to the previous experiments. The blade thickness was 0.2 mm with a spacer thickness of 0.74 mm. The average slice thickness was 0.59 mm with an average kerf of 0.35 mm. Additional data on Exp. 4 are given in Table 5. Total cycle time was 16 hours using various blade loads (1.1 N, 1.9 N, and 2.3 N/blade). Figure 16 shows kerf volume versus blade travel for these three blade

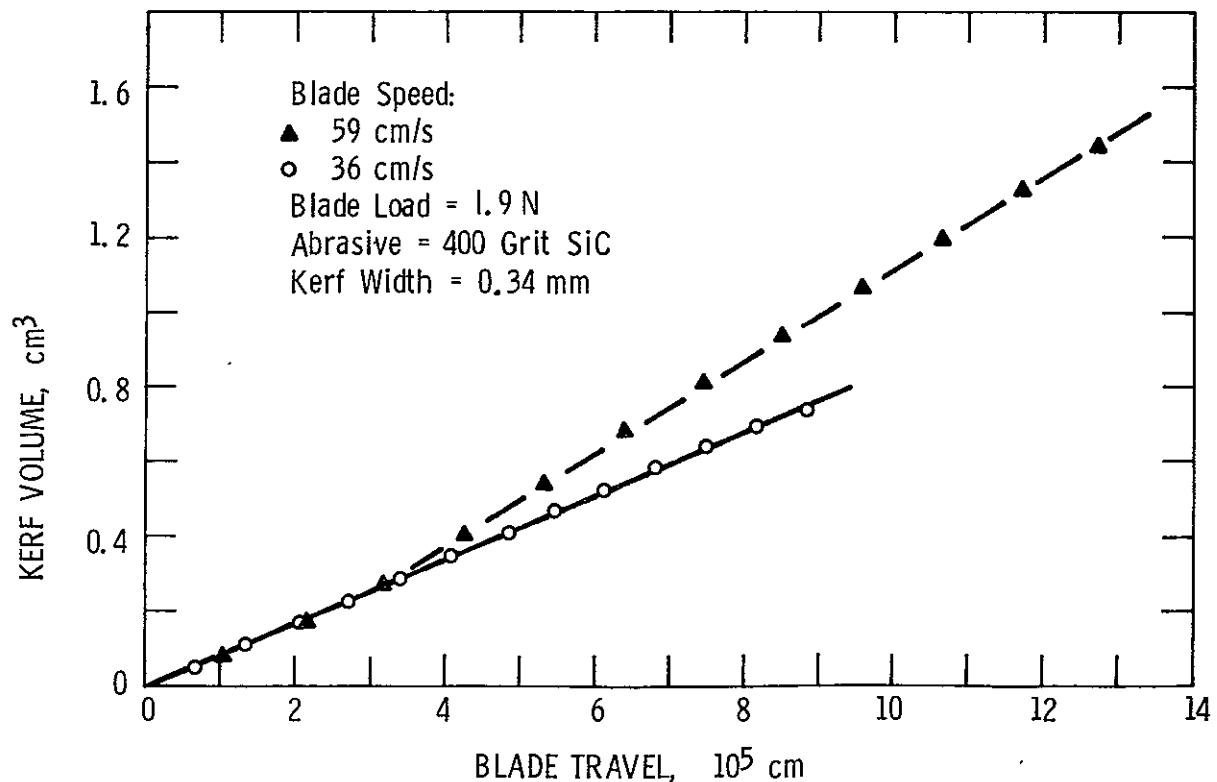


Figure 14. Kerf Volume versus Blade Travel as a Function of Blade Speed

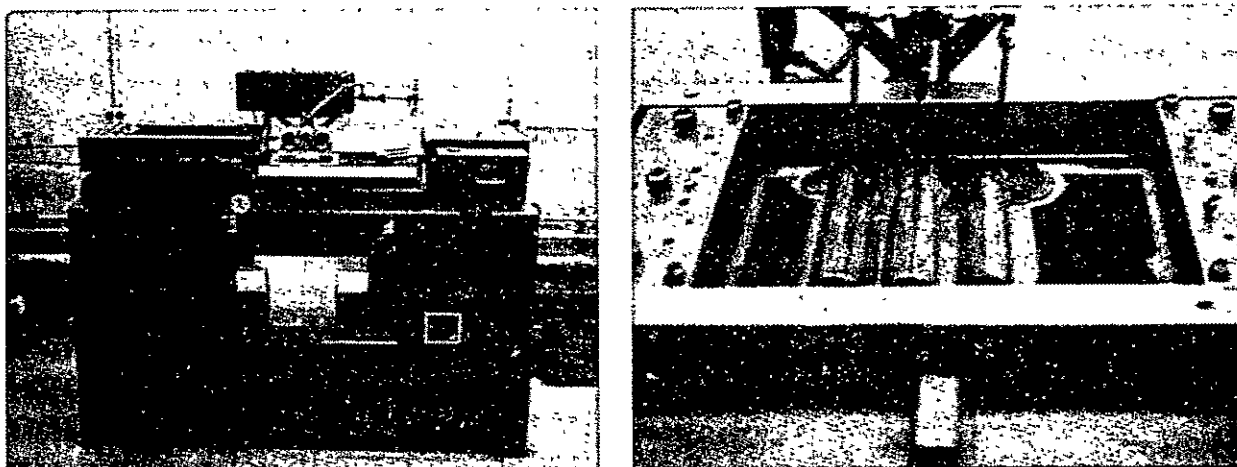


Figure 15. Slurry-Sawing Three 5.0-cm Crystals Simultaneously

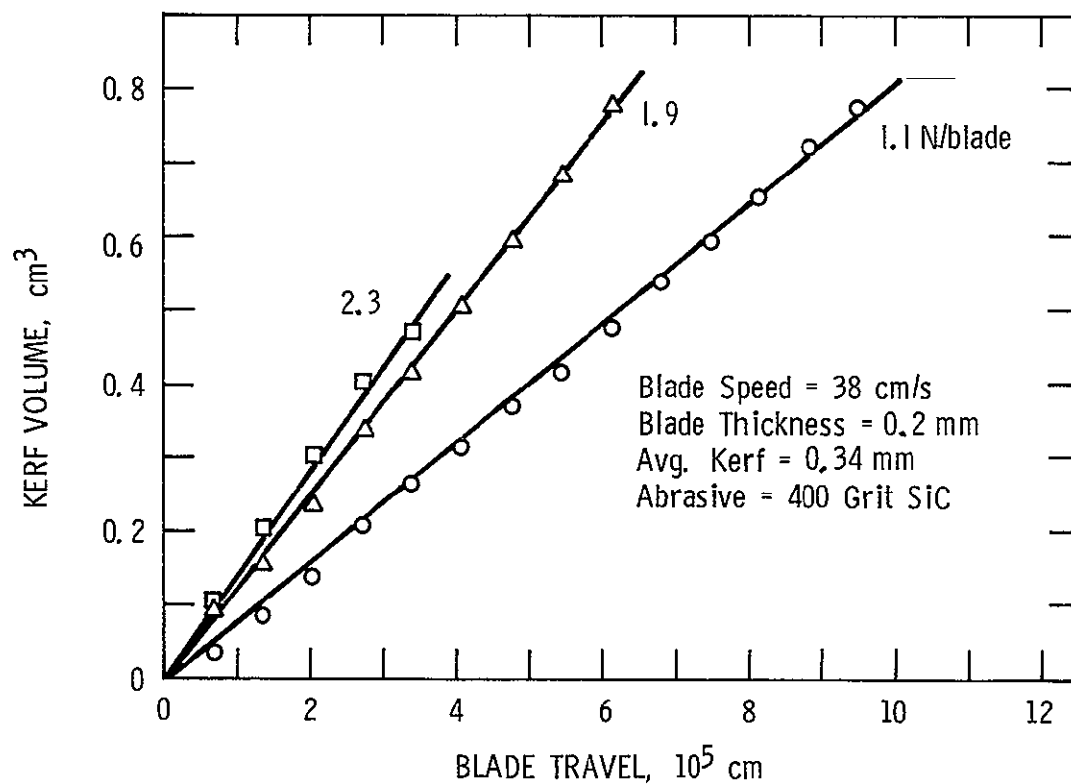


Figure 16. Simultaneous Sawing of Three 5-cm Silicon Crystals

TABLE 5
SLURRY SAWING EXPERIMENT SUMMARY

Experiment No.:	4
Experiment Description:	Three Crystals vs. Cutting Rate
Material Sawed:	5.08 cm Silicon - 15.24 cm Long (45.7 total)
Abrasive:	400 Grit SiC Crystolon
Slurry Mixture:	240 g/liter PC oil
Slurry Flow Rate (ml/s)	34
Blade Material:	1095 steel
Blade Dimensions (mm): Length	412.8 Thickness 0.2 Height 6.4
Blade Spacer Thickness (mm):	0.74 No. Blades in Array: 162 x 3 = 486
Blade Elongation (mm)	2.95 Elongation (%): 0.71
Stroke Length (cm)	16.5 Head Reciprocation (cycles/min.): 70
Blade Speed (cm/s):	38.5 Slice + Kerf (mm) 0.94
Blade Load (g/blade)	114, 190, 230 Blade Wear (mm): 1.65
Cycle Time (h)	16.0 Avg. Cutting Rate (mm/h): 3.17
No. Slices Sawed	483 Sawing Yield (%) 99.6
Slice Thickness (mm): Avg.	0.54 Max. 0.63 Min. 0.56
Max. Surface Planarity (μm):	12.5 Avg. Kerf Loss (mm): 0.36
Bow (μm): Avg.	2.4 Max. 20.3 Min. 0
Taper (μm) Avg.	48.3 Max. 80.0 Min. 14.0
Comments	Used Thermoset DC 412, 10 parts by weight and Thermoset Hardner DC 412, 1 part by weight for crystal mount.

TABLE 6
SLURRY SAWING EXPERIMENT SUMMARY

Experiment No.	10
Experiment Description:	Three Crystal vs. Cutting Rate
Material Sawed	5.08 cm Silicon (111) 15.22 cm Long
Abrasive	400 Grit SiC Crystolon
Slurry Mixture	240 g SiC/liter PC oil
Slurry Flow Rate (ml/s)	39
Blade Material:	1095 steel
Blade Dimensions (mm): Length	412.8 Thickness: 0.2 Height 6.4
Blade Spacer Thickness (mm):	0.74 No. Blades in Array: 162 x 3 = 486
Blade Elongation (mm):	2.95 Elongation (%) 0.71
Stroke Length (cm)	16.5 Head Reciprocation (cycles/min) 70
Blade Speed (cm/s)	38.5 Slice + Kerf (mm) 0.94
Blade Load (g/blade)	50, 150 Blade Wear (mm) 1.6
Cycle Time (h):	23.5 Avg. Cutting Rate (mm/h): 2.13
No. Slices Sawed	483 Sawing Yield (%) 98.6
Slice Thickness (mm): Avg	0.59 Max. 0.62 Min. 0.56
Max. Surface Planarity (μm):	12.5 Avg. Kerf Loss (mm): 0.35
Bow (μm) Avg.	4.83 Max. 17.8 Min. 0.0
Taper (μm): Avg.	19.81 Max. 61.5 Min. 4.32
Comments:	Reproduced data (cutting rate) of Experiment 4.

the end of this experiment it was noticed that the blade speed was considerably less than that initially set. The data from this experiment showed that cutting rate was greater than that of silicon carbide but a decision was made to repeat the experiment because of the blade speed problem.

Experiment 7. Cutting Rate versus Blade Force Using Boron Carbide (Repeat of Exp. 6)

The 7.62-cm crystal was mounted using epoxy adhesive and a phenolic strip. Crystal length was 16 cm. The blade array and other parameters including the slurry were the same as in Exp. 6. Kerf removal rate versus blade load is shown in Figure 18. Boron carbide abrasive produces a cutting rate 2.5 times greater than silicon carbide with the same blade load and blade speed. The average slice thickness was 0.60 mm with a kerf of 0.34 mm which were the same values as the silicon carbide results.

This experiment was terminated prematurely based on cutting rates dropping to nearly zero when the blade array touched the epoxy adhesive. When the crystal was taken off the mount fixture, it lacked 2.5 mm being cut into complete slice form. No additional slice parameter data other than thickness and kerf loss were taken.

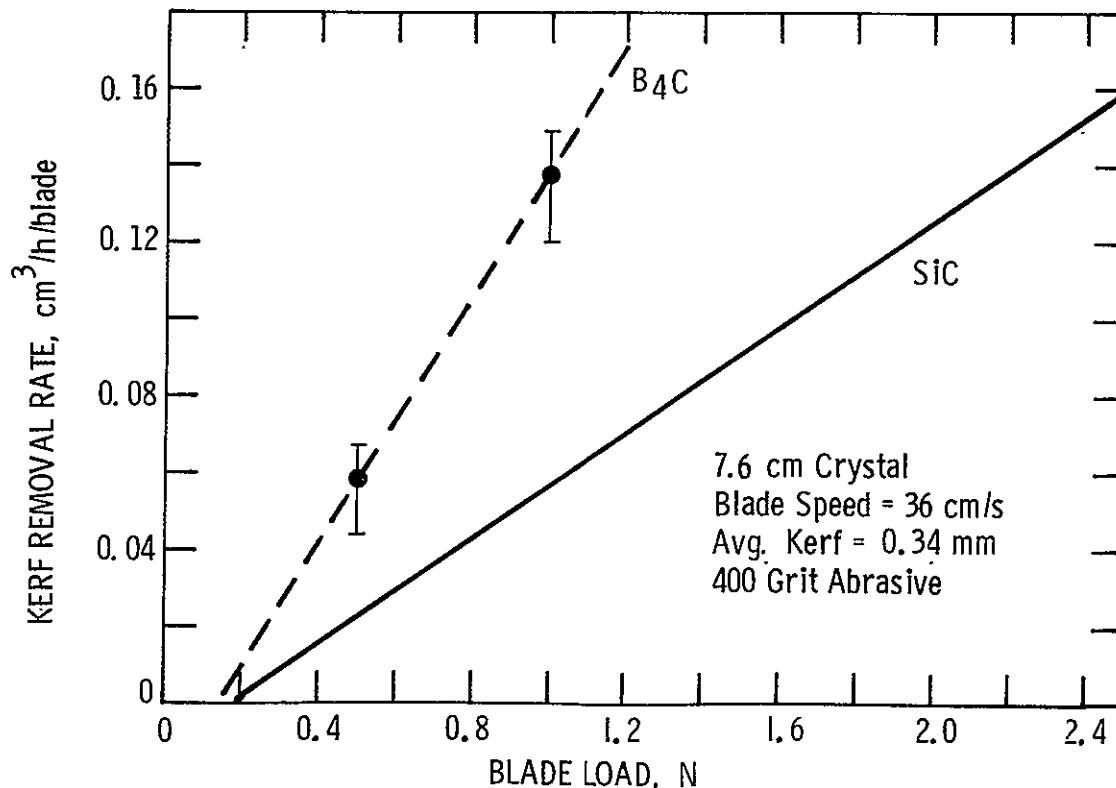


Figure 18. Boron Carbide Abrasive Slurry Sawing Results

Experiment 8. Thin Blades and Spacers

This crystal was 7.64 cm in diameter mounted as in Exp. 1. The blade thickness was 0.15 mm with a spacer thickness of 0.38 mm. The stroke length was 20.0 cm at 56 cycles/min. Initial blade load was 0.5 N/blade but when the blade load was increased to 1 N/blade, severe slice chippage and breakage began to occur. This experiment was terminated after cutting through approximately 3 cm of the crystal. Slice thicknesses on broken segments indicated 0.15 to 0.20 mm (6-8 mils).

Experiment 9. Slice Plus Kerf Thickness 0.63 mm (6-mil Blades and 19-mil Spacers)

A 7.62-cm crystal was mounted as in Exp. 1. The blade thickness was 0.15 mm and a 0.48-mm spacer thickness was used. The stroke length was 20.0 cm at 56 cycles/min. The blade array consisted of only 30 blades. The initial blade load was 0.5 N, so for a 30-blade array the pressure delta to the saw balance pressure of 1.73×10^5 Pa was 8.27×10^3 Pa. The cutting rate would decay with each additional 30-minute time interval to almost zero. The feed mechanism was lowered and then raised and this would produce the original cutting rate but with time it would decay to almost zero. This experiment proved that the Varian 686 saw feed mechanism is not sensitive enough to use small numbers of blades in the blade array. The blade pressure was varied from 0.5 to 2.5 N with questionable cutting rates still existing at the highest blade load. Data from this experiment were voided.

Experiment 10. Cutting Rate for Three Crystals (Repeat of Exp. 4)

In view of the results of Exp. 4, i.e., cutting rate is independent of kerf length, the 3-crystal experiment was repeated using blade loads of 0.5 and 1.5 N. Three 5.08-cm diameter crystals with a length (each section) of 15.22 cm were mounted as in Exp. 4 (Figure 15). In Exp. 4 the crystal orientation was $\langle 111 \rangle$, whereas in this experiment the crystals were $\langle 100 \rangle$. The stroke length was 16.5 cm at 70 cycles/min. The blade thickness was 0.2 mm with a spacer thickness of 0.74 mm. The average slice thickness was 0.59 mm with an average kerf of 0.35 mm, the same as in Exp. 4. The two data points (triangles) are plotted in Figure 17 and additional data are given in Table 6.

Experiment 11. Effect of Slurry Flow Rate on Cutting Speed

A 7.6-cm diameter $\langle 111 \rangle$ silicon crystal was slabbed into a rectangular cross section 4.4 by 5.8 cm. The resulting uniform kerf length allowed a direct comparison of cutting distance into the crystal with equal time increments. Three 30-blade arrays were assembled into the blade head for this experiment. The blade thickness was 0.15 mm with a spacer thickness of 0.48 mm. The stroke length was 20.0 cm at 56 cycles/min providing a blade speed of 38 cm/s. The blade load was 1.5 N/blade. Cutting rate as a function of slurry flow rate is plotted in Figure 19 (circles). Additional data are given in Table 7. The data in Figure 19 for this experiment indicate that a slurry flow rate in the 5 to 10 ml/s range is probably optimal, at least for boron carbide abrasive.

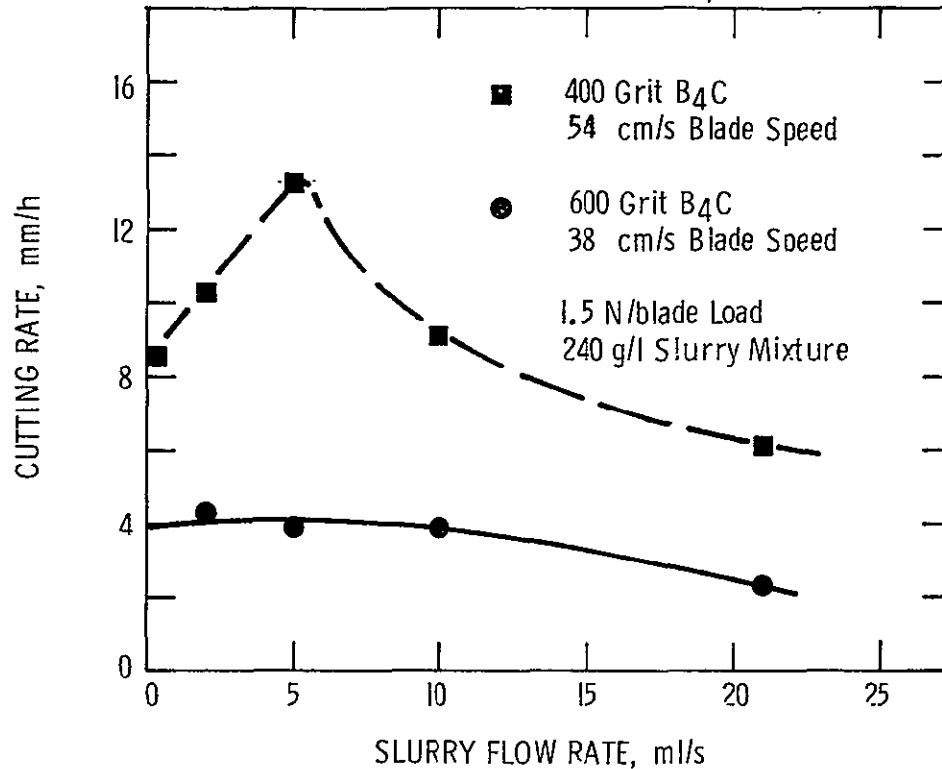


Figure 19. Effect of Slurry Flow Rate on Silicon Cutting Rate

Experiment 12. High-Speed Sawing by Combining Best Conditions

A 7.66-cm diameter $\langle 111 \rangle$ silicon crystal was mounted as in Exp. 1. The blade array consisted of 135 blades 0.2 mm thick with 0.48 mm spacers. The stroke length was 20.0 cm at 80 cycles/min. The slurry was 400-grit boron carbide in the ratio of 240 g/l PC oil. Blade force was 1.9 N/blade. The resulting slice thickness was 0.33 mm with an average kerf of 0.35 mm. Additional data are given in Table 8. The crystal was sliced in 7.2 h for an average cutting rate of 10.6 mm/h.

Experiment 13. High-Speed Sawing at 2.4 N per Blade

This experiment was basically a repeat of Exp. 12 except a higher blade force was used. The average slice thickness was 0.37 mm with an average kerf of 0.31 mm. Additional data are given in Table 9. The 7.62-cm diameter crystal was sliced in 6.2 h for an average cutting rate of 12.3 mm/h.

Experiment 14. Rotating Crystal (190 rpm)

Equipment was designed and built to accommodate rotation of the silicon crystal during the cutting process. An alignment fixture (Figure 20) was built which enabled the epoxy attachment of metal end assemblies to the crystal. The crystal rotated on a shaft attached to these end assemblies. A Heller motor and timing belt, shown in Figure 21, were used to rotate the crystal at 190 rpm

TABLE 7
SLURRY SAWING EXPERIMENT SUMMARY

Experiment No. 11

Experiment Description: Slurry Flow Rate vs. Cutting Rate

Material Sawed: Rectangular Crossection - Kerf 5.78 cm

Abrasive: 600 Grit B₄C - Norbide

Slurry Mixture: 240 g B₄C/liter PC oil

Slurry Flow Rate (ml/s): 21 to 2

Blade Material 1095 steel

Blade Dimensions (mm): Length: 412.8 Thickness: 0.15 Height 6.4

Blade Spacer Thickness (mm): 0.48 No. Blades in Array 90

Blade Elongation (mm) 2.54 Elongation (%): 0.71

Stroke Length (cm): 20 Head Reciprocation (cycles/min): 56

Blade Speed (cm/s): 38 Slice + Kerf (mm) 0.63

Blade Load (g/blade) 150 Blade Wear (mm) 1.53

Cycle Time (h) 15.5 Avg. Cutting Rate (mm/h): --

No. Slices Sawed: Not Applicable Sawing Yield (%) --

Slice Thickness (mm) Avg. -- Max -- Min. --

Max. Surface Planarity (μm) -- Avg Kerf Loss (mm) --

Bow (μm) Avg -- Max -- Min. --

Taper (μm) Avg -- Max. -- Min --

Comments At low flow rates (<10 mils/s) slices seem to cluster much sooner than at higher flows.

TABLE 8
SLURRY SAWING EXPERIMENT SUMMARY

Experiment No. 12

Experiment Description: High Speed Sawing - Combine Best Conditions

Material Sawed 7.66 cm Silicon (111)

Abrasive: 400 Grit B₄C - Microabrasive

Slurry Mixture 240 g B₄C/liter PC oil

Slurry Flow Rate (ml/s). 5

Blade Material 1095 steel

Blade Dimensions (mm) Length 412.8 Thickness: 0.2 Height. 6.4

Blade Spacer Thickness (mm) 0.48 No. Blades in Array: 135

Blade Elongation (mm): 2.5 Elongation (%): 0.62

Stroke Length (cm): 20 Head Reciprocation (cycles/min): 80

Blade Speed (cm/s): 53.3 Slice + Kerf (mm) 0.68

Blade Load (g/blade) 190 Blade Wear (mm) 1.4

Cycle Time (h): 7.2 Avg. Cutting Rate (mm/h): 10.6

No. Slices Sawed 134 Sawing Yield (%) 97.8

Slice Thickness (mm) Avg 0.33 Max. 0.42 Min. 0.23

Max. Surface Planarity (μm) 37.5 Avg. Kerf Loss (mm): 0.35

Bow (μm) Avg. 19.3 Max. 35.56 Min. 0.0

Taper (μm) Avg. 35.3 Max 49.28 Min. 17.02

Comments Slices started clustering well before blade exit of crystal possibly due to low (5 ml/s) slurry flow.

TABLE 9
SLURRY SAWING EXPERIMENT SUMMARY

Experiment No. 13

Experiment Description: High Speed Sawing at 240 g Per Blade

Material Sawed: 7.62 cm Silicon (111)

Abrasive: 400 Grit B₄C - Microabrasive

Slurry Mixture: 240 g/liter PC oil

Slurry Flow Rate (ml/s): 5

Blade Material: 1095 steel

Blade Dimensions (mm) Length: 412.8 Thickness: 0.2 Height: 6.4

Blade Spacer Thickness (mm): 0.48 No. Blades in Array: 88

Blade Elongation (mm) 2.5 Elongation (%) 0.62

Stroke Length (cm): 20 Head Reciprocation (cycles/min): 80

Blade Speed (cm/s) 53.3 Slice + Kerf (mm): 0.68

Blade Load (g/blade) 240 Blade Wear (mm) 1.42

Cycle Time (h): 6.2 Avg. Cutting Rate (mm/h): 12.3

No. Slices Sawed: 87 Sawing Yield (%) 96.6

Slice Thickness (mm) Avg 0.37 Max. 0.46 Min 0.30

Max. Surface Planarity (μm): 12.5 Avg. Kerf Loss (mm): 0.31

Bow (μm): Avg. Not Applicable Max. Min.

Taper (μm) Avg. Not Applicable Max. Min.

Comments: Approximately 25 slices given to Array Assembly for
fabrication of cells.

TABLE 10
SLURRY SAWING EXPERIMENT SUMMARY

Experiment No. 16

Experiment Description: Unground Silicon Crystal

Material Sawed: (111) Silicon Diameter 8.0 - 8.12 cm

Abrasive: 400 Grit B₄C - Microabrasive

Slurry Mixture: 240 g/liter PC Oil

Slurry Flow Rate (ml/s) 5.0

Blade Material: 1095 Steel

Blade Dimensions (mm) Length: 381 Thickness: 0.20 Height 6.4

Blade Spacer Thickness (mm): 0.43 No. Blades in Array: 160

Blade Elongation (mm) 2.54 Elongation (%): 0.67

Stroke Length (cm): 16.5 Head Reciprocation (cycles/min.): 80

Blade Speed (cm/s): 44 Slice + Kerf (mm): 0.63

Blade Load (g/blade): 200 Blade Wear (mm) 1.42

Cycle Time (h) 9.6 Avg. Cutting Rate (mm/h): 8.5

No. Slices Sawed: 159 Sawing Yield (%): 77.5*

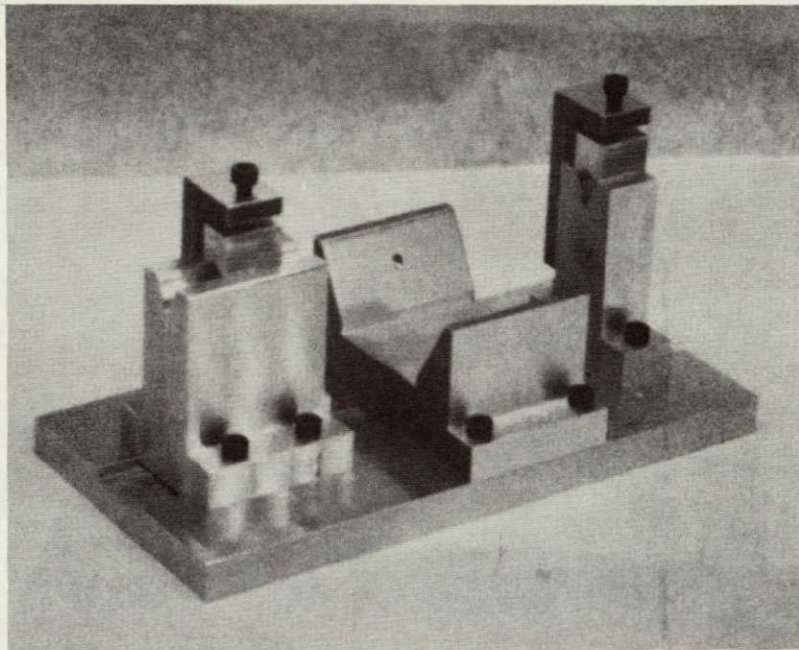
Slice Thickness (mm): Avg. 0.33 Max. 0.41 Min. 0.26

Max. Surface Planarity (μm): 15.0 Avg. Kerf Loss (mm): 0.30

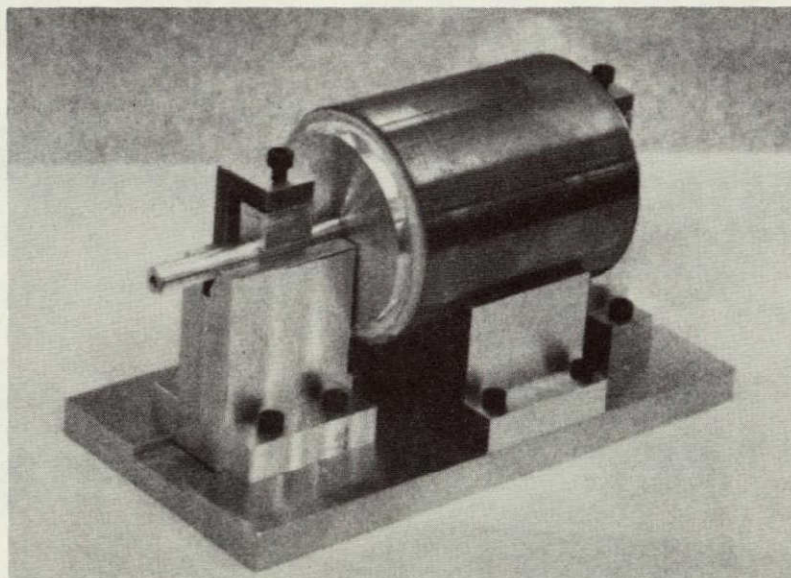
Bow (μm): Avg. 13.97 Max. 50.8 Min. 0.0

Taper (μm): Avg. 24.13 Max. 61.98 Min 4.32

Comments Employed light blade load for first 1.2 mm into crystal
* A number of slices broken due to use of three phenolic strips rather than 1.
The two additional strips were used as braces and epoxied to sides of crystal.
Also on first mount (single phenolic strip) phenolic broke causing two
large chips in top of crystal section.

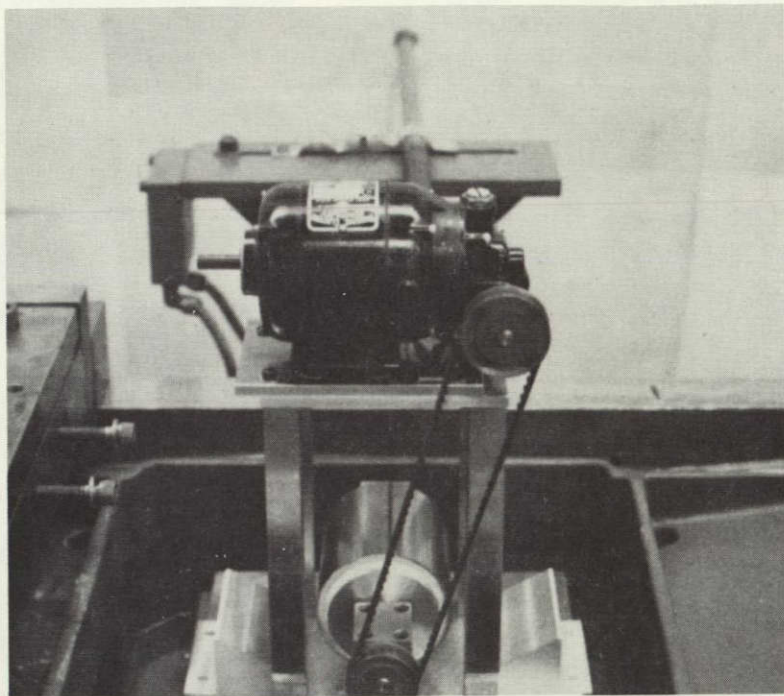


(a) CRYSTAL ALIGNMENT FIXTURE

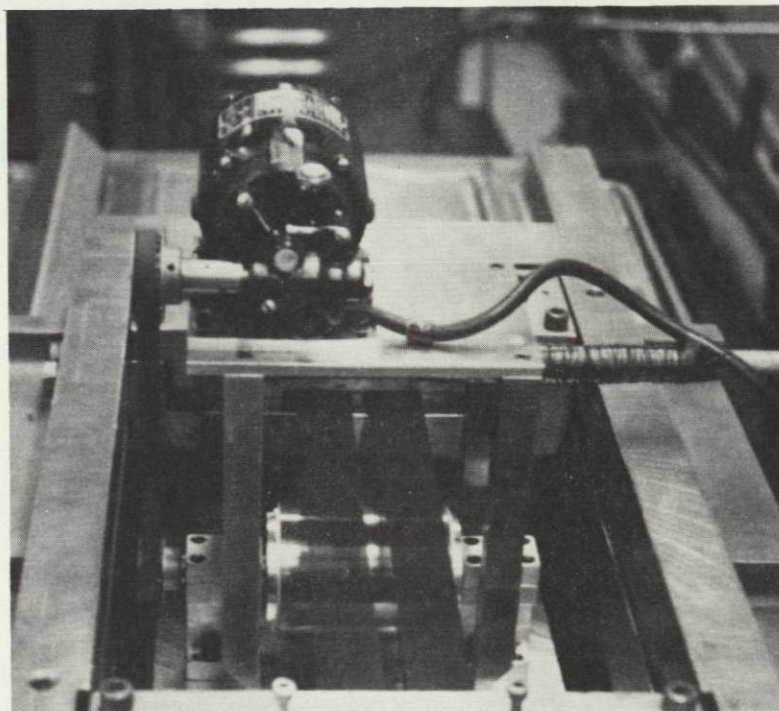


(b) CRYSTAL AND END MOUNTS IN
ALIGNMENT FIXTURE

Figure 20. Crystal Spinner Alignment Fixture



(a) CRYSTAL ROTATING SYSTEM
WITHOUT BLADE HEAD ASSEMBLY



(b) CRYSTAL ROTATING SYSTEM
READY FOR SLICING

Figure 21. Crystal Spinning System

while the blade head reciprocated. A blade load of 0.5 N was used with a stroke length of 20 cm at 56 cycles/min. The slurry was 400-grit B_4C in PC oil. After one hour of operation, the experiment had to be aborted due to a sharp momentary drop in the air pressure to the feed mechanism causing the crystal to drop and immediately return. This caused a major wipeout of the partially cut slices. It was determined from this experiment that a more powerful motor was needed. The spinning mechanism was returned to the shop for modifications.

Experiment 15. Cutting Rate versus Slurry Flow

This experiment was basically a repeat of Exp. 11. Boron carbide was used in both experiments, the difference being in the particle size – 600-grit in Exp. 11 and 400-grit in this experiment. Results of both these experiments are shown in Figure 19. Additional data are given in Table 10. The results of this experiment confirm the data from Exp. 11 that a flow rate of 5 ml/s is optimal. SEMs of new and used B_4C are shown in Figure 22 and SiC in Figure 23. Particle fragmentation and edge rounding occur with B_4C as with SiC but to a lesser degree. SEMs were taken of blades with a typical surface shown in Figure 24 and a blade from Exp. 1 (SiC) Figure 25. As was the case with SiC, no particle embedment was detected.

Experiment 16. Cutting an Unground Crystal

In all previous experiments the crystals were centerless ground to a specific diameter. The purpose of this experiment was to determine if an as-grown crystal with diameter undulations could be sliced. The conditions for the experiment are given in Table 10. The crystal had a diameter varying from 8.00 to 8.12 cm. The operating procedure was modified somewhat on startup to allow all blades in the array to seat onto the crystal surface before going to the full 2 N/blade loading. For this crystal, this was a cut distance of 0.6 mm from contact of the first blade in the array to all blades in the array. No problems with respect to slicing of the unground crystal were encountered by using the modified startup procedure.

Experiment 17. Rotating Crystal (850 rpm)

The modified spinning mechanism was again set up on the wafering machine with a 1.5-hp motor. A 7.66-cm $\langle 111 \rangle$ silicon crystal was mounted using the special fixture for centering the crystal end assemblies to enable rotation. The conditions for the experiment are given in Table 11. After approximately three hours of elapsed cutting time and a cut distance of 1.63 cm, the last blade in the assembly rode up on the end section of the crystal and caused a wipeout of a major portion of the partially cut slices. The experiment was abandoned, but slice and kerf thickness data were taken and cutting rate is plotted in Figure 26.

TABLE 11
SLURRY SAWING EXPERIMENT SUMMARY

Experiment No.: 17

Experiment Description: Rotating Crystal (850 rpm)

Material Sawed: 7.66 cm (111) Silicon

Abrasive: 600 Grit B₄C - Microabrasive

Slurry Mixture: 240 g B₄C/liter PC Oil

Slurry Flow Rate (ml/s): 10 - 25

Blade Material: 1095 Steel

Blade Dimensions (mm): Length: 381 Thickness: 0.2 Height: 12.7

Blade Spacer Thickness (mm): 0.48 No. Blades in Array: 89

Blade Elongation (mm): 2.54 Elongation (%): 0.67

Stroke Length (cm): 19 Head Reciprocation (cycles/min.): 60

Blade Speed (cm/s): 38 Slice + Kerf (mm): 0.68

Blade Load (g/blade): 100 Blade Wear (mm): Not measured

Cycle Time (h): --- Avg. Cutting Rate (mm/h): ---

No. Slices Sawed: --- Sawing Yield (%): ---

Slice Thickness (mm): Avg. --- Max. --- Min. ---

Max. Surface Planarity (μ m): --- Avg. Kerf Loss (mm): ---

Bow (μ m): Avg. --- Max. --- Min. ---

Taper (μ m): Avg. --- Max. --- Min. ---

Comments: Abort - Rear blade rode up on top of crystal. Broke all partially cut slices.

TABLE 12
SLURRY SAWING EXPERIMENT SUMMARY

Experiment No.: 18

Experiment Description: Rotating Crystal (850 rpm)

Material Sawed: 7.63 cm (111) Silicon

Abrasive: 400 Grit SiC - Norton

Slurry Mixture: 240 g/liter PC Oil

Slurry Flow Rate (ml/s): 10 - 25

Blade Material: 1095 Steel

Blade Dimensions (mm): Length: 381 Thickness: 0.2 Height: 6.35

Blade Spacer Thickness (mm): 0.48 No. Blades in Array: 111

Blade Elongation (mm): 2.54 Elongation (%): 0.67

Stroke Length (cm): 19 Head Reciprocation (cycles/min.): 60

Blade Speed (cm/s): 38 Slice + Kerf (mm): 0.68

Blade Load (g/blade): 50, 100, 150 Blade Wear (mm): 2.24

Cycle Time (h): 4.75 h for 3.1 cm Avg. Cutting Rate (mm/h): ---

No. Slices Sawed: 110 Sawing Yield (%): 0

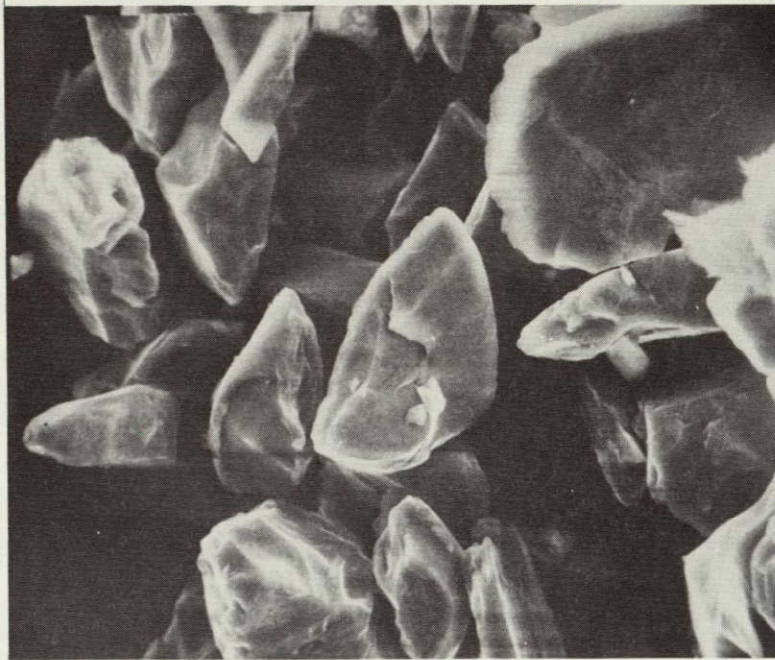
Slice Thickness (mm): Avg. --- Max. --- Min. ---

Max. Surface Planarity (μ m): --- Avg. Kerf Loss (mm): ---

Bow (μ m): Avg. --- Max. --- Min. ---

Taper (μ m): Avg. --- Max. --- Min. ---

Comments: Lost all slices after rotation stopped to slice core region. Partially cut slices were not supported adequately for core cutting.

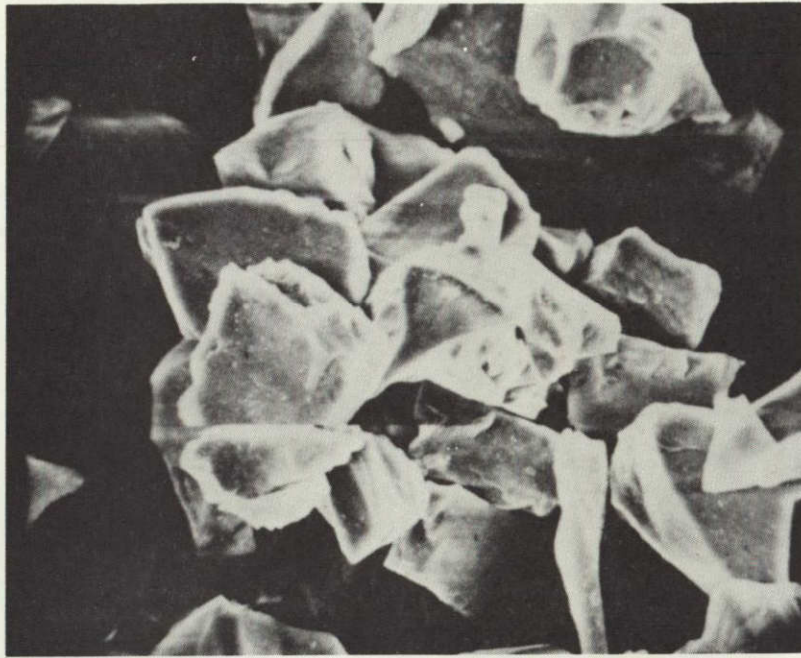


(a) 1000X NEW ABRASIVE

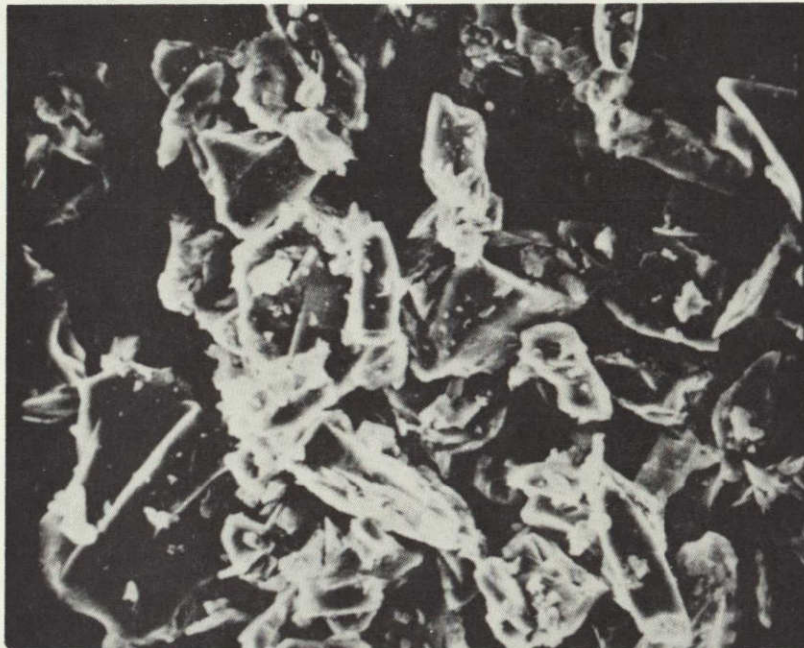


(b) 1000X USED ABRASIVE

Figure 22. SEMs of New and Used 400-Grit B₄C Abrasive



(a) 1000x New Abrasive



(b) 1000x Used Abrasive

Figure 23. SEMs of New and Used 400-Grit SiC Abrasive

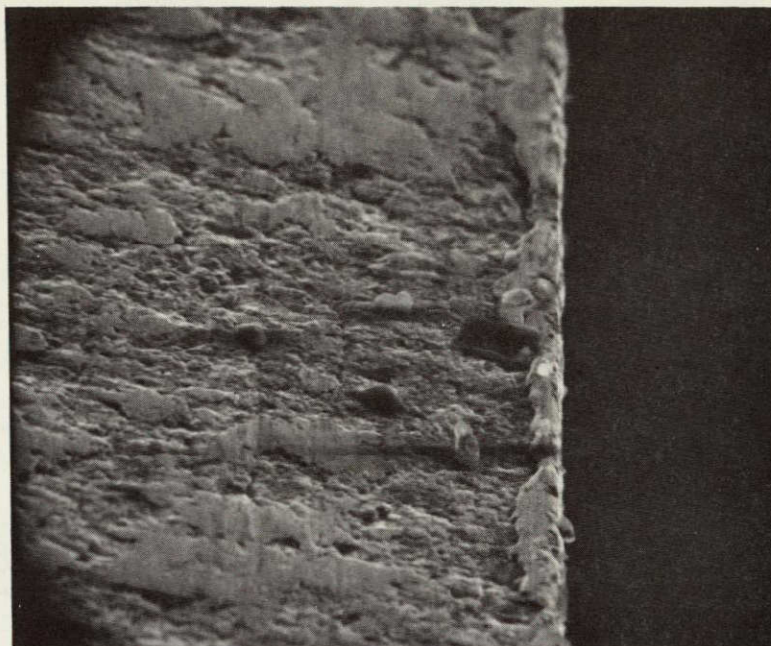


Figure 24. SEM of Blade from Experiment 15 – 400-Grit B_4C (500X)



25 μ

Figure 25. SEM (500X) of Blade After Cutting 7.6-cm Silicon Crystal Using
SiC-PC Oil Slurry (Blade from Experiment 1)

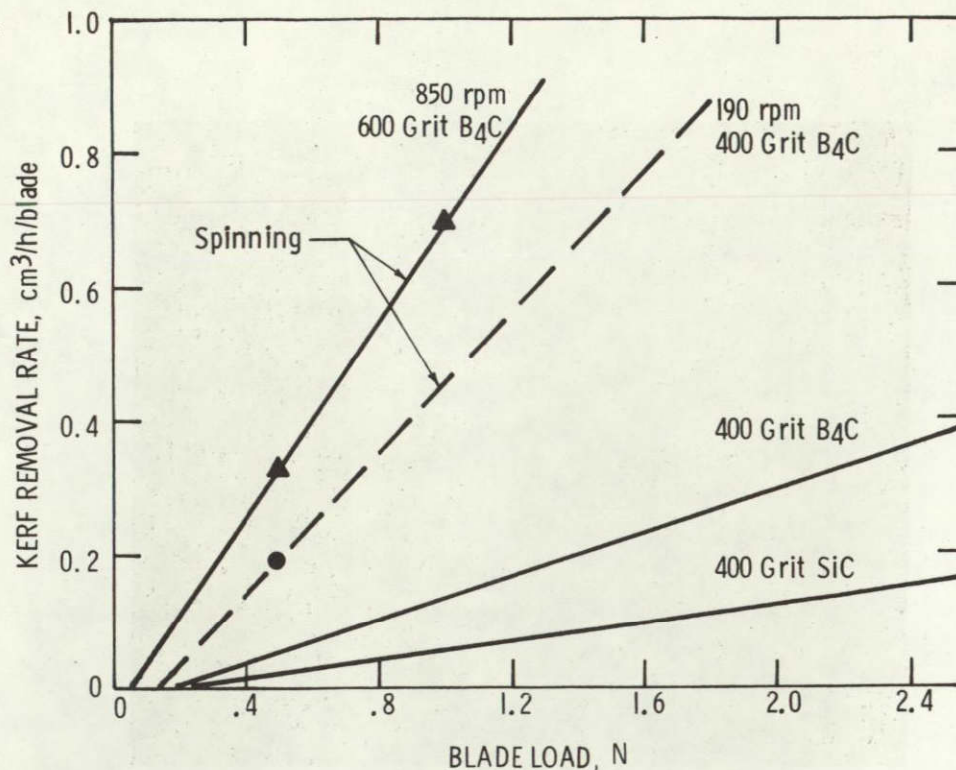


Figure 26. Experimental Slurry Sawing Results

Experiment 18. Rotating Crystal (850 rpm)

In the analysis of what may have caused the problem in Exp. 17, it was thought that the blade height (12.7 mm) could have been a contributing factor. In setting up for this experiment, a blade array was assembled using 6.35-mm high blades. Other conditions are given in Table 12. Initial blade loading was 0.5 N/blade for a cut distance of 1.48 cm, then a change was made to 1.0 N/blade to a cut distance of 3.14 cm. At this point, the crystal rotation was stopped, crystal supports were installed, and the remaining core was cut with the crystal stationary. Difficulty was encountered in the final 0.25 cm of the crystal core because the crystal and partially cut slices were not anchored firmly enough. Cutting rates with the 400-grit SiC virtually identical to those shown in Figure 26 for 600-grit B₄C.

Experiment 19. Abrasive Concentration versus Cutting Rate

The conditions and results of this experiment are given in Table 13. The abrasive concentration was increased from 240 g/l to 480 g/l. The kerf loss was exceptionally low (0.225 mm) in this experiment and was probably due to a statistical accident in that many slices were broken (possibly thin ones) in cleanup thus contributing to a thicker slice average – hence lower kerf. Indications were that cutting rate was about 1.5 times faster for the same blade loading with double (480 g/l PC oil) abrasive concentration.

Experiment 20. Diamond-Plated Blades

Diamond-plated blades were purchased from Semiconductor Materials Incorporated. The process used for plating was their Mark III which incorporates 3 parts 325-grit diamond with 1 part 270-grit diamond. The diamond plating was approximately 0.064-mm thick per side with a cutting edge thickness of 0.152 to 0.203 mm. Table 14 summarizes experimental results. Figure 27 shows the core/diamond interface with the core being high tensile strength stainless steel. The Mark III process with this particular diamond particle mix is one that is used for making ID wheels and was considered a good place to start for multiblade wafering.

Coolant for the diamond blades was a Rustlick/water mixture (1:20) at a flow rate of 5-10 ml/s. Additional data are shown in Table 14. The blade load at startup was 0.3 N/blade and was increased to 2.4 N/blade. The cutting rate increased with blade loading but was no better than abrasive cutting at equivalent pressures. Also, slice evaluation revealed that the blades began to wander after exceeding 0.9 N/blade, thus contributing to a wide spread in thickness, high bow, and taper. Figure 28 shows a surface view of a slice sawed with the diamond blades. Note that the surface has a semipolished appearance which is not characteristic of diamond ID wheel cutting.

Experiment 21. Rotating Crystal – Diamond-Plated Blades

The same blade package used in Exp. 20 and the crystal spinning mechanism used in Exp. 17 were used in this experiment. A 7.66-cm (111) silicon crystal was mounted as in Exp. 17. Other experimental conditions are given in Table 15. A significant improvement in cutting rate was obtained with the diamond blades and crystal rotation. Crystal rotation was stopped at a core diameter of 1.65 cm. At this point, the crystal was heated by a hot air gun and a bead of liquid Rigidax was poured over the top of the partially cut crystal. Crystal supports were placed beneath the crystal and liquid Rigidax was applied along the supports and allowed to solidify.

Figure 29 shows the surfaces of one of the slices produced in this experiment. Note the surface texture produced during crystal rotation versus the core texture. The slice surface produced during crystal rotation now looks much like an ID sawed surface but the core has a polished look. Total cycle time was 3.8 hours.

Experiment 22. 12-cm Crystal – Diamond Blades

The same diamond-blade package used in Exps. 20 and 21 was used in this experiment. The crystal was mounted with wax on a glass plate. As in Exp. 20, cutting rate was very slow. A number of variations in the coolant were tried in hopes of determining what could be contributing to the slow cutting rate with the crystal stationary. For example, 15% KOH solution and 10% HF solution

TABLE 13
SLURRY SAWING EXPERIMENT SUMMARY

Experiment No.: 19

Experiment Description: Abrasive Concentration vs. Cutting Rate

Material Sawed: 7.66 cm (111) Silicon

Abrasive: 400 Grit SiC - Crystolon

Slurry Mixture: 480 g/liter PC Oil

Slurry Flow Rate (ml/s): 5

Blade Material: 1095 Steel

Blade Dimensions (mm): Length: 381 Thickness: 0.15 Height: 6.35

Blade Spacer Thickness (mm): 0.43 No. Blades in Array: 177

Blade Elongation (mm): 2.54 Elongation (%): 0.67

Stroke Length (cm): 20 Head Reciprocation (cycles/min.): 56

Blade Speed (cm/s): 38 Slice + Kerf (mm): 0.58

Blade Load (g/blade): 100, 150, 200 Blade Wear (mm): 1.93

Cycle Time (h): 12.0 Avg. Cutting Rate (mm/h): 6.2

No. Slices Sawed: 176 Sawing Yield (%): 75.6

Slice Thickness (mm): Avg. 0.357 Max. 0.426 Min. 0.233

Max. Surface Planarity (μ m): 55.9 Avg. Kerf Loss (mm): 0.225

Bow (μ m): Avg. 11.43 Max. 25.4 Min. 0.0

Taper (μ m): Avg. 75.44 Max. 127.0 Min. 21.59

Comments: No explanation for low kerf loss with 480 g/liter of 400 grit SiC unless due to many slices getting broken in cleanup and skewing slice thickness data to the high side.

TABLE 14
SLURRY SAWING EXPERIMENT SUMMARY

Experiment No.: 20

Experiment Description: Diamond Blades

Material Sawed: 7.63 cm Silicon (111)

Abrasive: Plated Diamond Blades (SMI)

Slurry Mixture: Water/Rustlick (20 : 1)

Slurry Flow Rate (ml/s): 5 - 10

Blade Material: Diamond Plated on Stainless Steel, SMI Mark III Process

Blade Dimensions (mm): Length: 381 Thickness: 0.29 Height: 12.7

Blade Spacer Thickness (mm): 0.74 No. Blades in Array: 50

Blade Elongation (mm): 2.7 Elongation (%): 0.7

Stroke Length (cm): 20 Head Reciprocation (cycles/min.): 80

Blade Speed (cm/s): 53 Slice + Kerf (mm): 0.89

Blade Load (g/blade): 30, 60, 90, 150, 210, 240 Blade Wear (mm): None

Cycle Time (h): 12.8 Avg. Cutting Rate (mm/h): 5.80

No. Slices Sawed: 49 Sawing Yield (%): 32.7

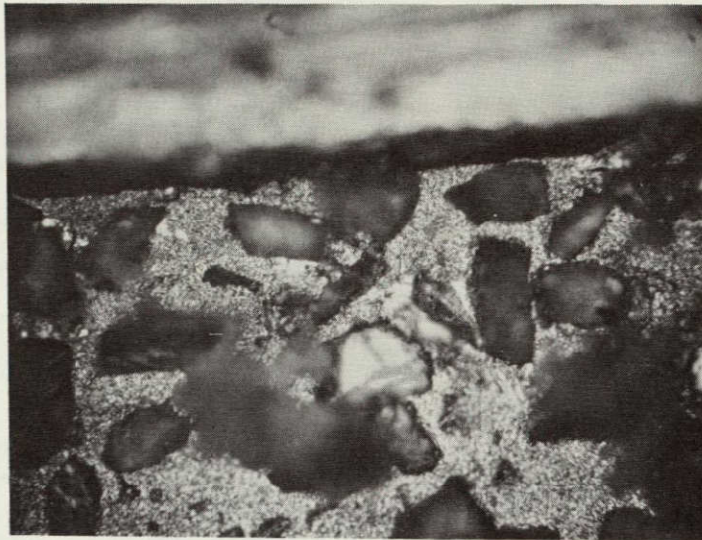
Slice Thickness (mm): Avg. 0.595 Max. 0.789 Min. 0.340

Max. Surface Planarity (μ m): 25.0 Avg. Kerf Loss (mm): 0.294

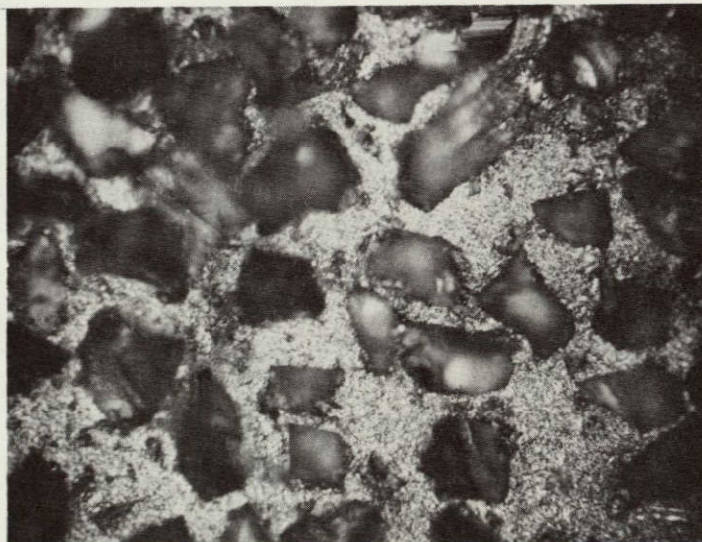
Bow (μ m): Avg. 51.82 Max. 109.2 Min. 12.7

Taper (μ m): Avg. 79.50 Max. 132.8 Min. 44.7

Comments: At 150 g blade load and up developed considerable blade wander as reflected in slice thickness uniformity, bow, taper.



(a) DIAMOND PLATED BLADE INTERFACE
BETWEEN CORE (TOP) AND DIAMOND (BOTTOM)



(b) DIAMOND PLATED BLADE

Figure 27. Photomicrographs of Diamond Blade Cutting Surface (240X)

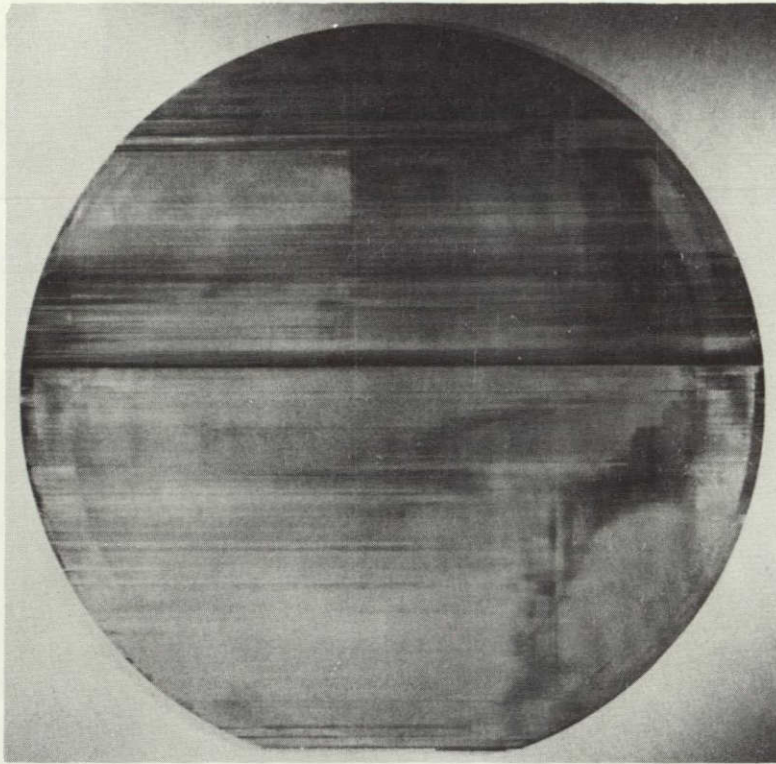


Figure 28. Slice From Experiment 20 Cut with Diamond-Plated Blades

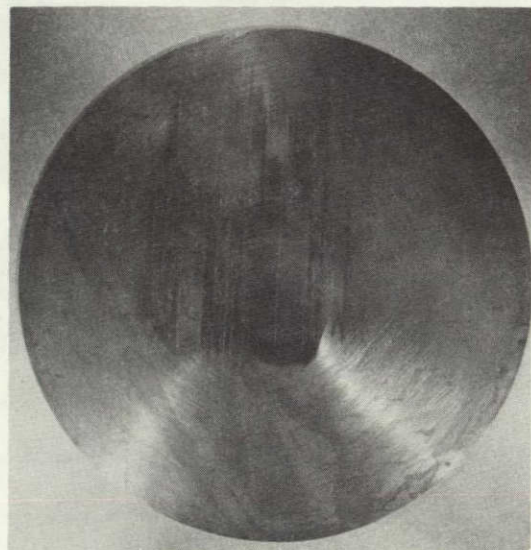
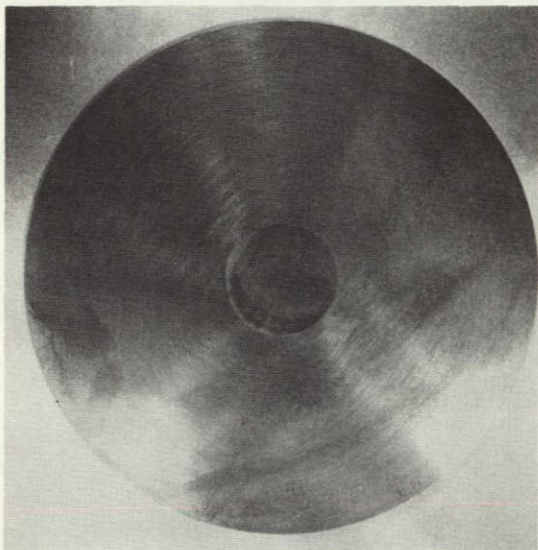


Figure 29. Surfaces of Both Sides of a Slice from Experiment 21

TABLE 15
SLURRY SAWING EXPERIMENT SUMMARY

Experiment No.: 21

Experiment Description: Rotating Crystal - Diamond Blades

Material Sawed: (111) Silicon 7.66 cm Diameter

Abrasive: Plated Diamond Blades (SMI)

Slurry Mixture: Water/Rustlick (20 : 1)

Slurry Flow Rate (ml/s): 5-10

Blade Material: Diamond Plated on Stainless Steel, SMI Mark III Process

Blade Dimensions (mm): Length: 381 Thickness: 0.29 Height: 12.7

Blade Spacer Thickness (mm): 0.74 No. Blades in Array: 50

Blade Elongation (mm): 2.7 Elongation (%): 0.7

Stroke Length (cm): 18 Head Reciprocation (cycles/min.): 80

Blade Speed (cm/s): 48 Slice + Kerf (mm): 0.89

Blade Load (g/blade): 30, 90, 120*, 180* Blade Wear (mm): None

Cycle Time (h): 3.9 Avg. Cutting Rate (mm/h): 19.6

No. Slices Sawed: 49 Sawing Yield (%): 89.8

Slice Thickness (mm): Avg. 0.60 Max. 0.90 Min. 0.36

Max. Surface Planarity (μ m): 37.0 Avg. Kerf Loss (mm): 0.30

Bow (μ m): Avg. 42.2 Max. 71.1 Min. 5.1

Taper (μ m): Avg. 75.4 Max. 144.0 Min. 17.3

Comments: Crystal rotated until core dimension was 16.5 mm. Rotation stopped, Rigidax applied, core sliced.

* 120 g and 180 g per blade load for cutting core.

TABLE 16
SLURRY SAWING EXPERIMENT SUMMARY

Experiment No.: 23

Experiment Description: Rotating Crystal - Diamond

Material Sawed: 7.66 cm (111) Silicon

Abrasive: Plated Diamond Blades (SMI)

Slurry Mixture: Water/Rustlick (20 to 1)

Slurry Flow Rate (ml/s): 5 - 10

Blade Material: Diamond Plated Blades SMI Mark III Process

Diamond 0.29

Blade Dimensions (mm): Length: 381 Thickness: Core 0.15 Height: 12.7

Blade Spacer Thickness (mm): 0.74 No. Blades in Array: 50

Blade Elongation (mm): 2.7 Elongation (%): 0.7

Stroke Length (cm): 18 Head Reciprocation (cycles/min.): 80

Blade Speed (cm/s): 48 Slice + Kerf (mm): 0.89

Blade Load (g/blade): --- Blade Wear (mm): ---

Cycle Time (h): --- Avg. Cutting Rate (mm/h): ---

No. Slices Sawed: --- Sawing Yield (%): ---

Slice Thickness (mm): Avg. --- Max. --- Min. ---

Max. Surface Planarity (μ m): --- Avg. Kerf Loss (mm): ---

Bow (μ m): Avg. --- Max. --- Min. ---

Taper (μ m): Avg. --- Max. --- Min. ---

Comments: After 30 minutes (> 12.5 mm into crystal) of cutting time elapsed experienced total wipeout of partial slices.

were substituted for the standard Rustlick/water mixture in an effort to etch off any silicon buildup on the blades. Also, two SiC dressing sticks (320 grit) were attached to each side of the crystal. None of the above made an impact on the slow cutting rate so the experiment was terminated.

Experiment 23. Rotating Crystal – Diamond Blades

Again, the same diamond blade package used in Exps. 20, 21, and 22 was used in this experiment. Detailed data are given in Table 16. After the diamond blades were well seated (2 minutes), the blade load was increased from 0.3 to 0.9 N. In 30 minutes, the cut depth had exceeded 1.27 cm with the crystal rotating at 850 rpm. This indicated again, as in Exp. 21, that blade travel speed was a key factor with this diamond matrix. This experiment was terminated prematurely due to catastrophic slice breakage.

Experiment 24. Thin (0.43 mm) Spacer Blade Package

A 7.64-cm $\langle 111 \rangle$ silicon crystal was mounted as in Exp. 1. The blade array consisted of 162 blades 0.20-mm thick with 0.43-mm spacers. The slurry was 600-grit B₄C in the ratio of 240 g/l PC oil. Blade load was varied from 0.5 to 2.5 N/blade in 0.5-N increments. The resulting slice thickness plus kerf was 0.63 mm. Additional data are given in Table 17. Cycle time was 13.0 hours.

Experiment 25. Thin (0.36 mm) Spacer Blade Package

A 7.65-cm $\langle 111 \rangle$ silicon crystal was mounted with wax on a glass plate. The blade array consisted of 140 blades 0.20-mm thick with 0.36-mm spacers. The slurry was 600-grit SiC in a ratio of 240 g/l PC oil. Blade load was increased from 0.5 to 2.0 N/blade in 0.5-N increments. The resulting slice thickness plus kerf was 0.56 mm with a saw yield of 100%. Rigidax was used in this experiment after a cut depth of 3 cm. Additional data are given in Table 18. Total cycle time was 23 hours.

Experiment 26. Abrasive Sawing of 12-cm Crystal

A 12-cm $\langle 111 \rangle$ silicon crystal was mounted with wax on a glass plate. The blade array consisted of 139 blades 0.20 mm thick with 0.36-mm spacers. The slurry was 400 grit B₄C in a ratio of 480 g/l PC oil. Blade load was increased from 0.5 to 2.0 N/blade in 0.5-N increments. After a cut depth of 3 cm, a Rigidax bead was used to retain slices in position. The resulting slice thickness plus kerf was 0.56 mm with a saw yield of 100%. Total cycle time was 19.8 hours for an average cutting rate of 6.1 mm/h. Additional data are given in Table 19. Figure 30 shows the crystal at two stages of cutting with the Rigidax applied and Figure 31 depicts completed slices.

TABLE 17
SLURRY SAWING EXPERIMENT SUMMARY

Experiment No.: 24

Experiment Description: 0.43 mm Spacer - B₄C Abrasive

Material Sawed: 7.64 cm (III) Silicon

Abrasive: 600 Grit B₄C - Microabrasive

Slurry Mixture: 240 g B₄C/liter PC Oil

Slurry Flow Rate (ml/s): 5

Blade Material: 1095 Steel

Blade Dimensions (mm): Length: 381 Thickness: 0.20 Height: 6.35

Blade Spacer Thickness (mm): 0.43 No. Blades in Array: 162

Blade Elongation (mm): 2.5 Elongation (%): 0.65

Stroke Length (cm): 20 Head Reciprocation (cycles/min.): 56

Blade Speed (cm/s): 37 Slice + Kerf (mm): 0.63

Blade Load (g/blade): 50, 100, 150, 200, 250 Blade Wear (mm): ---

Cycle Time (h): 13.0 Avg. Cutting Rate (mm/h): 5.9

No. Slices Sawed: 161 Sawing Yield (%): 100

Slice Thickness (mm): Avg. 0.37 Max. 0.45 Min. 0.31

Max. Surface Planarity (μm): Not Available Avg. Kerf Loss (mm): 0.27

Bow (μm): Avg. 11.7 Max. Min.

Taper (μm): Avg. --- Max. Min.

Comments: Added Bead of Rigidax after cutting 25.4 mm. Slices had minor chipping as blade exited crystal.

TABLE 18
SLURRY SAWING EXPERIMENT SUMMARY

Experiment No.: 25

Experiment Description: 0.36 mm Spacer - SiC Abrasive

Material Sawed: 7.65 cm (III) Silicon

Abrasive: 600 grit SiC - Microabrasive

Slurry Mixture: 240 g/liter PC oil

Slurry Flow Rate (ml/s): 5

Blade Material: 1095 Steel

Blade Dimensions (mm): Length: 381 Thickness: 0.20 Height: 6.35

Blade Spacer Thickness (mm): 0.36 No. Blades in Array: 140

Blade Elongation (mm): 25 Elongation (%): 0.65

Stroke Length (cm): 20 Head Reciprocation (cycles/min.): 56

Blade Speed (cm/s): 37 Slice + Kerf (mm): 0.56

Blade Load (g/blade): 50, 100, 150, 200 Blade Wear (mm): ---

Cycle Time (h): 23 Avg. Cutting Rate (mm/h): 3.33

No. Slices Sawed: 139 Sawing Yield (%): 100

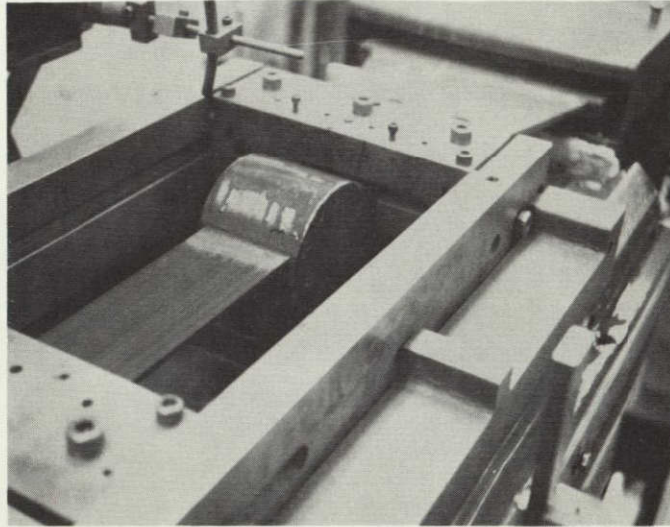
Slice Thickness (mm): Avg. 0.32 Max. 0.35 Min. 0.28

Max. Surface Planarity (μm): --- Avg. Kerf Loss (mm): 0.24

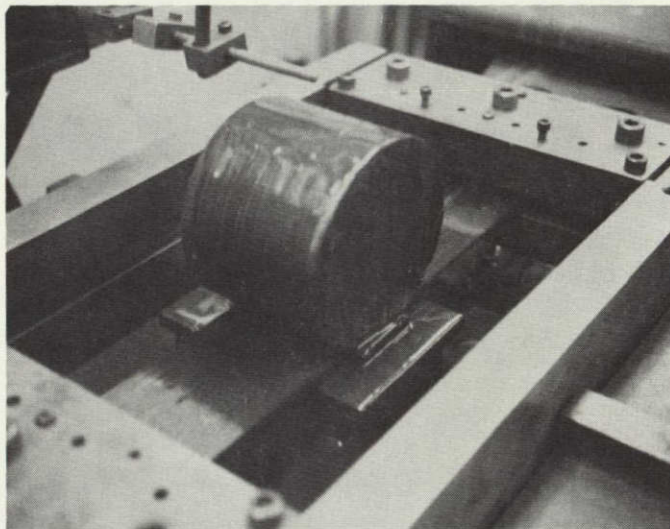
Bow (μm): Avg. 6.6 Max. Min.

Taper (μm): Avg. --- Max. Min.

Comments: Excellent results with 0.36 mm spacer - no slices lost.



(a) APPROXIMATELY 40% CUT THROUGH
NOTE RIGIDAX BEAD



(b) AT END OF CUTTING CYCLE

Figure 30. Experiment 16 — Sawing a 12-cm Crystal

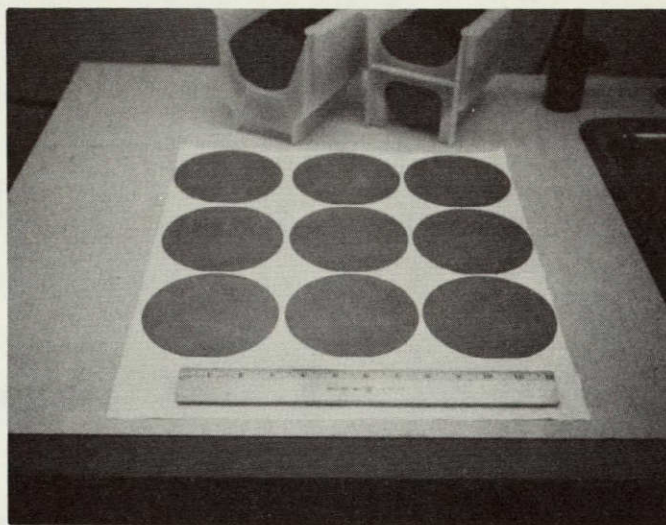


Figure 31. 12-cm Slices from Experiment 26 After Slice Cleanup

Experiment 27. 12-cm Crystal – 0.15 mm Blade

A 12-cm $\langle 111 \rangle$ silicon crystal was mounted with wax on a glass plate. The blade array consisted of 177 blades 0.15 mm thick with 0.43-mm spacers. The slurry was 600 grit SiC in a ratio of 480 g/l PC oil to 2.0 N/blade in 0.5-N increments. From a cut depth of 3 cm, excessive breakage occurred and the experiment was aborted at 5.5-cm depth.

Experiment 28. Diamond-Plated Blades

New diamond-plated blades were purchased from Semiconductor Materials, Inc. The process used for plating was their Mark III with a different diamond mix from that used in Exp. 20. The diamond mix was three parts 270 grit and one part 230 grit. The use of larger diamond particles required a thicker diamond plate. The diamond plating was about 0.11 mm thick per side, resulting in a cutting edge thickness of 0.36 to 0.38 mm. Table 20 summarizes other pertinent parameters. The cutting rate was so slow (0.71 mm/h at 3.0 N/blade force) that the experiment was terminated.

TABLE 19
SLURRY SAWING EXPERIMENT SUMMARY

Experiment No.: 26

Experiment Description: 12 cm Diameter Crystal

Material Sawed: (111) Silicon - 12 cm Diameter (JPL 12-4)

Abrasive: 400 Grit B₄C - Microabrasive

Slurry Mixture: 480 g/liter PC oil

Slurry Flow Rate (ml/s): 10

Blade Material: 1095 steel

Blade Dimensions (mm): Length: 412.8 Thickness: 0.20 Height: 6.35

Blade Spacer Thickness (mm): 0.36 No. Blades in Array: 139

Blade Elongation (mm): 2.54 Elongation (%): 0.65

Stroke Length (cm): 20 Head Reciprocation (cycles/min.): 56

Blade Speed (cm/s): 38 Slice + Kerf (mm): 0.56

Blade Load (g/blade): 50 to 200 Blade Wear (mm): 3.1

Cycle Time (h): 19.8 Avg. Cutting Rate (mm/h): 6.06

No. Slices Sawed: 138 Sawing Yield (%): 100

Slice Thickness (mm): Avg. 0.32 Max. 0.37 Min. 0.26

Max. Surface Planarity (μm): 25.4 Avg. Kerf Loss (mm): 0.24

Bow (μm): Avg. Not Available Max. -- Min. --

Taper (μm): Avg. 44.5 Max. 122.7 Min. 16.0

Comments: Slice surfaces looked great - ESI thought they were lapped. Experienced problems with microcracks at slice periphery.

TABLE 20
SLURRY SAWING EXPERIMENT SUMMARY

Experiment No.: 28

Experiment Description: Diamond-Plated Blades - Stationary Crystal

Material Sawed: (111) Silicon - 7.6 cm Diameter

Abrasive: Plated Diamond Blades (SMI)

Slurry Mixture: Water-Rustlick 20 to 1

Slurry Flow Rate (ml/s): 5 - 10

Blade Material: Stainless Steel Core, SMI Mark III Process

Blade Dimensions (mm): Length: 381 Diamond Thickness: 0.37 Height: 12.7
Core t = 0.15 mm

Blade Spacer Thickness (mm): 0.48 No. Blades in Array: 70

Blade Elongation (mm): 2.7 Elongation (%): 0.7

Stroke Length (cm): 20 Head Reciprocation (cycles/min.): 80

Blade Speed (cm/s): 48 Slice + Kerf (mm): ---

Blade Load (g/blade): 20 to 250 Blade Wear (mm): ---

Cycle Time (h): --- Avg. Cutting Rate (mm/h): ---

No. Slices Sawed: --- Sawing Yield (%): ---

Slice Thickness (mm): Avg. --- Max. --- Min. ---

Max. Surface Planarity (μm): --- Avg. Kerf Loss (mm): ---

Bow (μm): Avg. --- Max. --- Min. ---

Taper (μm): Avg. --- Max. --- Min. ---

Comments: Diamonds were 230/270 mixture (large than Exp. 20) but cutting rate so slow that experiment was terminated.

Experiment 29. Diamond-Plated Blades – Rotating Crystal (850 rpm)

A 7.63-cm $\langle 111 \rangle$ silicon crystal was mounted for rotation. The same 70-blade array used in Exp. 28 was used for this experiment. Initial blade load was 0.3 N/blade. Before the blades reached a depth of 2.5 mm, a major breakage problem was encountered and the experiment had to be terminated. In reviewing the experiment, the problem was thought to be due to the thin spacers (0.48 mm) and thick diamond plate used in the array.

The larger diamond particles required a thicker diamond plating (0.11 mm/side) and hence both factors combined to produce a potential slice in the 0.24-0.26-mm range. A decision was made to disassemble the array and use 0.74-mm spacers (as was used in Exp. 20) in the next experiment with rotating crystal.

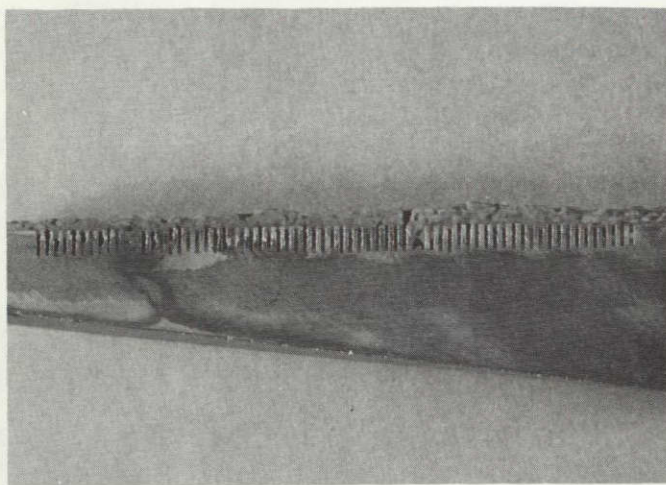
Experiment 30. Diamond-Plated Blades – Rotating Crystal (850 rpm), 0.74 mm Spacer

A 7.66-cm $\langle 111 \rangle$ silicon crystal was mounted for rotation. The blade array from Exp. 29 was disassembled and reassembled using 0.74-mm spacers. Initial blade pressure was 0.3 N/blade for the first 1.22 mm of cutting, then the pressure was increased to 0.9 N/blade. After a 2.92-mm cut depth, a major breakage problem was encountered and the experiment had to be terminated. Upon examination of the crystal, it appeared that the cause for breakage had started at the slice between blades 21 and 22. Blades 21 and 22 were examined visually and under the microscope for continuity of diamond plating and other anomalies. Both blades appeared to be in good condition. A cross section from the crystal was taken and examined for possible clues to the failure (Figures 30 and 31). Figure 32 showing this cross section does not indicate any obvious problem. It is interesting to note the variable cut depths of the individual blades due, probably, to vertical misalignment at blade pack assembly.

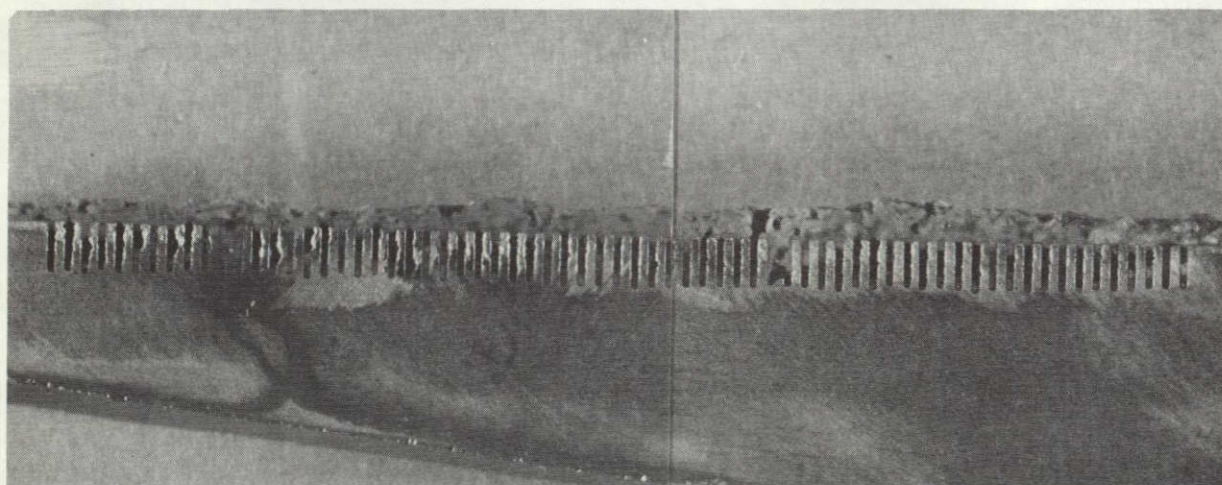
Experiment 31. Two 7.63-cm Silicon Crystals Cut Simultaneously

Two 7.63-cm $\langle 111 \rangle$ silicon crystals were wax-mounted side by side with a 2.5 mm separation between crystals. The blades used were 0.15 X 0.36 mm (total slice + kerf of 0.51 mm) with 155 blades in the array. The slurry was 480 g/l of 400 grit SiC in PC oil. The stroke length was 17.5 cm at 56 cycles/min. Blade loads from 0.3 to 2 N/blade were used. Considerable slice breakage was encountered and the experiment was terminated after cutting to a depth of 6.05 cm. A cutting rate of 5.02 mm/h was observed for 2 N/blade load, indicating as before that multiple crystals will cut at the same rate as a single crystal. This experiment also showed that two 7.6-cm crystals can be sawed simultaneously on the Varian multiblade saw with no modifications required.

ORIGINAL PAGE IS
OF POOR QUALITY



(a)



(b)

Figure 32. Cross Section From Experiment 30

Experiment 32. Abrasive Cutting of 12-cm Crystal

A 12-cm $\langle 100 \rangle$ crystal was mounted with wax on a glass plate. The blade array consisted of 136 blades 0.20 mm thick with 0.36-mm spacers. The slurry was 400-grit SiC in a ratio of 480 g/l PC oil. Blade load was increased 0.5 to 1.5 N/blade in 0.5-N increments. After a cut depth of 3.8 cm, a Rigidax bead was used to retain slices in position (Figure 33). The resulting slice thickness plus kerf was 0.56 mm with a saw yield of 93%. Total cycle time was 39.5 hours for an average cutting rate of 3.45 mm/h. Additional data are given in Table 21.

Experiment 33. Diamond Blades – Rotating Crystal

The same diamond blades as used in Exp. 28 were used in this experiment. The blades were cleaned and reassembled using 0.74-mm spacers rather than 0.48 mm as used in Exp. 28. The cutting proceeded without difficulty until a depth of 2.6 mm was reached. At this point a wipeout occurred and the experiment was terminated.

Experiment 34. Abrasive Cutting of 12-cm Crystal

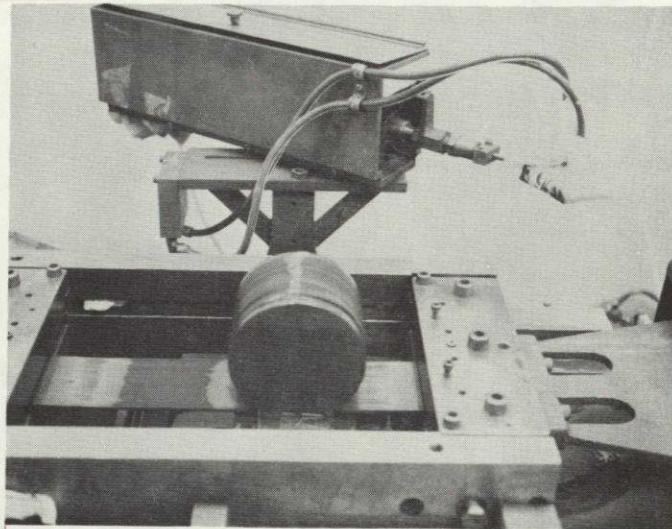
An 11.94-cm $\langle 100 \rangle$ silicon crystal was mounted with wax on a glass plate. The blade array consisted of 135 blades 0.20-mm thick with 0.36-mm spacers. The slurry was 400-grit SiC in a ratio of 480 g/l PC oil. Blade load was increased from 0.3 N to 2.0 N in 0.5-N increments. After a cut depth of 2.1 cm, a Rigidax bead was used to retain slices in position. The resulting slice thickness plus kerf was 0.56 mm with a saw yield of 76.1%. Total cycle time was 29 hours. Additional data are shown in Table 22.

Experiment 35. Unground Crystal – Thin Blades

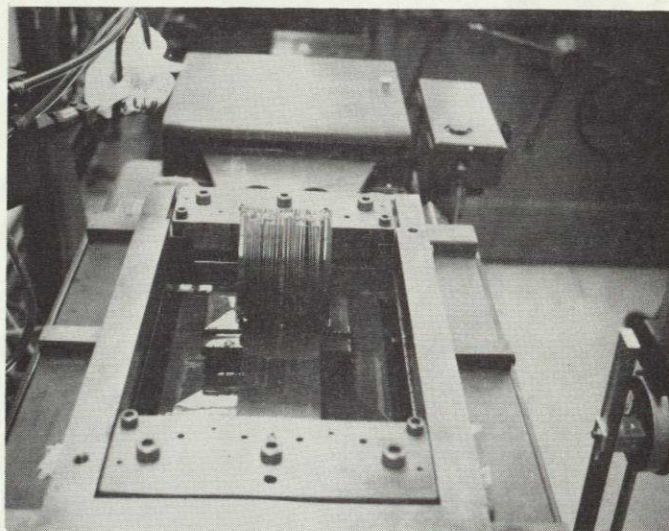
An unground $\langle 100 \rangle$ silicon crystal was mounted using epoxy and a graphite impregnated phenolic strip. The blade array consisted of 145 blades 0.15 mm thick with 0.35-mm spacer. The slurry was 400-grit SiC in a ratio of 500 g/l PC oil. Blade load was increased from 0.5 N to 1.5 N in 0.5 N increments. After a cut depth of 2.5 mm, a Cenco wax bead was used to retain slices in position. The resulting slice thickness plus kerf was 0.50 mm with a saw yield of 29.2%. Total cycle time was 22 hours. Slice breakage again was a major problem due to the thin (0.23 mm) slices and the thin blades. Table 23 presents a summary of this experimental run.

Experiment 36. Diamond Blades with Abrasive Slurry

A 7.46-cm $\langle 111 \rangle$ silicon crystal was mounted. The blade array consisted of the diamond blades used in Exp. 20. The slurry was 400-grit SiC in a ratio of 500 g/l PC oil. Blade load was increased from 0.5 N to 2.5 N in 0.5-N increments. After a cut depth of 7.19 cm, a blade broke and the



(a) END VIEW OF 12 cm CRYSTAL AFTER SLICING



(b) SIDE VIEW OF 12 cm CRYSTAL AFTER SLICING

Figure 33. Experiment 32

TABLE 21
SLURRY SAWING EXPERIMENT SUMMARY

Experiment No.: 32

Experiment Description: 12-cm Crystal

Material Sawed: <100> Silicon Crystal (JPL 12-14)

Abrasive: 400 Grit - SiC Microabrasive

Slurry Mixture: 480 g SiC/liter PC Oil

Slurry Flow Rate (ml/s): 5-10

Blade Material: 1095 Steel

Blade Dimensions (mm): Length: 381 Thickness: 0.20 Height: 6.4

Blade Spacer Thickness (mm): 0.36 No. Blades in Array: 136

Blade Elongation (mm): 2.5 Elongation (%): 0.65

Stroke Length (cm): 19.0 Head Reciprocation (cycles/min.): 60

Blade Speed (cm/s): 38.0 Slice + Kerf (mm): 0.56

Blade Load (g/blade): 30-150 Blade Wear (mm): 3.0

Cycle Time (h): 39.5 Avg. Cutting Rate (mm/h): 3.0

No. Slices Sawed: 13.5 Sawing Yield (%): 93

Slice Thickness (mm): Avg. 0.28 Max. 0.30 Min. 0.24

Max. Surface Planarity (μm): 12.5 Avg. Kerf Loss (mm): 0.28

Bow (μm): Avg. 38.1 Max. 53.3 Min. 25.4

Taper (μm): Avg. 49.5 Max. 65.0 Min. 36.0

Comments: Did not apply Rigidex until cut depth was 2.8 cm -- slices had clustered and showed signs of curvature.

TABLE 22
SLURRY SAWING EXPERIMENT SUMMARY

Experiment No.: 34

Experiment Description: 12-cm Crystal

Material Sawed: 11.94 cm <100> Silicon Crystal (JPL 12-24)

Abrasive: 400 Grit SiC Microabrasive

Slurry Mixture: 480 g/liter PC Oil

Slurry Flow Rate (ml/s): 5-10

Blade Material: 1095 Steel

Blade Dimensions (mm): Length: 412.8 Thickness: 0.20 Height: 6.35

Blade Spacer Thickness (mm): 0.36 No. Blades in Array: 135

Blade Elongation (mm): 2.54 Elongation (%): 0.65

Stroke Length (cm): 19 Head Reciprocation (cycles/min.): 60

Blade Speed (cm/s): 38 Slice + Kerf (mm): 0.56

Blade Load (g/blade): 30 to 200 Blade Wear (mm): 3.05

Cycle Time (h): 29 Avg. Cutting Rate (mm/h): 4.1

No. Slices Sawed: 134 Sawing Yield (%): 76.1

Slice Thickness (mm): Avg. 0.26 Max. 0.35 Min. 0.19

Max. Surface Planarity (μm): 37.7 Avg. Kerf Loss (mm): 0.30

Bow (μm): Avg. 30.5 Max. 43.2 Min. 5.1

Taper (μm): Avg. 39.1 Max. 43.7 Min. 32.3

Comments: Good surfaces.

TABLE 23
SLURRY SAWING EXPERIMENT SUMMARY

Experiment No.: 35

Experiment Description: Unground Crystal

Material Sawed: 8.9 cm <100> Silicon

Abrasive: 400 Grit SiC Microabrasive

Slurry Mixture: 500 g SiC/liter PC Oil

Slurry Flow Rate (ml/s): 5-10

Blade Material: 1095 Steel

Blade Dimensions (mm): Length: 412.8 Thickness: 0.15 Height: 6.4

Blade Spacer Thickness (mm): 0.35 No. Blades in Array: 145

Blade Elongation (mm): 2.54 Elongation (%): 0.65

Stroke Length (cm): 19 Head Reciprocation (cycles/min.): 60

Blade Speed (cm/s): 38 Slice + Kerf (mm): 0.50

Blade Load (g/blade): 50 to 150 Blade Wear (mm): 2.0

Cycle Time (h): 22 Avg. Cutting Rate (mm/h): 4.05

No. Slices Sawed: 144 Sawing Yield (%): 29.2

Slice Thickness (mm): Avg. 0.23 Max. 0.31 Min. 0.17

Max. Surface Planarity (μm): 37.7 Avg. Kerf Loss (mm): 0.27

Bow (μm): Avg. _____ Max. _____ Min. _____

Taper (μm): Avg. 42.4 Max. 96.3 Min. 8.3

Comments: Major problem was slice breakage.

TABLE 24
SLURRY SAWING EXPERIMENT SUMMARY

Experiment No.: 36

Experiment Description: Diamond Blades and Slurry

Material Sawed: 7.46 cm <111> Silicon

Abrasive: Diamond Blades (used in Exp. 20) and 400 Grit SiC

Slurry Mixture: 500 g SiC/liter PC Oil + Diamond Blades

Slurry Flow Rate (ml/s): 5-10

Blade Material: Stainless Steel

Blade Dimensions (mm): Length: 412.8 Thickness: core 0.15 Height: 12.7

Blade Spacer Thickness (mm): 0.74 No. Blades in Array: 47

Blade Elongation (mm): 2.71 Elongation (%): 0.7

Stroke Length (cm): 20.3 Head Reciprocation (cycles/min.): 60

Blade Speed (cm/s): 40.6 Slice + Kerf (mm): 0.89

Blade Load (g/blade): 50, 100, 150, 200, 250 Blade Wear (mm): None

Cycle Time (h): 15 Avg. Cutting Rate (mm/h): 4.97

No. Slices Sawed: -0- Sawing Yield (%): -0-

Slice Thickness (mm): Avg. 0.43 Max. 0.58 Min. 0.35

Max. Surface Planarity (μm): _____ Avg. Kerf Loss (mm): _____

Bow (μm): Avg. _____ Max. _____ Min. _____

Taper (μm): Avg. _____ Max. _____ Min. _____

Comments: Blade broke after a cut depth of 7.2 cm. Experiment was terminated. Diamond plate was gone on one end of array.

experiment was terminated. The cutting rate obtained with the combination of diamond-plated blades and slurry was 5 mm/h., which has been obtained with normal slurry sawing. Upon examination of the diamond blades, considerable diamond had been worn off especially at one end of the array. The diamond was completely gone on the broken blade which may have contributed to blade breakage. Table 24 summarizes data for this run.

3. Saw Blade Mechanics

Experiments with sawing using thin blades described above have indicated difficulties at blade thicknesses below 0.2 mm. The best yield accomplished to date with 0.15-mm blades was 76% observed in Exp. 19. One experiment tried with 0.1-mm blades was totally unsuccessful. In an effort to gain a better understanding of problems using thin blades, a stability analysis was performed to predict the critical blade load which would cause lateral buckling. Obviously, if lateral buckling were severe enough, the sideways movement of the blades could snap off the slices being sawed.

Figure 34 depicts a blade subjected to a load sufficient to cause buckling. Thin blades are subject to lateral buckling instability in which, at the critical load, the blade will twist and bow out in a direction normal to the applied load. The equations describing the blade shape of Figure 34 are:

$$EIu'' - Tu + (P/2)x\phi - M = 0 \quad (23)$$

$$C\phi'' - (P/2)u'' = 0 \quad (24)$$

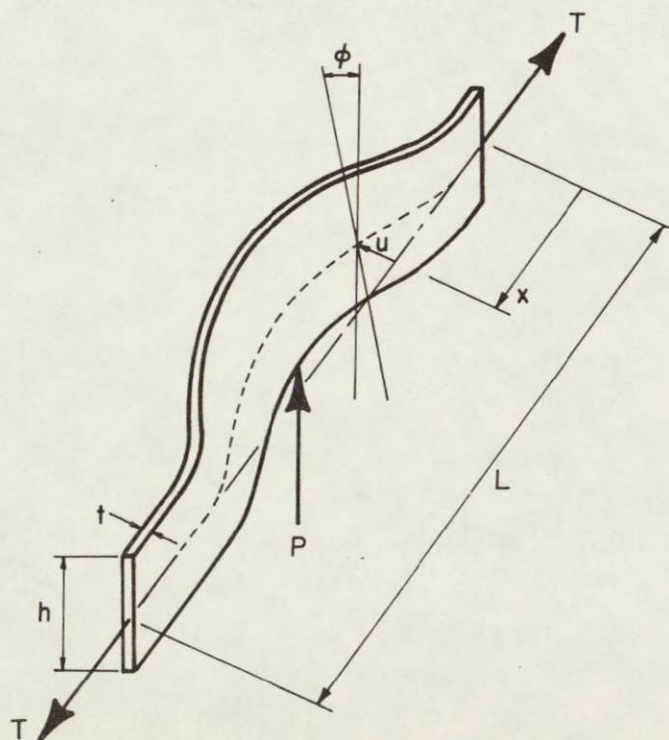


Figure 34. Model of a Thin Blade Undergoing Lateral Buckling Instability

where the primes denote derivatives with respect to x . Boundary conditions on Eqs. (1) and (2) are:

$$x = 0: u = u' = \phi = 0 \quad (25)$$

$$x = L/2: u' = \phi' = 0 \quad (26)$$

In the above equations, u is the blade centerline deflection, ϕ is the blade twist, E is the elastic modulus = 190 GPa, I is the moment of inertia in the most flexible direction = $ht^3/12$, M is the built-in end moment which is unknown *a priori* and is determined from the boundary conditions, and C is the torsional rigidity of the blade derived below.

a. TORSIONAL RIGIDITY

The torsional rigidity of a thin rectangular blade with no axial tension applied is given by:

$$R = Ght^3/3 \quad (27)$$

which holds for $h/t > 15$. When a blade is tensioned, the stress, σ , in the blade increases the torsional rigidity.

Consider the rectangular beam of Figure 34 and assume it has an applied torsional moment, M_t , twisting it rather than the load P . A counter moment to M_t is produced by the blade tension and this moment is given by:

$$M = \int_{-h/2}^{h/2} \sigma t y u_1' dy \quad (28)$$

where

$$\sigma = T/th \quad (29)$$

and

$$u_1 = u + y\phi \quad (30)$$

The quantity u_1 in Eq. (30) is the side displacement of the beam at any vertical position y . Thus, from Eq. (30):

$$u_1' = u' + y\phi' \quad (31)$$

By inserting Eq. (31) into Eq. (28) and carrying out the integration:

$$M = \sigma (th^3/12) \phi' \quad (32)$$

The moment given by Eq. (32) is a restoring moment counteracting the applied moment. By summing the torques acting on the beam

$$M_t - M = R\phi'$$

or, using Eq. (32)

$$M_t = (R + \sigma th^3/12) \phi' = C\phi' \quad (33)$$

and C is, therefore, given by

$$C = Ght^3/3 + \sigma th^3/12 \quad (34)$$

and represents the torsional rigidity of a rectangular beam subjected to an axial stress loading. This value of C is that used in Eq. (24) in which G is the shear modulus:

$$G = E/[2(1 + \nu)] \quad (35)$$

and ν is Poisson's ratio (0.3). For the hardened steel blades employed in the multiblade saw, $G = 73.1$ GPa.

b. BUCKLING LOAD

The general solution to Eqs. (23-26) has not been obtained. However, special cases can be found in the literature. For instance, for a simply-supported beam with no axial tension, ref. 6 gives the critical load:

$$M = T = 0: \quad P_{cr} = \frac{16.94 \sqrt{EIR}}{L^2} \quad (36)$$

Also, the critical load for the case where there is no axial tension but the blade ends are clamped is:⁶

$$T = 0: \quad P_{cr} = \frac{26.6 \sqrt{EIR}}{L^2} \quad (37)$$

Equations (36) and (37) give absurdly low values for P_{cr} since they neglect the axial tension which increases the critical load by orders of magnitude.

An approximate solution to Eqs. (23-26) which yields the critical load can be found using the method of Vianello.⁷ In that method, a shape for the midbeam deflection u is assumed, which satisfies the boundary conditions. Equation (24) is then used to obtain an approximate solution for ϕ and then these approximate solutions for u and ϕ are inserted into Eq. (23) to solve for a new u , subject to the boundary conditions of Eqs. (25) and (26). The initial assumed u was:

$$u = u_o \left(x^2 - \frac{4}{3} \frac{x^3}{L} \right) \quad (38)$$

where u_o is the arbitrary deflection at midspan. Equation (38), when inserted into Eq. (24) and solved for ϕ , gives:

$$\phi = \frac{P u_o L^3}{24C} \left[\frac{x}{L} + 4 \left(\frac{x}{L} \right)^3 - 8 \left(\frac{x}{L} \right)^4 \right] \quad (39)$$

Equations (38) and (39) are now used in Eq. (23) and a new solution of u is found. The coefficients of like powers of x are set equal between this new u and the trial u from Eq. (38) and the minimum value of P can then be determined which forces coefficient equality. Details are omitted and the result of these rather tedious computations is:

$$P_{cr} = \frac{4.67 \sqrt{48 EIC + TL^2 C}}{L^2} \quad (40)$$

The exact solution when $T = 0$ is given by Eq. (37). By putting $T = 0$ in Eq. (40) and comparing the constant in Eq. (40) with the exact value (26.6), it appears that Eq. (40) is about 20% high. Consequently, P_{cr} given by Eq. (40) was adjusted to agree with the exact solution for $T = 0$ and the final result is:

$$P_{cr} = \frac{3.84 \sqrt{48 EIC + TL^2 C}}{L^2} \quad (41)$$

which can be written as

$$P_{cr} = (1.11 h^2 t/L) \sqrt{[4 G (t/h)^2 + \sigma] [4E (t/L)^2 + \sigma]} \quad (42)$$

Where, as before, $\sigma = T/ht$, $G = 73.1$ GPa, and $E = 190$ GPa. Equation (42) is shown plotted in Figure 35 for some typical blade sizes.

Figure 35 shows that lateral buckling is not a problem when the blades are tensioned to the normal $\sigma = 1.35$ GPa stress level. In fact, the critical blade load is at least ten times the normal blade load of 2.0 N. The best results that have been obtained experimentally were with 0.2 X 6.4-mm blades (curve D). Figure 35 indicates that these blades should be more susceptible to buckling than the 0.1 X 12.7-mm blades which have failed on every occasion. Inspection of several of the 0.15 mm-thick diamond blades from Exp. 29 indicated that buckling *had* occurred and could be responsible for the slice breakage observed. Figure 36 shows one of these blades. Note how it is curved into the shape depicted in Figure 34. The grayish area in the center of the blade was caused by rubbing against the adjacent slice which is indicative of lateral buckling.

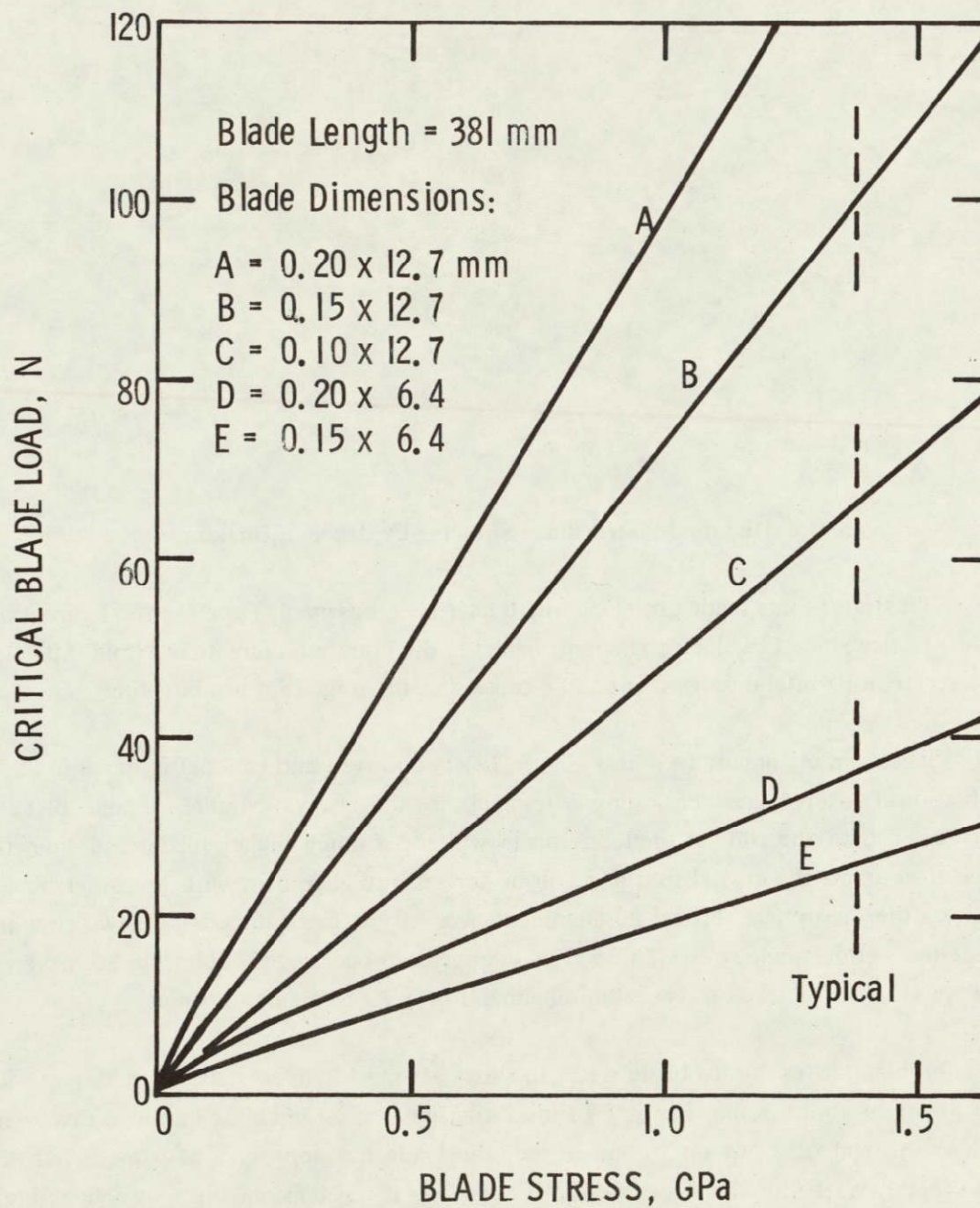


Figure 35. Theoretical Maximum Loads for Multiblade Saw Blades

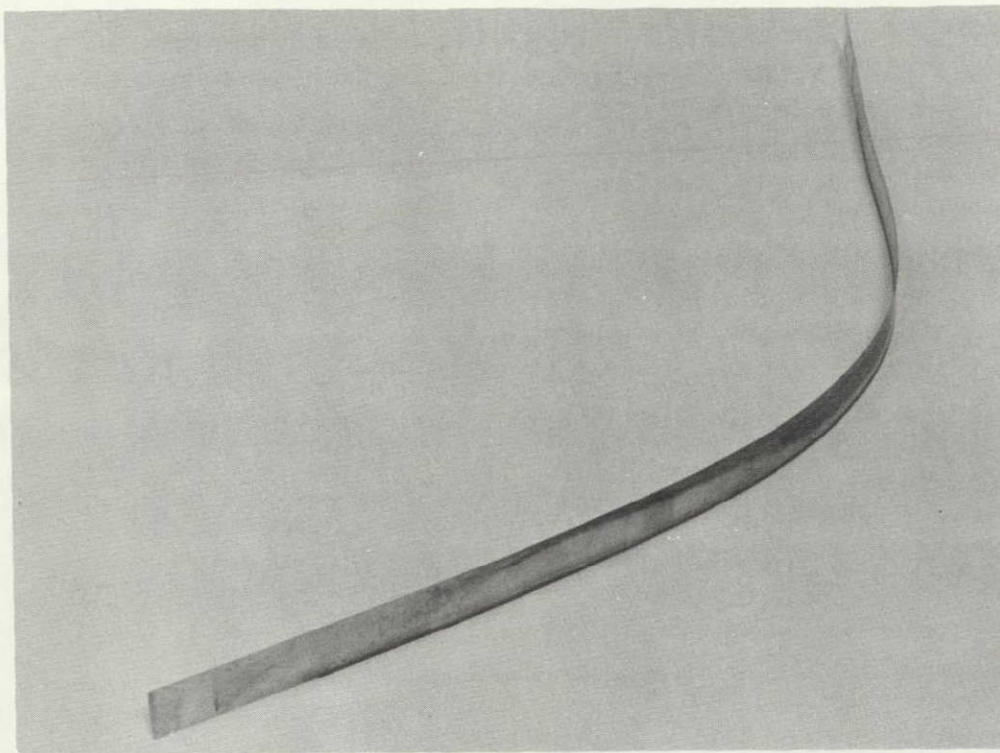
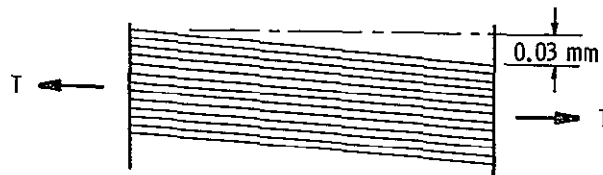


Figure 36. Diamond-Plated Blade Showing Evidence of Buckling

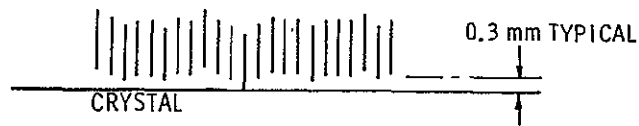
Figure 37 illustrates some blade problems which have been observed. Type I in the figure is not a problem in practice since the blade packs are aligned in the horizontal direction within 0.03 mm. Obviously, a severe horizontal misalignment could cause slice breakage (but not buckling).

Type II vertical misalignment (see also Figure 32) is observed and can cause buckling under extreme situations. After blade tensioning, the pack is not always parallel. If one blade is significantly lower than the others, then this blade will see a much higher blade load than the average since it contacts the crystal first and will be forced into alignment with the other blades. Figure 38 shows the theoretical vertical misalignment necessary to cause buckling for two common blade sizes. If the normal blade stress of 1.35 GPa is applied, no buckling should occur according to Figure 38. Type III is a variation on vertical misalignment peculiar to diamond blades.

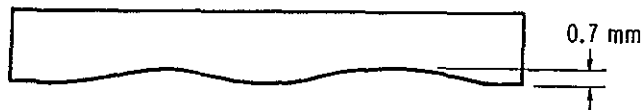
Another problem arises due to blade wear. In slurry sawing 12-cm crystals, the 6.35-mm wide blades wear down to about 3 mm. Figure 39 shows how the critical buckling load decreases with blade wear. At the end of a cut on 12-cm crystal, the blade has approximately one-fourth the critical load capacity as it did when new. Again, if the blade is not tensioned properly, buckling is much more probable at the end of the cut than at the beginning. This suggests that blade loading should be reduced toward the end of a cut to minimize the buckling probability.



I. BLADE PACK MISALIGNMENT



II. VERTICAL BLADE MISALIGNMENT



III. HORIZONTAL BLADE WAVINESS
(DIAMOND BLADES)

Figure 37. Blade Problem Catalog

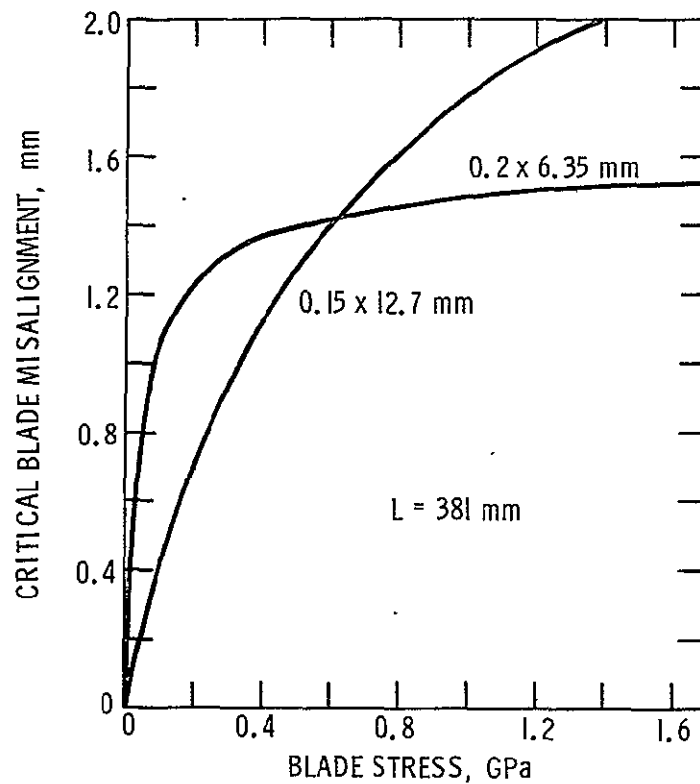


Figure 38. Blade Misalignment Sufficient to Cause Buckling

ORIGINAL PAGE IS
OF POOR QUALITY

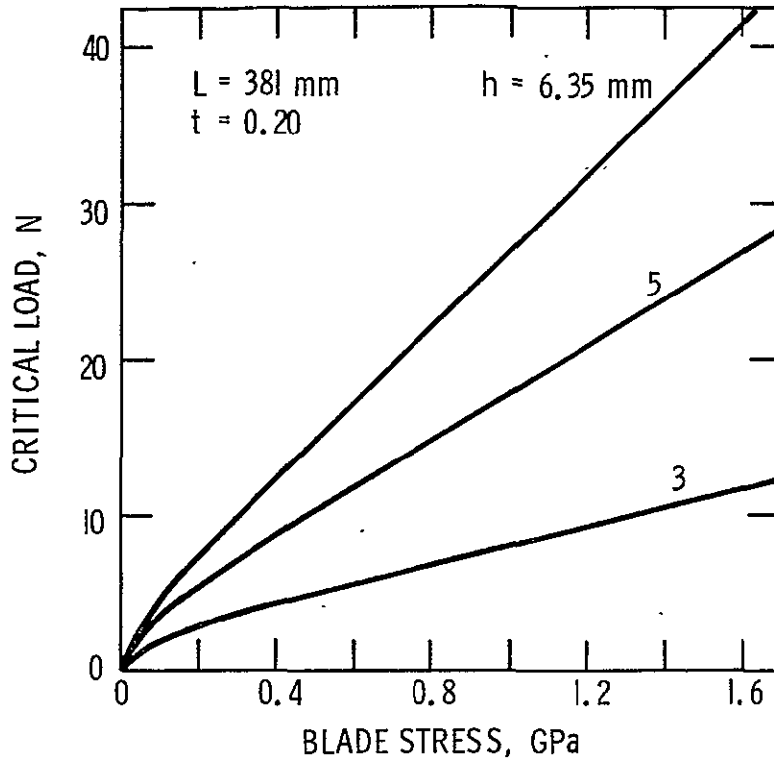


Figure 39. Effect of Blade Wear on the Critical Buckling Load

In summary, tensioning the blades to the proper level is extremely important if blade buckling is to be avoided. At present, there is no foolproof way to ensure each blade in a pack is properly tensioned.

c. BLADE VIBRATION

The natural vibration frequency of a taut blade is given by⁸

$$f^2 = (\sigma/\rho)/4L^2 \quad (43)$$

where σ is the blade stress and ρ is the blade density (7820 kg/m^3). Equation (43) must be multiplied by the gravitational constant to get the proper units for frequency in Hz. For the usual conditions employed on the saw, $f = 500 \text{ Hz}$, which is about an order of magnitude higher than the frequency of blade head oscillation. Consequently, the blade head oscillation should not excite blade vibration, which could then be transmitted to the slices with possibly damaging results.

4. Sawing Summary

Slice thicknesses of 0.25 mm can be obtained using 400-grit SiC abrasive in a nominal 500 g/l PC oil slurry with 0.36-mm spacers between blades. For reliable sawing of 12-cm crystal, a 0.2-mm thick by 6.35-mm high blade is recommended. This blade/spacer combination results in a slice plus kerf of 0.56 mm which appears to be a practical lower limit and still achieve fairly good cutting rates.

For multiblade sawing to be cost effective, cutting rates of at least 5 mm/h must be achieved. Figure 40 summarizes experimentally determined cutting rates from key experiments performed on this program. A 5 mm/h sawing rate is achievable with SiC abrasive as indicated. Boron carbide abrasive has demonstrated a 2.5 times improvement in cutting rates over SiC but the much greater cost of B_4C does not make its use cost effective. The data in Figure 40 were obtained with blade reciprocation rates in the 50-60 cycles/min range and some improvement in cutting speed could be obtained at higher reciprocation rates. However, there is some concern that at rates higher than 70 cycles/min, excessive slice breakage might be encountered on thin slices.

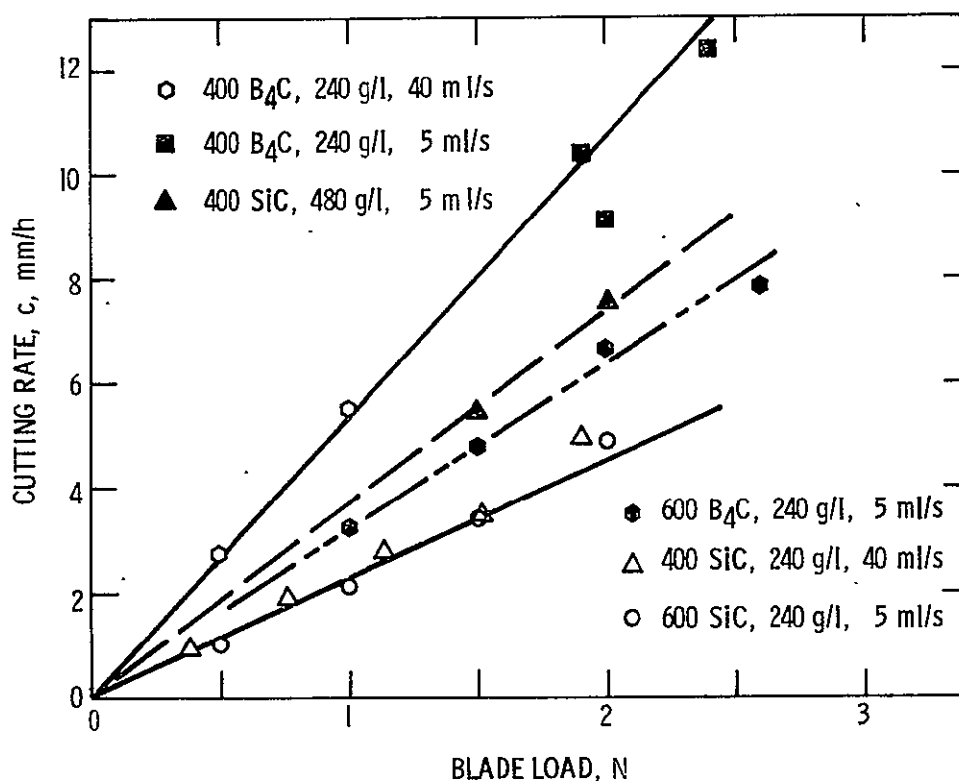


Figure 40. Effects of Multiblade Saw Slurry Parameters on Silicon Cutting Rates

Results of stationary sawing with diamond blades are not included in Figure 40. Table 25 lists the maximum stationary cutting rates of diamond blades. The data in Table 25 do not follow an orderly trend as do those in Figure 40. At best, diamond blades used in this study appear no better than B₄C abrasive. A wide range of diamond-plating parameters is available and it is believed that a better diamond formulation for multiblade sawing can be found. Data from Exps. 28 and 33 indicate larger diamond particles is not the way to go.

Table 25. Diamond-Plated Blade Cutting Rates

Blade Load N	Cutting Rate mm/h
0.9	4.1
1.5	5.2
2.1	6.9
2.4	6.0

Figure 41 compares the stationary cutting data of Figure 36 to results obtained with crystal spinning. The diamond blades are clearly superior in the spinning mode to any slurry tested. It appears, then, that the diamond blades perform better with a high relative blade speed.

In summary, the experimental work on crystal slicing has indicated:

- 1) Saw rate is directly proportional to blade load.
- 2) For a given blade load, the sawing rate is proportional to blade speed.
- 3) Saw rate is independent of kerf length, i.e., multiple crystals can be sliced at the same rate as a single crystal.
- 4) As blade load increases, parameter control (bow, taper, etc.) appears to decrease.
- 5) SEMs of the new and used silicon carbide and boron carbide indicate some particle wear and fragmentation.
- 6) Efforts to saw thin slices by utilizing thin blade spacing (0.31 mm) have resulted in excessive slice breakage.
- 7) Multiblade slurry saw yields with thicker slices are in excess of 95%.

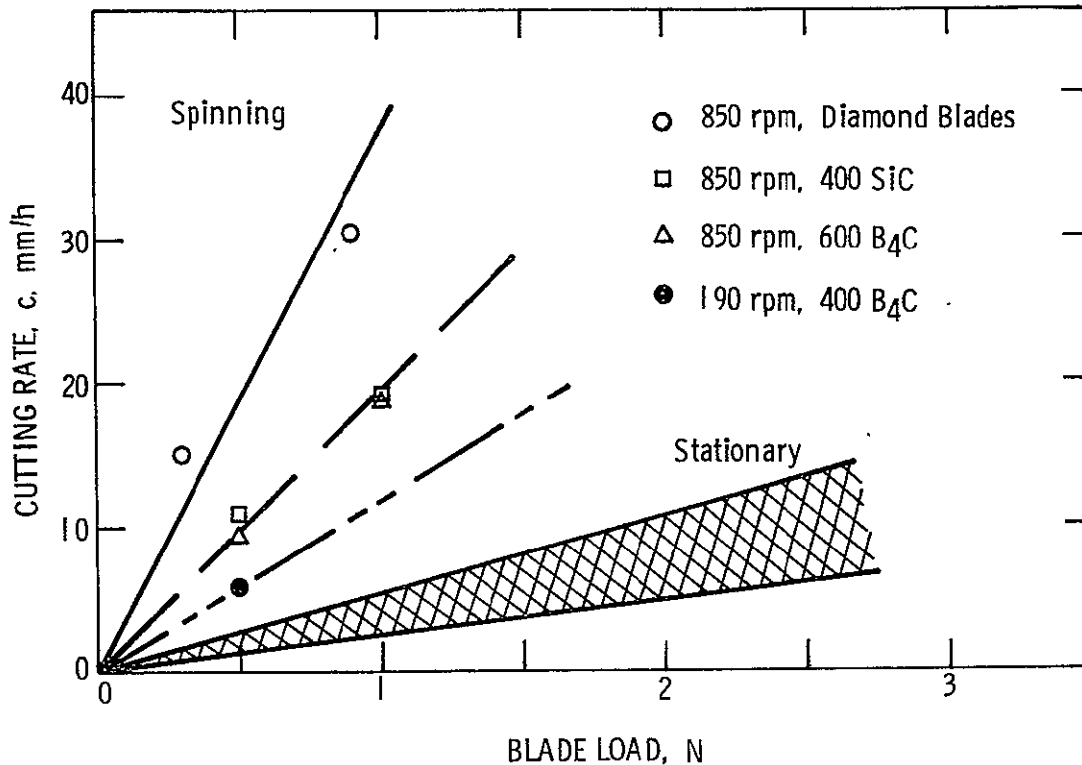


Figure 41. Multiblade Saw Silicon Cutting Rates

- 8) The larger and harder the abrasive particle, the faster the cutting rate. A 400-grit B₄C will produce a silicon cutting rate 2.5 times that of 600-grit SiC. Higher abrasive concentrations in the slurry result in faster sawing rates. It is preferable from a cutting rate standpoint to run dry rather than flood the workpiece with slurry. The optimal slurry flow for normal abrasive concentrations is around 5 ml/s which is considerably lower than the wide open flow of 40 ml/s.
- 9) Narrow, thick blades are preferable to thin, wide blades. Best results have been obtained with 0.2 X 6.4 mm blades tensioned 0.7%. Very thin blades (0.1 mm) are unstable in the lateral direction at higher blade loads which results in broken slices and blade wander.
- 10) To minimize the probability of slice breakage due to blade buckling, it is essential to tension the blades to the normal 0.7% elongation. The 0.2 X 6.4 mm blades are less susceptible to buckling due to vertical misalignment coupled with reduced tension.

ORIGINAL PAGE IS
OF POOR QUALITY

C. CHARACTERIZATION

1. Crystal

Resistivity, carbon and oxygen content, and lifetime were measured on selected crystals. A 4-point probe was used to measure resistivity on slices taken from the top and bottom of the crystal. Radial gradients were determined from ten readings across the slice out to within R/8 of the edge.

Oxygen and carbon concentrations were determined using a Perkin-Elmer 283 Spectrophotometer. This infrared technique employs a difference measurement between the sample and a float zone reference containing less than 5×10^{15} atoms/cm³ carbon and oxygen. The accuracy of this technique is believed within 5% for oxygen and 10% for carbon. ASTM procedures F121-70T and F123-74 were followed.

Minority carrier lifetimes were measured by the surface photovoltage (SPV) technique. The SPV technique involves the illumination of the specimen surface (in this case, nominal 0.4-mm wafers chemically polished on both sides) with a chopped monochromatic radiation with energy slightly greater than the band gap of silicon. Electron-hole pairs are produced and diffuse to the surface where they are separated by the electric field of a depletion region to produce a surface photovoltage. The SPV measurement procedure followed closely the ASTM F391-73T recommendations.

Table 26 presents pertinent data on several of the 12-cm crystals grown on this contract. All the doped crystals were p-type (boron), and none were heat treated. Generally, carbon and oxygen levels are normal for Cz silicon grown from RH furnaces. The letters T and B on the crystal numbers refer to top and bottom respectively.

Table 27 lists radial resistivity gradients for two crystals. The gradients are surprisingly flat and compare quite favorably to those observed on 7.6-cm ingots.

2. Slice Thickness, Bow, and Taper

These parameters were all measured with an ADE Corporation Microsense 3046A unit and measurements are presented in the tables summarizing sawing experiments. Slice thickness was measured at the wafer center. Bow was determined by supporting the wafer at the periphery and taking the center reading. Taper was defined as the difference between the maximum and minimum thicknesses measured at three peripheral locations and the center.

Table 26. 12-cm Crystal Characterization

Crystal	Resistivity	Oxygen	Carbon	Lifetime
*12-4 T	53 Ω -cm	1.5 E18/cm ³	2.7 E17/cm ³	50 μ s
12-10 T	—	1.6 E18	6.0 E16	—
12-12 T	1.5	1.7 E18	3.9 E16	84
12-14 T	1.7	1.5 E18	1.2 E16	42
12-21 T	1.7	1.8 E18	2.7 E16	20
12-21 B	1.5	1.5 E18	7.0 E16	30
12-24 T	1.2	1.9 E18	1.5 E17	16
12-24 B	1.1	1.4 E18	5.9 E17	4
12-26 T	1.1	1.9 E18	9.5 E16	11
12-26 B	0.8	1.3 E18	2.4 E17	11
12-32A T	1.1	1.5 E18	1.8 E16	20
12-32A B	0.7	1.1 E18	1.6 E17	—
12-32B T	2.0	1.7 E18	4.2 E17	—
12-32B B	1.7	1.4 E18	6.6 E17	—
12-32C T	—	1.6 E18	5.2 E17	—
12-32C B	—	1.4 E18	5.4 E17	—

*Undoped

Table 27. 12-cm Radial Resistivity Gradients

Crystal	Gradient	
	R/2	R/8
12-24 T	2.4%	1.0%
12-24 B	10.8	12.4
12-26 T	6.4	9.6
12-26 B	0.5	0.1

The general trend of the data showed that as blade loading increased, thickness uniformity, bow, and taper worsened but are still adequate for solar cell requirements. On the other hand, surface planarity is relatively unaffected by blade load as indicated in Figures 42 and 43 for loads up to 2.4 N/blade.

3. Saw Damage Depth

Damage depth was determined using X-ray topography. The slice is masked on one side and 0.05 mm etched (planar) off the unmasked side to remove some saw damage. The etched side is then masked and approximately one-fourth of the original masked sawed surface is exposed. The slice is placed in planar etch to remove approximately 0.06 mm. Another one-fourth of the mask is removed and that surface etched approximately 0.06 mm. This procedure is repeated two more times and produces a slice as shown in Figure 44 with four etched regions. Examination under a metallurgical microscope at 448X is not adequate to reveal damage sites.

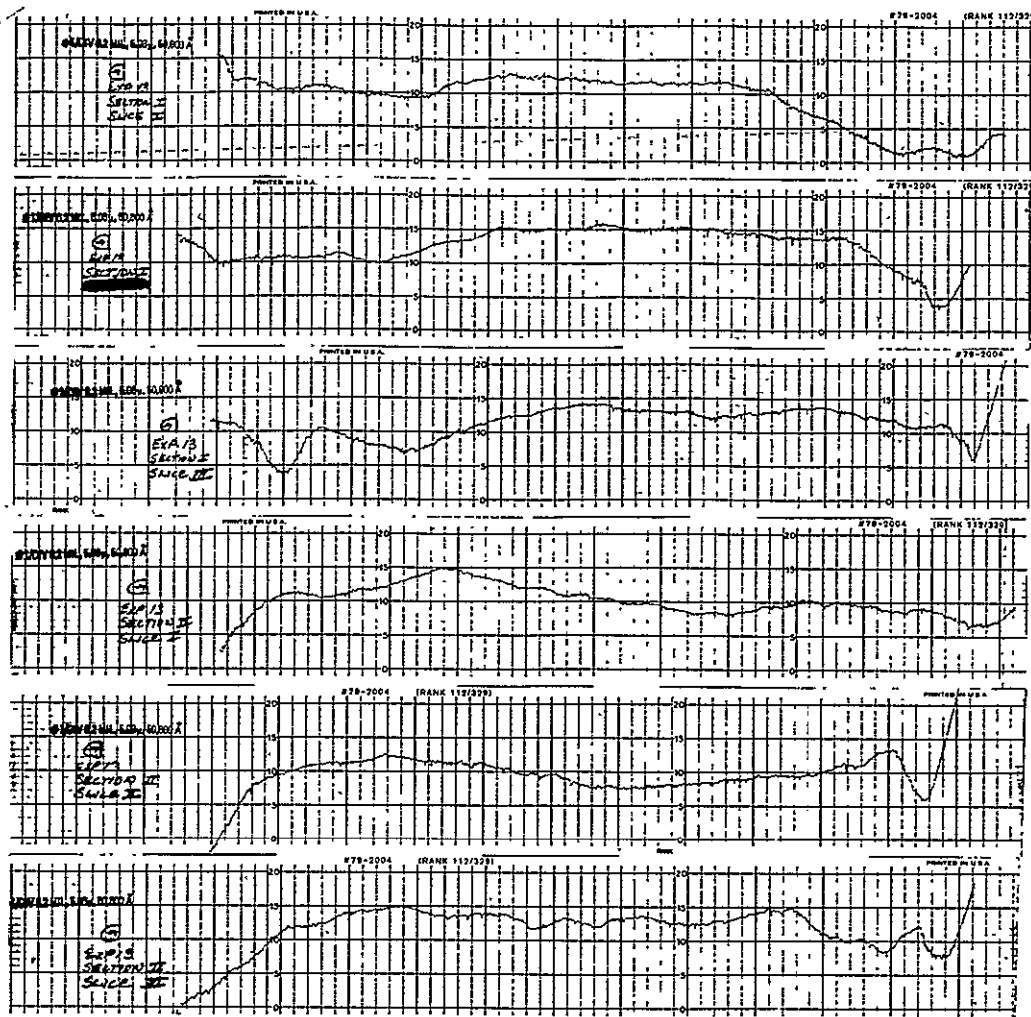


Figure 42. Talysurfs from Experiment 13 – 400-Grit B₄C Abrasive, 2.4 N/Blade Load

The slice is now ready for Automated Transmission X-ray Topography. In addition to the standard transmission X-ray topograph as shown in Figure 45, a printout is obtained as in Figure 46. The first column of data is the slice position indexed to the slice flat. The second column is the Bragg angle which should be approximately constant if the slice is flat. The third column is the X-ray intensity reading. As the X-ray enters the damaged region (region 1), note the increase in intensity, which indicates residual saw damage.

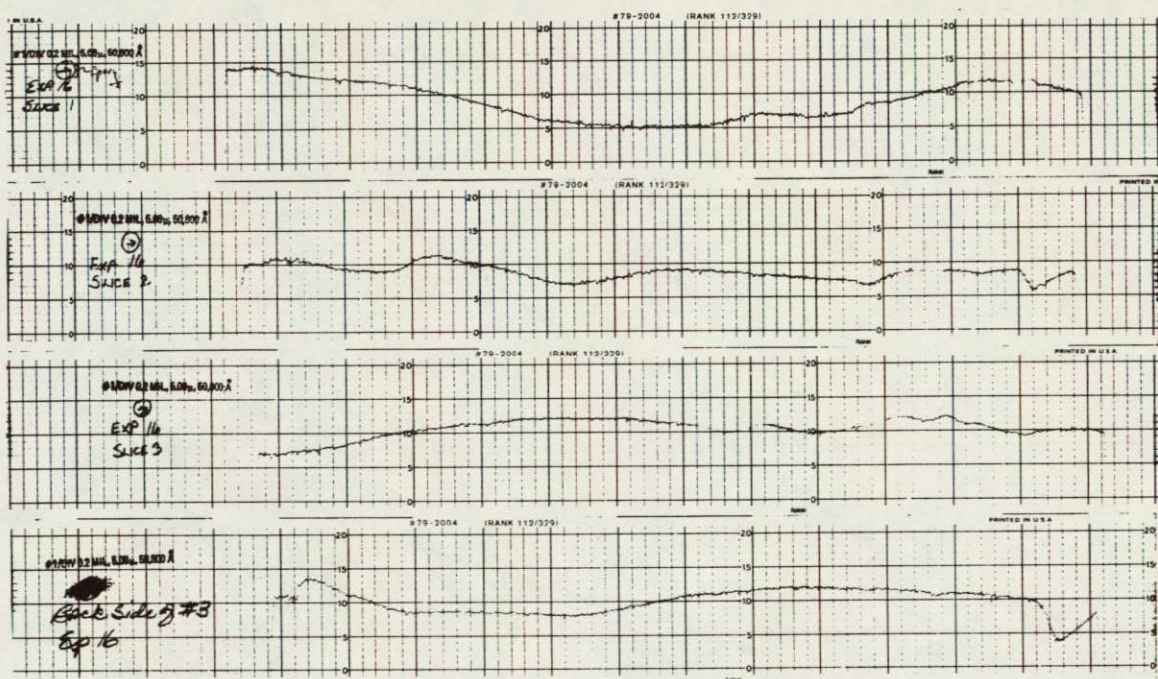


Figure 43. Talysurfs from Experiment 16 – 400-Grit B₄C Abrasive, 2.0 N/Blade Load

The topography — region 1 — reveals damage sites after $7.6 \mu\text{m}$ are removed (dark regions). After $17.8 \mu\text{m}$ of silicon are removed, region 2 reveals only four sites remaining. Regions 3 and 4 are free of damage. The salt-and-pepper effect in Figure 45 is film graininess showing up at the magnification of 28X.

Measurements on various slices indicate severe slice damage is confined to a surface layer $10 \mu\text{m}$ in depth with medium to light damage in the next $10 \mu\text{m}$. Thus, the nature of damage induced by slurry sawing appears no different from that observed for lapping, grinding, or ID sawing operations. There is a thin surface region of microcracks caused by particle abrasion and these microcracks create dislocations which propagate some distance into the slice interior. This damage depth is a function of many factors such as abrasive hardness, particle size, and blade load. The nominal 20-30- μm depths measured in this work are comparable to silicon lapping damage⁹ and indicate that slurry sawing is a relatively gentle slicing process. Damage depths with ID sawing using diamond-plated blades are typically around $10 \mu\text{m}$.¹⁰ The variation of damage depth as a function of various slurry sawing parameters is shown below.

ORIGINAL PAGE IS
OF POOR QUALITY

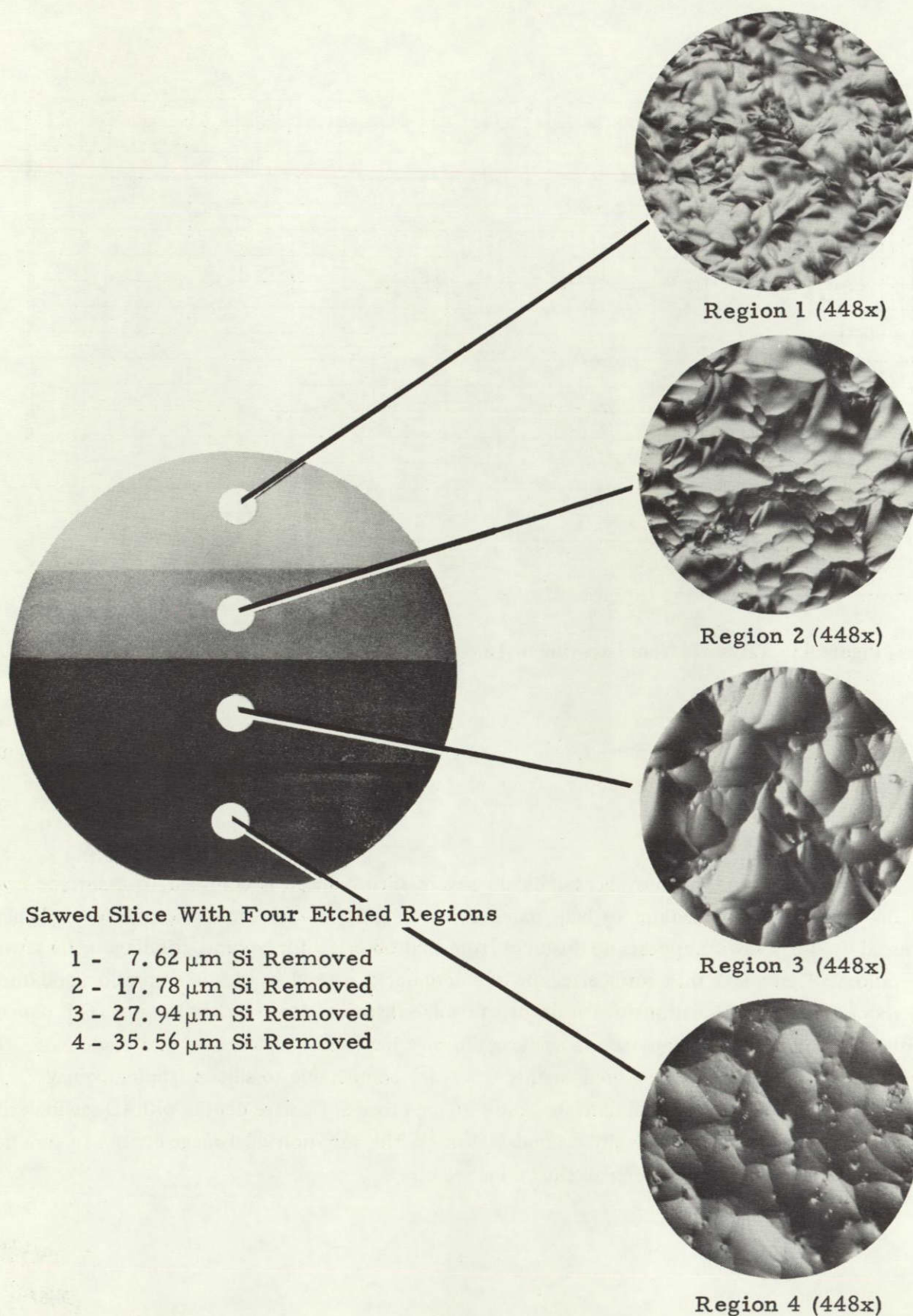


Figure 44. 7.6-cm Diameter Sawed Slice Prepared for Transmission X-ray Topography

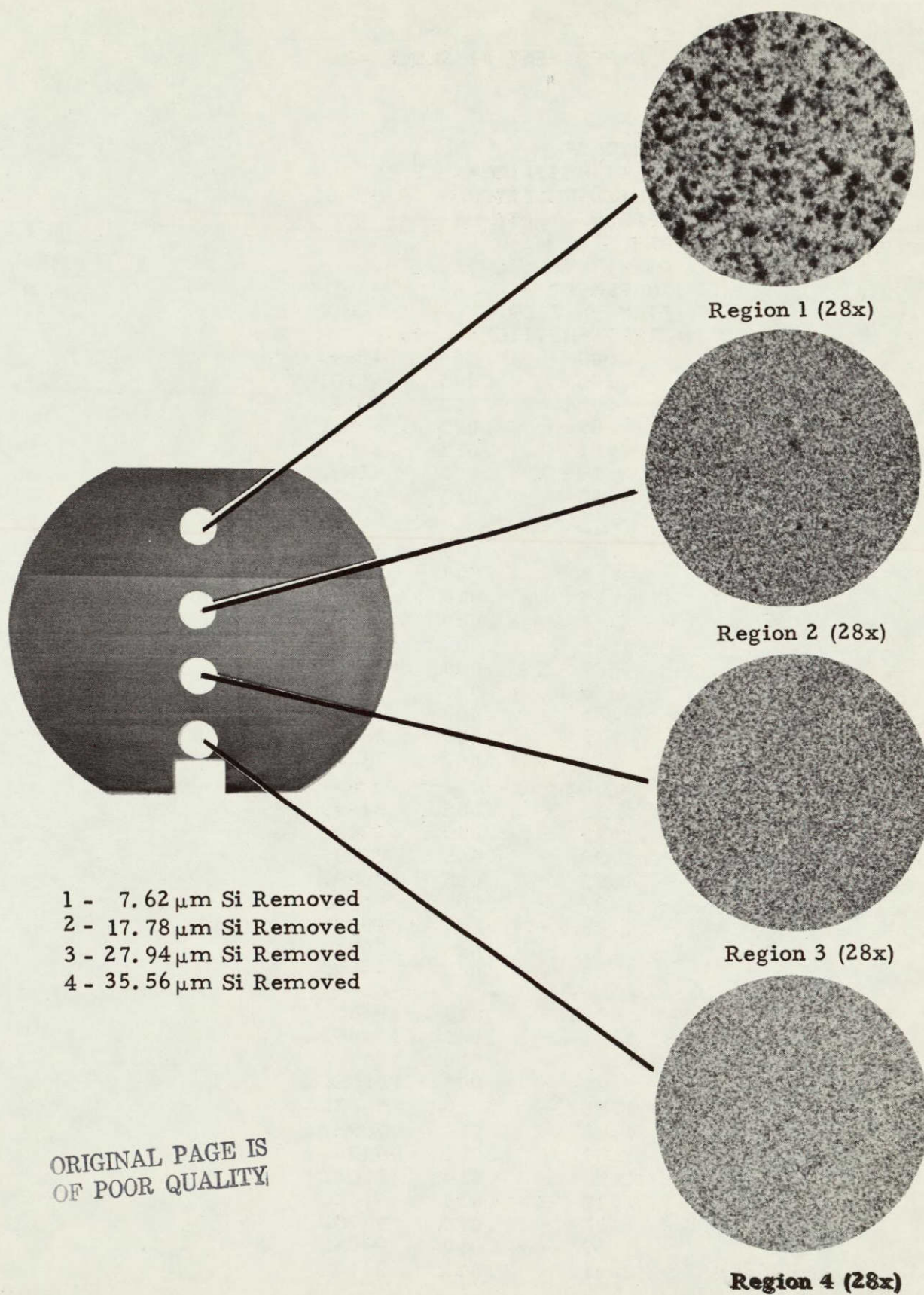


Figure 45. Transmission X-ray Topography of a Step-Etched Slice

```

EF
? EXPERIMENT #1 SLICE #2

S
? SC
OPTIONS? N
START POSITION= 2.25
FINISH POSITION=- 2.25
SPEED= .050
ABAC? Y
PRINT? Y
INCREMENT .02
FILM -HIT CR
START POSITION= 1.47
- .03 .000 4584.
- .05 .005 6018.
- .07 .010 6406.
- .09 .015 6292.
- .11 .015 6157.
- .13 .015 6254.
- .15 .015 6421.
- .61 .000 7817.
- .63 .000 7942.
- .65 .000 7898.
- .67 .000 7898.
- .69 .000 7975.
- .71 .000 7753.
- .73 .000 7719.
- .75 .000 7759.
- .77 .000 7811.
- .79 .000 7673.
- 1.29 - .005 7404.
- 1.31 - .005 7308.
- 1.33 - .005 7229.
- 1.35 - .005 7089.
- 1.37 - .005 7099.
- 1.39 - .005 6967.
- 1.41 - .005 7051.
- 1.43 - .005 6923.
- 1.79 - .015 9465.
- 1.81 - .015 10406.
- 1.83 - .010 10493.
- 1.85 - .005 10156.
- 1.87 - .010 9477.
- 1.89 - .010 9392.
- 1.91 - .010 9430.
- 1.93 - .010 9120.
- 1.95 - .010 9166.
- 1.97 - .010 9495.
- 1.99 - .010 9494.
- 2.01 - .010 9310.

```

Figure 46. Computer Printout of the Transmission X-ray Topograph

Slice Damage Depth

Heavy	0.0-10.0 μm
Medium to light	10.0-23.0 μm
Light to none	23.0-33.0 μm

Abrasive Hardness

SiC (400 grit)	23 μm typical
B ₄ C (400 grit)	33 μm typical

Abrasive Particle Size

400 grit B ₄ C	33 μm
600 grit B ₄ C	25 μm

Blade Load

Maximum slice damage depth of 33 μm at 2.5 N/blade

The data indicate that if the solar cell process requires a damage-free surface, then a minimum of 33 μm must be removed by etching or texturing.

4. Cell Fabrication

Solar cells were fabricated by TI Array Automation (Task 4) personnel on slices from sawing Exp. 2. These slices were sawed with 400-grit SiC abrasive at blade loads up to 1.9 N. Slice thickness averaged 0.6 mm. The slices were given a light, 25 μm , planar etch prior to normal solar cell processing. A control lot consisting of four slices cut with an ID saw was run simultaneously with three lots of multiblade-sawed slices. Average I_{SC} was 0.95 A and V_{OC} was 0.54 V for the slurry-sawed slices compared to 0.94 A and 0.55 V measured on the control slices. These results indicate no significant difference in cell performance between ID and multiblade-sawed slices.

D. WAFER SHAPING

1. Laser Scribing

Several 7.6- and 12-cm diameter slices of varying thicknesses were sent to Electro Scientific Industries in Portland, Oregon for laser scribe experiments. ESI used their Model 32 laser system in attempting to completely cut and shape the slices into hexagonals. This system utilizes a 10-W YAG laser.

ORIGINAL PAGE IS
OF POOR QUALITY

Two operational modes were evaluated: (1) pulse mode, Figure 47(a), which produces a donut-shaped beam, and (2) continuous mode, Figure 47(b), which produces a pointed beam about 25 μm in diameter. The continuous mode produces a narrower cut line and much less silicon slag at the cut edge. At 10-cm/s shaping speed, the total penetration on the various slices was 0.15 to 0.20 mm. Focus of the beam either at the surface or 0.13 mm below the surface had little effect on penetration but the lower focus did produce a channel with less slag. The system was fitted with vacuum and air jets to remove particles of silicon as the beam cut. The resulting slice surface was very free of particles and the edge of the cut had minimum buildup as shown in Figure 48. By reducing the scribe speed to 5.1 cm/s on a 0.25-mm thick slice, an average cut depth of 0.23 mm was obtained with total penetration in spots. Figure 49 is a view of the laser cut for this case.

The last group of 12-cm slices sent to ESI averaged 0.24 mm in thickness. Shaping rates of 1 cm/s, 5 cm/s and 10 cm/s were evaluated. Figure 50 indicates that at 1 cm/s complete cut through is obtained. Figure 51 indicates that at 5 cm/s some areas are completely cut through with small areas (light spots) of single crystal that cleaved. Figure 52 indicates at 10 cm/s approximately half the slice is cut. Application of a slight pressure introduces breakage at the laser cut.

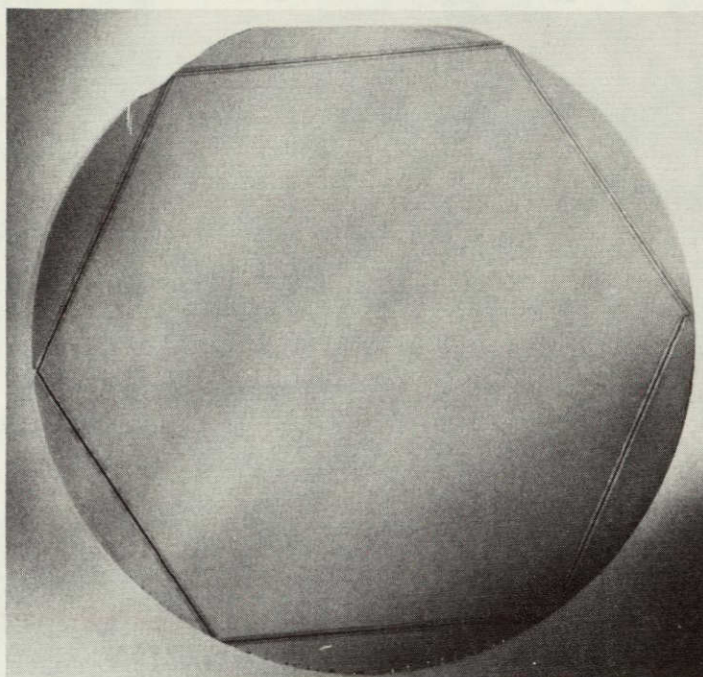
If edge grinding is necessary for the solar cell blanks, then there is a question as to the necessity of total scribe through. It is straightforward to achieve a 0.05 to 0.10 mm cut depth and then break the edges. At these shallower cuts, scribe rates up to 30 cm/s are feasible.

2. Edge Beveling

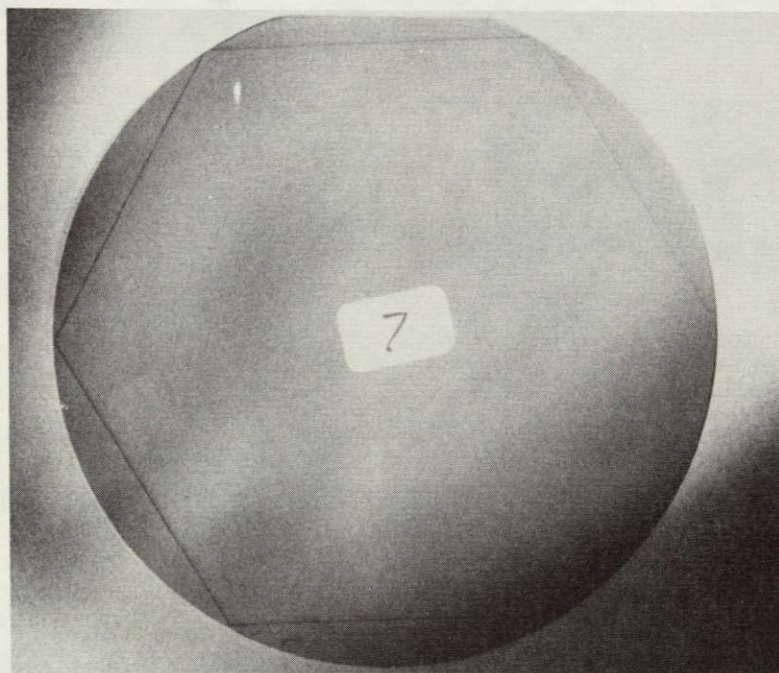
A Macronetics G1000 edge shaper was evaluated on 7.6-cm slices. However, this machine would not accommodate a hexagonal shape. Macronetics was given six 12-cm hexagonal slices for trials on a new, larger shaper but this shaper was not large enough to properly bevel the 12-cm slices. An even larger shaper is being developed but was not available in time for evaluation on this program. In any event, economic analysis of the edge bevel operation indicates it is far too expensive for solar cell — Cz silicon.

E. ECONOMIC MODELING

The Czochralski sheet process consists of two primary processes: crystal growth and crystal slicing. There are secondary process steps such as crystal crop, crystal grind (if necessary), wafer cleanup, and wafer shaping. Costs associated with these secondary processes can be lumped with the basic crystal growth or wafering step but these various costs will be considered separately in this report.



(a) ESI MODEL 32 IN PULSE MODE



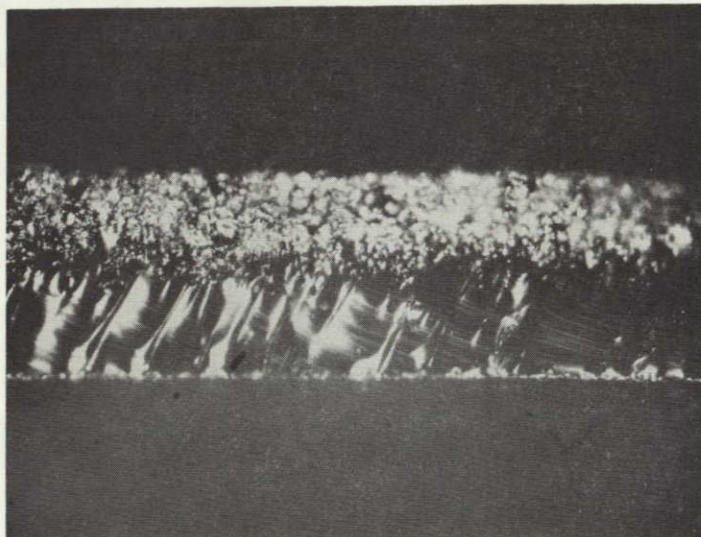
(b) ESI MODEL 32 IN CONTINUOUS MODE

Figure 47. Laser Scribed Slices

ORIGINAL PAGE IS
OF POOR QUALITY



(a) TOP VIEW OF SLICE LASER SCRIBED AT 10 cm/s (55x)



(b) CROSS-SECTIONAL VIEW OF SLICE
LASER SCRIBED AT 10 cm/s (110x)

Figure 48. Photomicrographs of Laser Scribed Silicon Slices — Continuous Mode

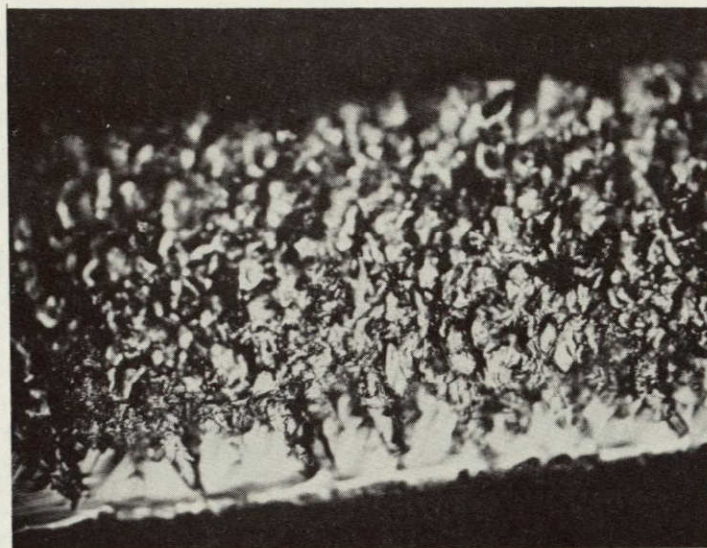


Figure 49. Cross Section of Line Laser Scribed at 5.1 cm/s (300X)

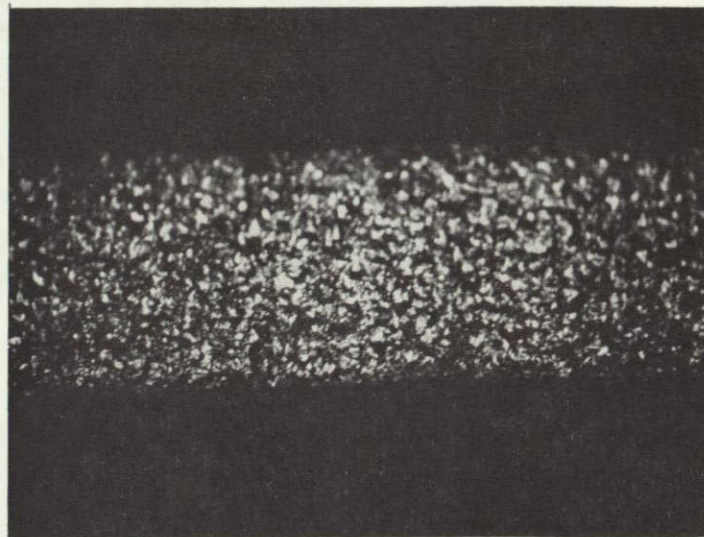
The fundamental economic model assumes 12-cm diameter crystal grown from an 18-kg crucible with subsequent wafering performed on a multiblade slurry saw capable of slicing 28-cm crystal lengths. Single-charge, multicharge, and semicontinuous crystal growth are all examined. Semicontinuous growth consists of feeding polysilicon into the crucible as a crystal is grown in order to maintain constant melt level and allow crystal lengths independent of crucible capacity. Periodically the process is interrupted to permit removal of the crystal after it attains a predetermined length. Crystal lengths are assumed to be multiples of the 28-cm sawing length.

A crystal pull rate of 9 cm/h is used for single and multicharge runs. In semicontinuous runs, 12 cm/h is used for all but the last crystal and 9 cm/h is applied for that crystal. These pull rates are lower than the pull rate modeling indicates is possible but the experimental crystal growth work supports the assumed values.

ORIGINAL PAGE IS
OF POOR QUALITY

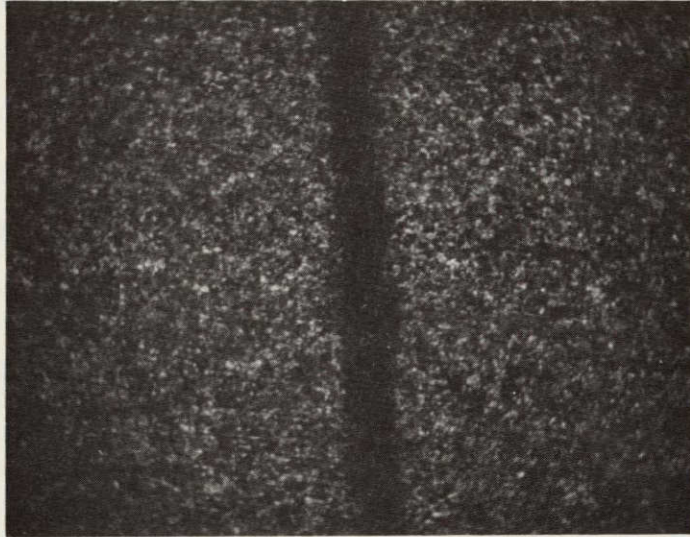


(a)

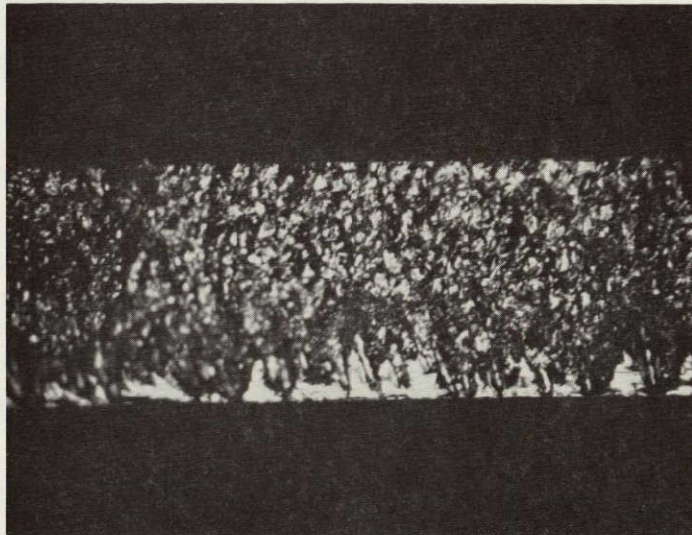


(b)

Figure 50. Laser Shaping Rate of 1 cm/s (110X)



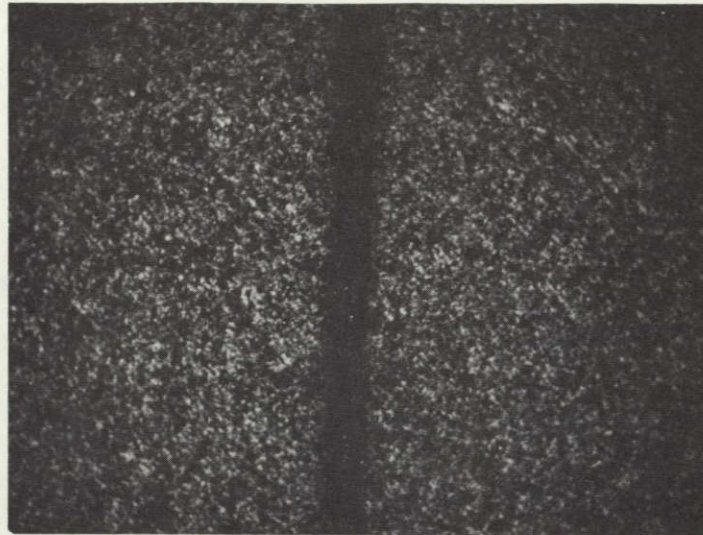
(a)



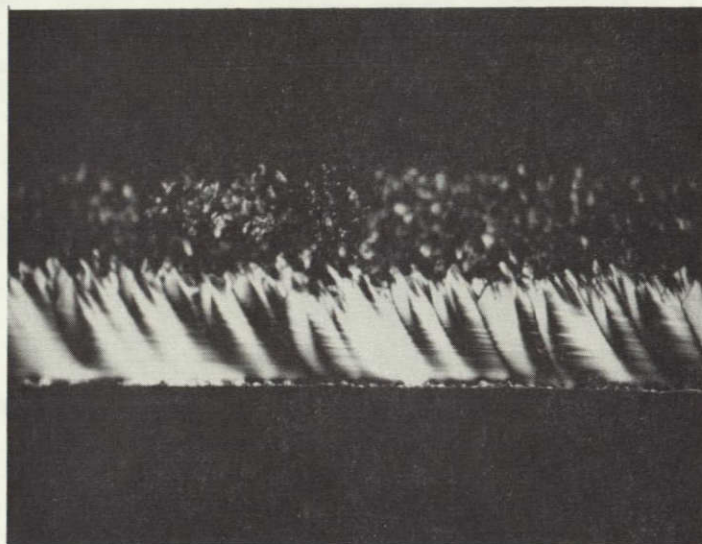
(b)

Figure 51. Laser Shaping Rate of 5 cm/s (110X)

ORIGINAL PAGE IS
OF POOR QUALITY



(a)



(b)

Figure 52. Laser Shaping Rate at 10 cm/s (110X)

c. MULTICHARGE (Three Crystals)

Item	Time	Crystal Length
Cleanup	0.5 h	
Load and Melt (18 kg)	2.0	
Seed and Top	2.0	
Growth (14.82 kg)	6.2	56 cm
Taper (0.7 kg)	1.0	
Load and Melt (14.82 kg)	1.3	
Seed and Top	2.0	
Growth (14.82 kg)	6.2	56
Taper (0.7 kg)	1.0	
Load and Melt (14.54 kg)	1.3	
Seed and Top	2.0	
Growth (14.82 kg)	6.2	56
Taper (0.7 kg)	1.0	
Cooldown	2.0	
Totals	34.7 h	168 cm
Polysilicon Charged:	47.36 kg	
Power Consumed:	1557 kW-h	

d. SEMICONTINUOUS (Three Crystals)

Item	Time	Crystal Length
Cleanup	0.5 h	
Load and Melt (18 kg)	2.0	
Seed and Top	2.0	
Growth (22.23 kg)	7.0	84 cm
Taper (0.7 kg)	1.0	
Unload	1.0	
Seed and Top	1.0	
Growth (22.23 kg)	7.0	84
Taper (0.7 kg)	1.0	
Unload	1.0	
Seed and Top	1.0	
Growth (22.23 kg)	9.3	84
Taper (0.7 kg)	1.0	
Cooldown	2.0	
Totals	36.8 h	252 cm
Polysilicon Charged:	69.59 kg	
Power Consumed:	1658 kW-h	

ORIGINAL PAGE IS
OF POOR QUALITY

2. Crystal Growth Cost Assumptions

- 1) \$10/kg polysilicon
 - 2) Argon costs \$3/h of puller operation
 - 3) Electrical power is \$0.03/kW-h
 - 4) Miscellaneous materials costs as given in Appendix F
 - 5) Three pullers/operator
 - 6) Puller costs: \$100,000 for single charge; \$125,000 for multicharge; and \$200,000 for a semicontinuous puller
 - 7) Seven-year, straight line depreciation
 - 8) Labor at \$4.50/h
 - 9) Seven-day week, 52-week year
 - 10) An 83% equipment utilization
 - 11) Supervision cost at 10% direct labor
 - 12) Miscellaneous overhead at 100% direct labor.
-

3. Crystal Growth Costs

a. SINGLE CHARGE (12-kg Crucible)

Materials:	Polysilicon (11.6 kg)	\$116.00
	Seed	5.00
	Liner	100.00
	Argon	27.90
	Energy	12.18
	Miscellaneous	<u>54.00</u>
	Total Material	\$315.08/run
Labor:	Direct: (11.3 h) (\$4.50/h)/3	\$ 16.95
	Supervision:	<u>1.70</u>
	Total Labor	\$ 18.65/run
Overhead:	100% direct labor	\$ 16.95/run
Depreciation:	No. runs/yr/puller =	
	(24) (0.83) (7) (52)/11.3 = 644.2	
	Depreciation/run =	
	\$100,000/(7) (644.2) =	
		\$ 22.17/run
Total Crystal Cost:	100% yield	\$372.85/run
Crystal Cost:	100% yield (38 cm)	\$ 9.81/cm length
Add-on Crystal Cost:	100% yield (no polysilicon)	\$ 6.76/cm length

b. SINGLE CHARGE (18-kg Crucible)

Materials:	Polysilicon (16.32 kg)	\$163.20
	Seed	5.00
	Liner	125.00
	Argon	34.50
	Energy	15.36
	Miscellaneous	<u>54.00</u>
	Total Material	\$397.06/run
Labor:	Direct: (13.5 h) (\$4.50/h)/3	\$ 20.25
	Supervision:	<u>2.03</u>
	Total Labor	\$ 22.28/run
Overhead:	100% direct labor	\$ 20.25/run
Depreciation:	No. runs/yr/puller =	
	(24) (0.83) (7) (52)/13.5 = 539.3	
	Depreciation/run =	
	\$100,000/(7) (539.3) =	
		\$ 26.49/run
Total Crystal Cost:	100% yield	\$466.08/run
Crystal Cost:	100% yield (56 cm)	\$ 8.32/cm length
Add-on Crystal Cost:	100% yield (no polysilicon)	\$ 5.41/cm length

ORIGINAL PAGE IS
OF POOR QUALITY

c. MULTICHARGE (Three Crystals)

Materials:	Polysilicon (47.36 kg)	\$473.60
	Seeds (3)	15.00
	Liner	125.00
	Argon	98.10
	Energy	46.71
	Miscellaneous	<u>70.00</u>
	Total Material	\$828.41/run
Labor:	Direct: (34.7 h) (\$4.50/h)/3	\$ 52.05
	Supervision:	<u>5.21</u>
	Total Labor	\$ 57.26/run
Overhead:	100% direct labor	\$ 52.05/run
Depreciation:	No. runs/yr/puller =	
	(24) (0.83) (7) (52)/34.7 = 209.8	
	Depreciation/run =	
	\$125,000/(7) (209.8) =	
		\$ 85.12/run
Total Crystal Cost:	100% yield	\$1022.84/run
Crystal Cost:	100% yield (168 cm)	\$ 6.09/cm length
Add-on Crystal Cost:	100% yield (no polysilicon)	\$ 3.27/cm length

d. SEMICONTINUOUS (Three Crystals)

Materials:	Polysilicon (69.59 kg)	\$ 695.90
	Seeds (3)	15.00
	Liner	125.00
	Argon	104.40
	Energy	49.74
	Miscellaneous	<u>70.00</u>
	Total Material	\$1060.04/run
Labor:	Direct: (36.8 h) (\$4.50/h)/3	\$ 55.20
	Supervision:	<u>5.52</u>
	Total Labor	\$ 60.72/run
Overhead:	100% direct labor	\$ 55.20/run
Depreciation:	No. runs/yr/puller =	
	(24) (0.83) (7) (52)/36.8 = 197.8	
	Depreciation/run =	
	\$200,000/(7) (197.8) =	
		\$ 144.43/run
Total Crystal Cost:	100% yield	\$1320.39/run
Crystal Cost:	100% yield (252 cm)	\$ 5.24/cm length
Add-on Crystal Cost:	100% yield (no polysilicon)	\$ 2.48/cm length

e. CRYSTAL COST DISCUSSION

The cycle times and costs presented above are considered baseline costs. That is, these costs are realistic based on knowledge gained during the course of the current investigation. There are a number of technical hurdles in achieving semicontinuous growth, however, and the costs in that case may be optimistic. Although the multicharge experimental results were somewhat inconclusive, the approach of using nugget polysilicon appears sound and fairly straightforward puller modifications would be required to achieve this operational mode.

ORIGINAL PAGE IS
OF POOR QUALITY

Figure 53 shows a graphical breakdown of crystal costs for the three 18-kg crucible cases. Single-charge pulls are overwhelmingly dominated by polysilicon and materials costs which represent 85% of the total crystal cost. In the multicharge and semicontinuous operational modes, these costs are approximately 80% of the total.

Figure 54 shows the impact of yield on the crystal costs for the various cases. It should be noted that a 100% yield, as defined here, is based on good cm crystal out, not on grams out. The bottom tapers and button left in the crucible are not counted against yield. Thus, if the entire crystal is within resistivity specification and diameter control is perfect, negating the need for grinding, a 100% yield is possible. In routine, high-volume production with a wide resistivity range yields of 80-90% should be achievable. Figures 53 and 54 illustrate the large cost advantage of multiple crystals from a single run. This advantage is gained primarily by the reduction in operating materials costs when these costs are spread over much greater crystal length.

The influence of pull rate on crystal cost is illustrated in Figure 55. The baseline costs presented above assumed 9 cm/h pull rates for single and multicharge runs and an average 10.8 cm/h pull rate for the semicontinuous case. Figure 55 indicates that only a few percent decrease in crystal cost would be gained by increasing the pull rates beyond the baseline values.

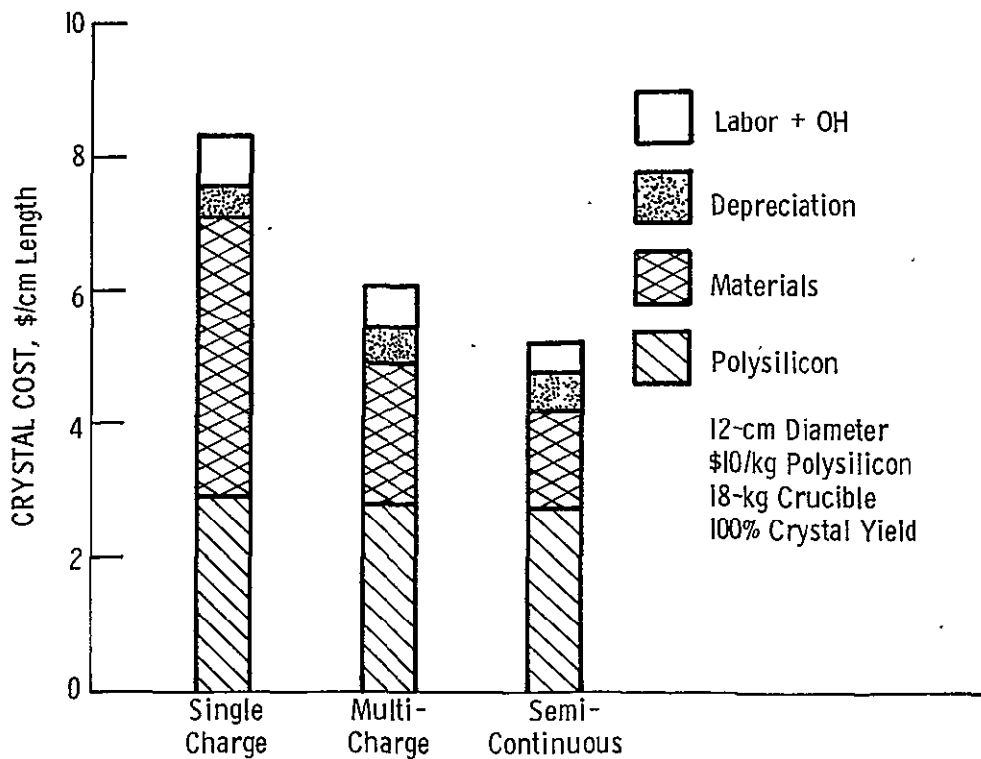


Figure 53. Czoehrski Silicon Costs

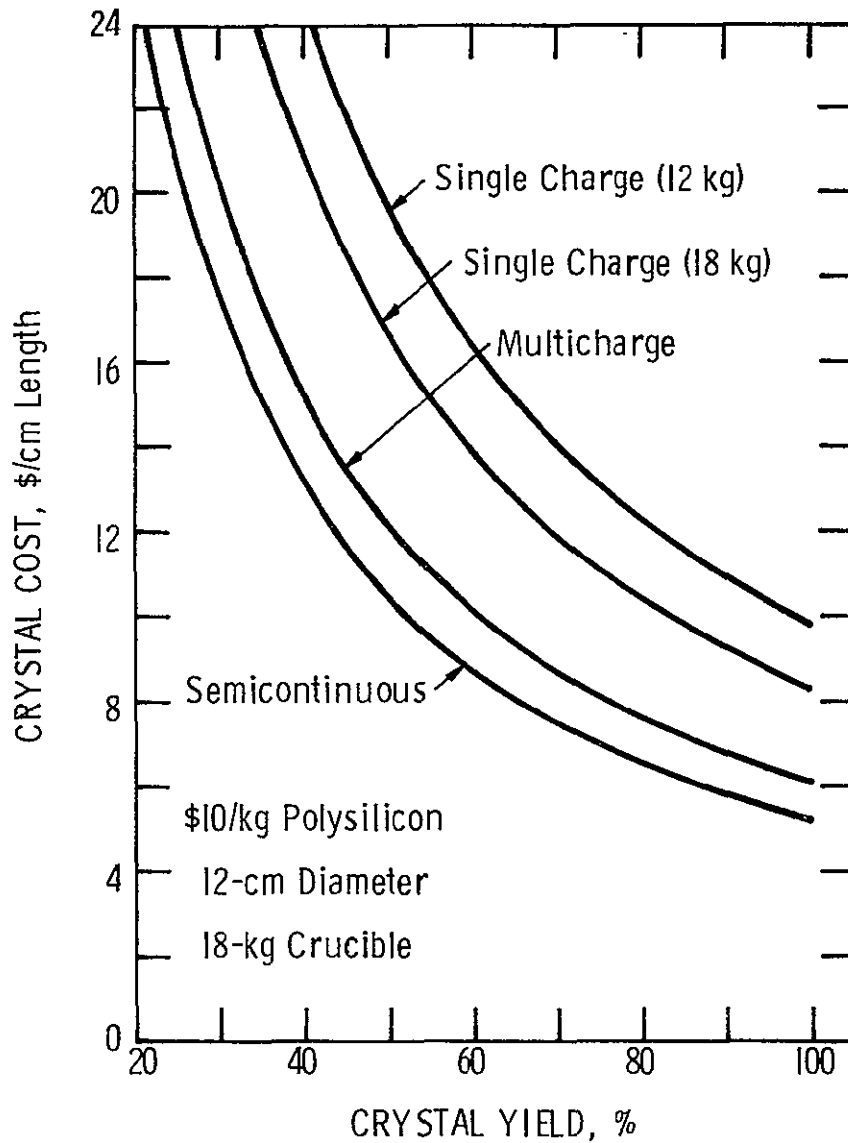


Figure 54. Silicon Crystal Cost

Figures 56 and 57 examine variations from the baseline costs for semicontinuous growth. Figure 56 indicates a 6% improvement in cost could be gained by pulling four crystals instead of three. By increasing the crystal length per pull to 103 cm, a 5% decrease in cost from the baseline could be realized (Figure 57).

ORIGINAL PAGE IS
OF POOR QUALITY

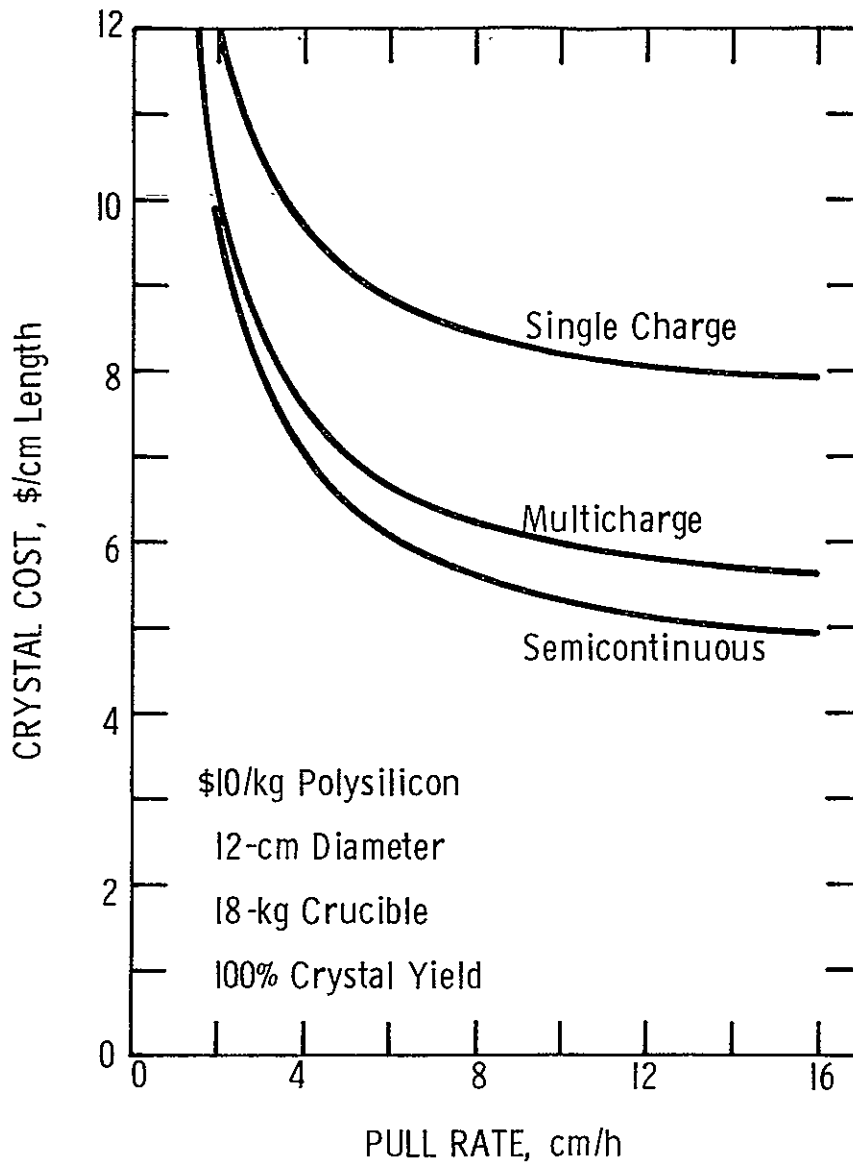


Figure 55. Silicon Crystal Costs as a Function of Pull Rate

4. Crystal Slicing Cycle Time

A number of options have been investigated in the slicing work utilizing multi-blade sawing including silicon carbide slurries, boron carbide slurries, crystal spinning, and diamond-plated blades. In slurry sawing, boron carbide has exhibited the fastest cutting rates but its cost of \$40/kg does not make it cost-effective. Diamond blades coupled with crystal spinning have produced the highest sawing rates of all options but this technology requires extensive developmental work to be a truly viable process. Thus, for a baseline slicing process, slurry sawing utilizing silicon carbide abrasive has been selected.

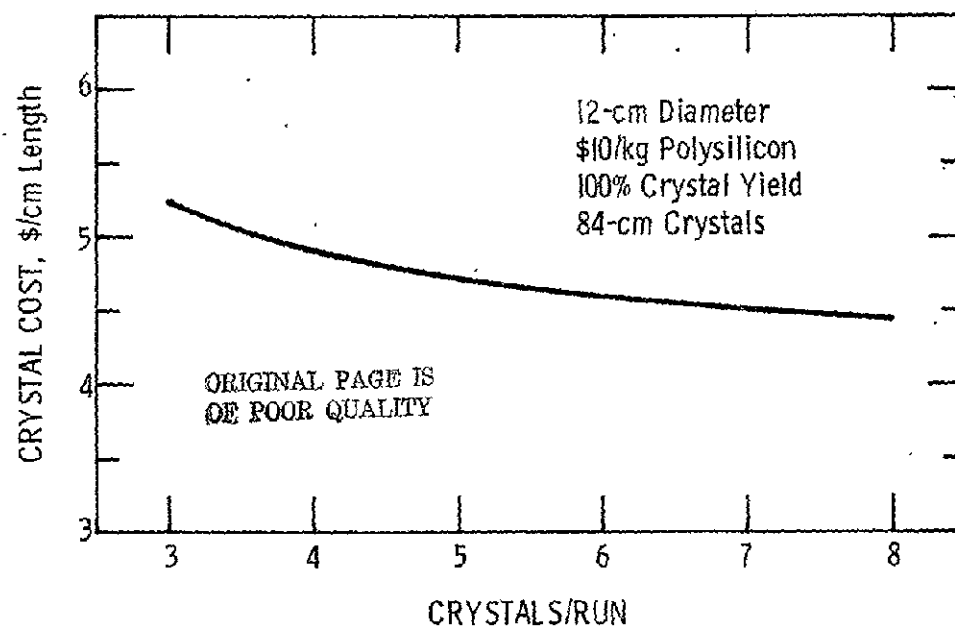


Figure 56. Variation of Semicontinuous Growth Costs with the Number of Crystals/Run

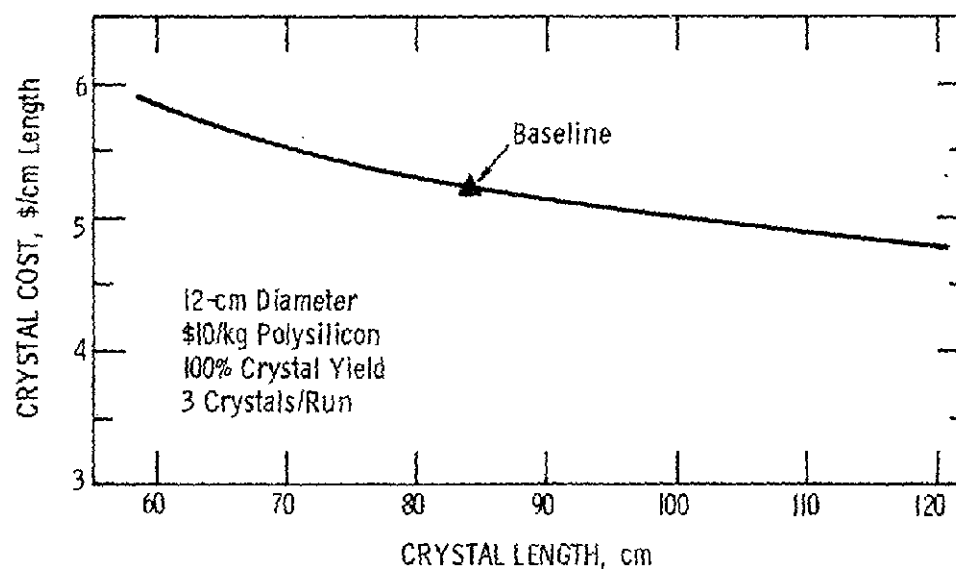


Figure 57. Influence of Crystal Length/Pull on Semicontinuous Growth Costs

In slurry sawing, the abrasive size, slurry mixture, slurry flow rate, and blade load all affect the cutting rate. At present, for sawing 12-cm crystal, the best compromise appears to be 400-grit SiC abrasive in a mixture of 500 g/l PC oil utilizing 0.02 X 6.4-mm blades at 2 N/blade load. This combination of parameters results in a cutting rate around 5 mm/h. With this cutting rate, the basic cycle time is:

Install Blade Package	0.3 h
Mount Crystal	0.2
Saw Crystal	24.0
Cleanup	<u>0.3</u>
Total	24.8 h

5. Crystal Slicing Cost Assumption

- 1) Saw Cost is \$25,000
- 2) Seven-year, straight line depreciation
- 3) Seven-day week, 52-week year
- 4) 90% equipment utilization
- 5) Eight saws/operator
- 6) Direct labor at \$4.50/h
- 7) Supervision cost at 10% of direct labor
- 8) Miscellaneous overhead at 100% of total labor
- 9) One crystal, 28 cm long, sliced per run
- 10) Slice plus kerf is 0.56 mm (500 blades/pack)
- 11) SiC abrasive cost is \$2.20/kg
- 12) PC oil costs \$0.66/l
- 13) Saw blades are \$0.03/blade
- 14) Wafer area per run is 5.655 m^2 at 100% yield.

6. Crystal Slicing Costs

a. BASELINE PROCESS

Materials:	Abrasive (500 g/l)	\$ 8.80
	PC Oil (8 l)	5.28
	Blades (500 @ \$0.03)	15.00
	Miscellaneous	<u>1.00</u>
	Total Materials	\$30.08/run
Labor:	Direct: (24.8 h) (\$4.50/h)/8	\$13.95
	Supervision:	<u>1.40</u>
	Total Labor	\$15.35/run
Overhead:	100% total labor	\$15.35/run
Depreciation:	No. runs/yr/saw =	
	(24) (0.9) (7) (52)/24.8 = 317.0	.
	Depreciation/run =	
	\$25,000/(7) (317.0) =	\$11.27/run
Total Slicing Cost:		\$72.05/run
Slicing Cost: 100% yield		\$12.74/m ²

b. SLICING COST DISCUSSION

The baseline sawing process above was based on a slice + kerf thickness (K) of 0.56 mm which experimentally has given fairly good sawing results. This K value is derived from a 0.2 mm blade thickness and 0.36 mm spacer thickness. The resulting slices are typically in the 0.25-0.28 mm thickness range. Figure 58 illustrates the variation in sawing cost with K and as a function of sawing yield. By decreasing K to 0.5 mm, a 12% reduction in sawing cost could be effected. A K of 0.5 mm could be achieved by going to thinner saw blades (0.15 mm) although experimentally it has been difficult to obtain high yields at this thickness.

ORIGINAL PAGE IS
OF POOR QUALITY

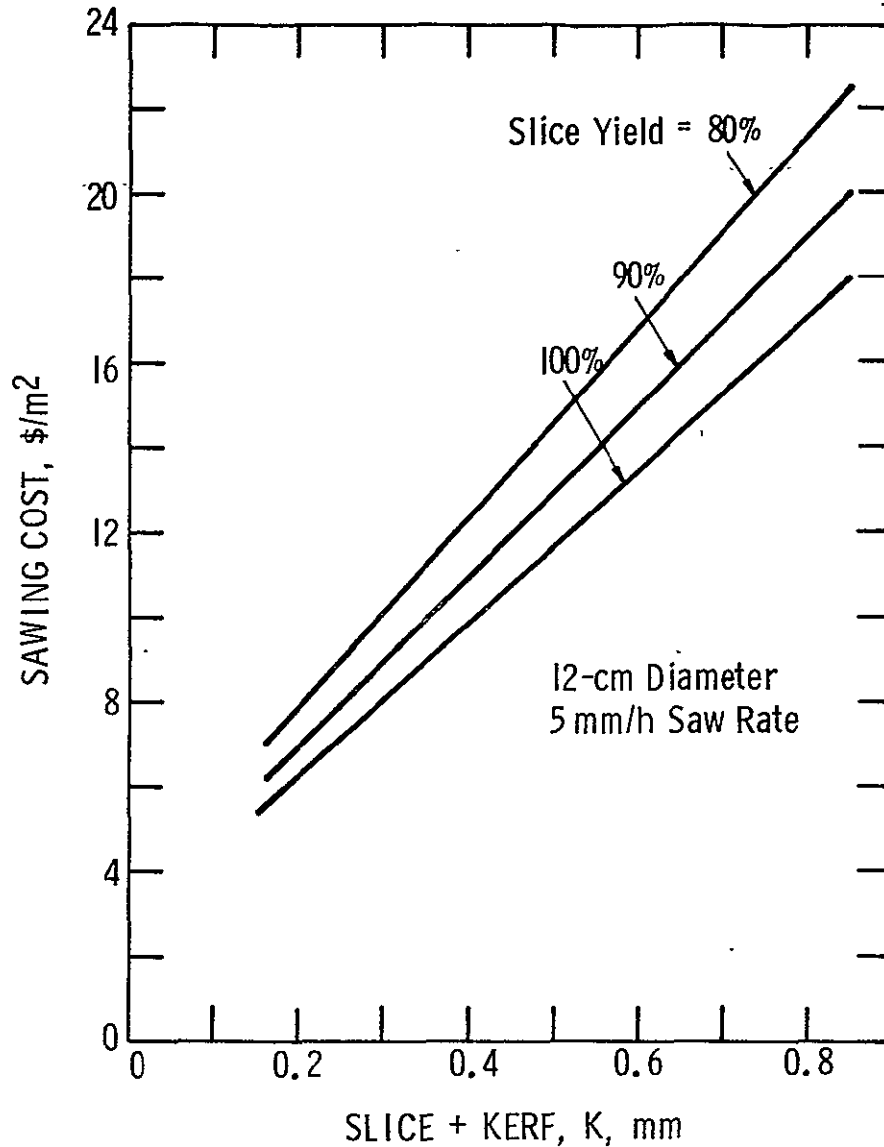


Figure 58. Multiblade Slurry Sawing Costs

Higher sawing rates reduce the sawing costs as Figure 59 indicates, although there is a bottom limit to cost. In the baseline process, materials account for \$5.31/m² of the total cost. As the saw rate is increased, depreciation decreases but the labor content will remain approximately constant due to the greater number of people required to set up the saws and handle the higher crystal throughput. Also, as the sawing cycle time decreases, set up becomes a greater percent of the cycle which adversely affects labor and depreciation costs. All these factors combined result in a minimum sawing cost at a cutting rate in the 10-12 mm/h range for the assumed baseline SiC costs given above. Under the cost assumptions depicted in Figure 59, the only way to increase cutting rate is to increase the blade force on the crystal and the blade reciprocation rate. From a practical standpoint it appears doubtful that cutting rates much in excess of 6 mm/h could be achieved by

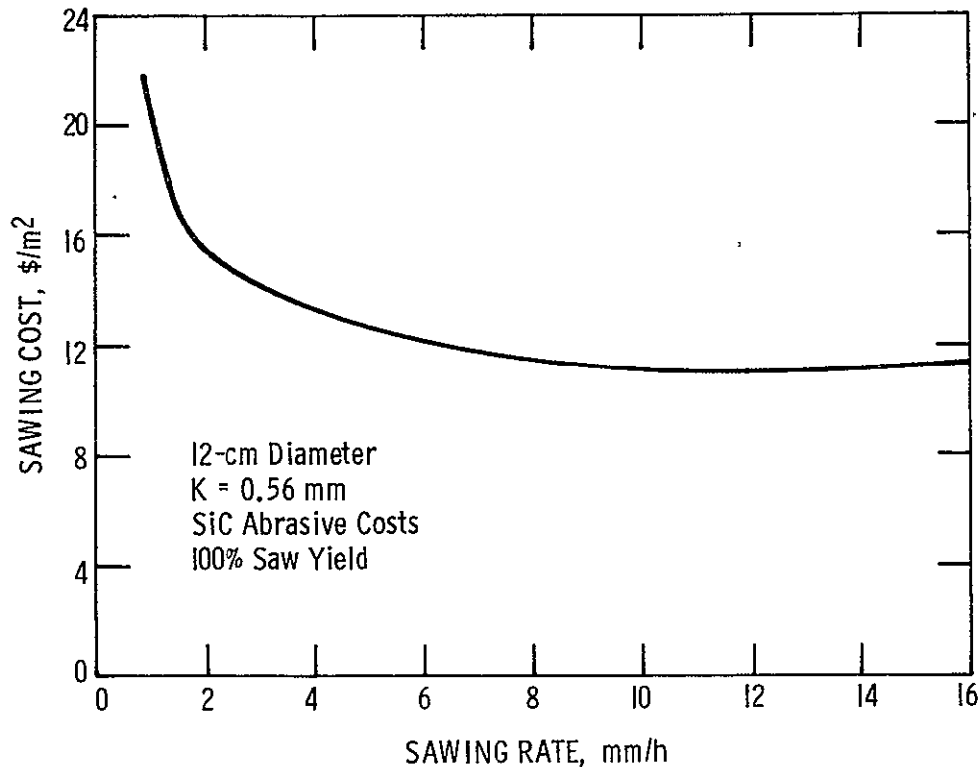


Figure 59. Effect of Sawing Rate on Multiblade Slurry Sawing Costs

increasing these parameters. Richer slurries are known to increase saw rates but then the cost assumptions built into Figure 59 no longer hold. A 50% slurry enrichment would raise the cost curve in Figure 59 approximately $\$0.77/\text{m}^2$ and at least a 25% improvement in cutting rate would be necessary to stay even with the $\$12.74/\text{m}^2$ baseline cost.

The assumed 8 saws/operator in the economic model includes backup labor for crystal preparation and mounting prior to installation on the saw. It is quite possible that with volume production and experience the labor costs could be reduced somewhat. A 10% labor reduction would result in a $\$0.50/\text{m}^2$ slicing cost reduction. Thus, overall it is believed that volume production coupled with process improvements in saw rate, set up, and slurry handling could reduce the sawing costs to the $\$11/\text{m}^2$ level.

ORIGINAL PAGE IS
OF POOR QUALITY

7. Other Costs

a. CRYSTAL GRIND

It is anticipated that automatic diameter control on the crystal puller will produce sufficiently uniform crystal so that grinding will not be necessary. However, in the event that at least some percentage of the crystals will require grinding, these costs are presented below.

Cost Assumptions

- 1) 28-cm crystal segments are ground
- 2) Two passes per crystal
- 3) Cycle time is 36 min
- 4) Four grinders per operator
- 5) Wheels are \$300 each
- 6) Wheel life is 500 crystals
- 7) Machine utilization is 90%
- 8) Grinder cost is \$40,000
- 9) Labor is \$4.50/h
- 10) Overhead is 100% of total labor.

Grind Costs

Materials:	Diamond Wheels	\$0.60
	Miscellaneous	<u>0.10</u>
	Total Materials	\$0.70/crystal
Labor:	Direct: (0.6 h) (\$4.50/h)/4	\$0.68
	Supervision:	<u>0.07</u>
	Total Labor	\$0.75/crystal
Overhead:	100% total labor	\$0.75/crystal
Depreciation:	No. runs/yr/grinder = (0.9) (24) (7) (52)/0.6 = 13,104 Depreciation/crystal = \$40,000/(7) (13104) =	
		<u>\$0.44/crystal</u>
Total Cost:		\$2.64/crystal
Grind Cost:	100% yield (500.slices/crystal)	\$0.47/m ²

b. WAFER CLEAN

After sawing, it is anticipated that the slices will be cleaned with an automated slice scrubber having cassette load/unload capability.

Cost Assumptions

- 1) Solvent cost is \$1.34/l
- 2) Solvent consumption is 5 ml/slice
- 3) Machine capacity is 120 slices/h
- 4) Eight machines/operator
- 5) Machine cost is \$20,000
- 6) Labor is \$4.50/h
- 7) Overhead is 100% total labor
- 8) Machine utilization is 90%.

Cleaning Costs

Materials:	$\$0.0067/\text{slice} =$	$\$0.59/\text{m}^2$
Labor:	$(\$4.50/\text{h})/(120) (8) = \$0.00469/\text{slice} =$	$\$0.41/\text{m}^2$
Supervision:		$\underline{0.04}$
	Total Labor	$\$0.45/\text{m}^2$
Overhead:	100% total labor	$\$0.45/\text{m}^2$
Depreciation:	Slices/machine/yr = $943,488 =$ $10,671 \text{ m}^2/\text{yr}$ Depreciation = $\$20,000/(7) (10,671) =$	
		$\$0.27/\text{m}^2$
Total Cleaning Costs: 100% yield		$\$1.76/\text{m}^2$

c. LASER SCRIBE

There is considerable uncertainty at this time whether 12-cm circular slices will be shaped into hexagons. In the eventuality that hexagonal slices will be cost effective, an estimate of laser scribing is given below.

Cost Assumptions

- 1) Laser lifetime is 300 operating hours
- 2) Scribe rate is 10 cm/s
- 3) Slice processing rate is 900/h per machine ($10.18 \text{ m}^2/\text{h}$)
- 4) Four machines/operator
- 5) Direct labor is \$4.50/h
- 6) Machine utilization is 85%
- 7) Replacement lasers are \$300 each
- 8) Machine cost is \$100,000.

Scribe Costs

Materials:	Laser	\$0.10/m ²
Labor:	Direct: (\$4.50/h)/4 (10.18)	\$0.11
	Supervision:	<u>0.01</u>
	Total Labor	\$0.12/m ²
Overhead:	100% total labor	\$0.12/m ²
Depreciation:		\$0.19/m ²
Total Cost:	100% yield	\$0.53/m ²

This cost is based on the incoming or circular slice area which makes the cost compatible with the other cost data presented in this report.

d. EDGE BEVELING

As in the case of laser scribe, this operation may not be necessary and its use will depend to some extent on the processing used to fabricate solar cells.

Cost Assumptions

- 1) Slice throughput is 125 slices/h (1.41 m²/h) per machine
- 2) Machine cost is \$15,000
- 3) Four machines/operator
- 4) Machine utilization is 85%
- 5) Direct labor is \$4.50/h
- 6) Diamond wheel life is 9000 slices/wheel
- 7) Abrasive wheels cost \$150 each.

Beveling Costs

Materials:	Abrasive wheels	\$1.47/m ²
Labor:	Direct: (\$4.50/h)/4 (1.41)	\$0.80
	Supervision:	<u>0.08</u>
	Total Labor	\$0.88/m ²
Overhead:	100% total labor	\$0.88/m ²
Depreciation:		\$0.20/m ²
Total Cost:	100% yield	\$3.43/m ²

Edge beveling costs appear too high to be considered in a Czochralski sheet process. Slice throughput per machine and diamond wheel life would each have to be increased by an order of magnitude to make this operation remotely feasible. The above costs are extrapolations of current technology on 76 mm slices and there are no indications of any dramatic cost breakthroughs pending for this process.

8. Czochralski Sheet Cost

The crystal growth and sawing cost models can be combined into a single Czochralski sheet cost. Figure 60 presents this cost as a function of slice plus kerf thickness and crystal yield. Figure 60 indicates a sheet cost around \$47/m² for 80% crystal yield, 95% saw yield, and $K = 0.56$ mm. Since the crystal cost already accounts for taper and button losses, an 80% yield should be attainable in practice. The sheet cost is very sensitive to the K value. A K of 0.5 mm would reduce the sheet cost to \$42/m² assuming the same crystal and saw yields.

Figure 61 presents the sheet cost with polysilicon costs subtracted out. The add-on cost for a slice plus kerf of 0.56 mm is around \$29/m² for the above yield values. By decreasing K to 0.5 mm, this cost could be lowered to around \$26/m².

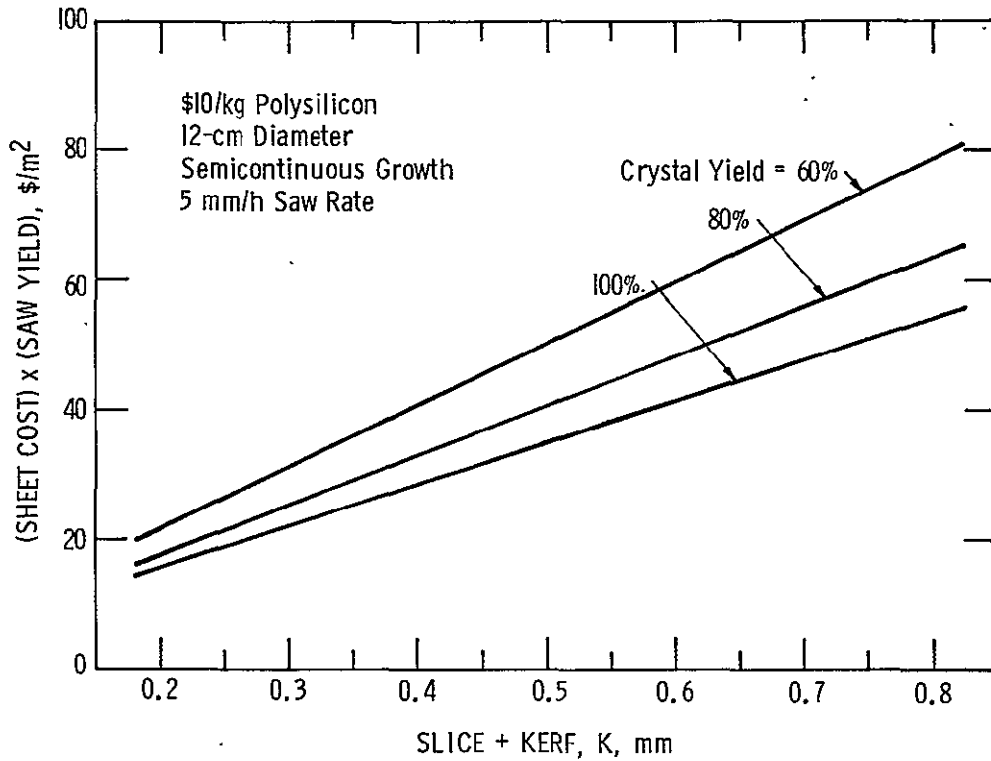


Figure 60. Czochralski Silicon Sheet Cost

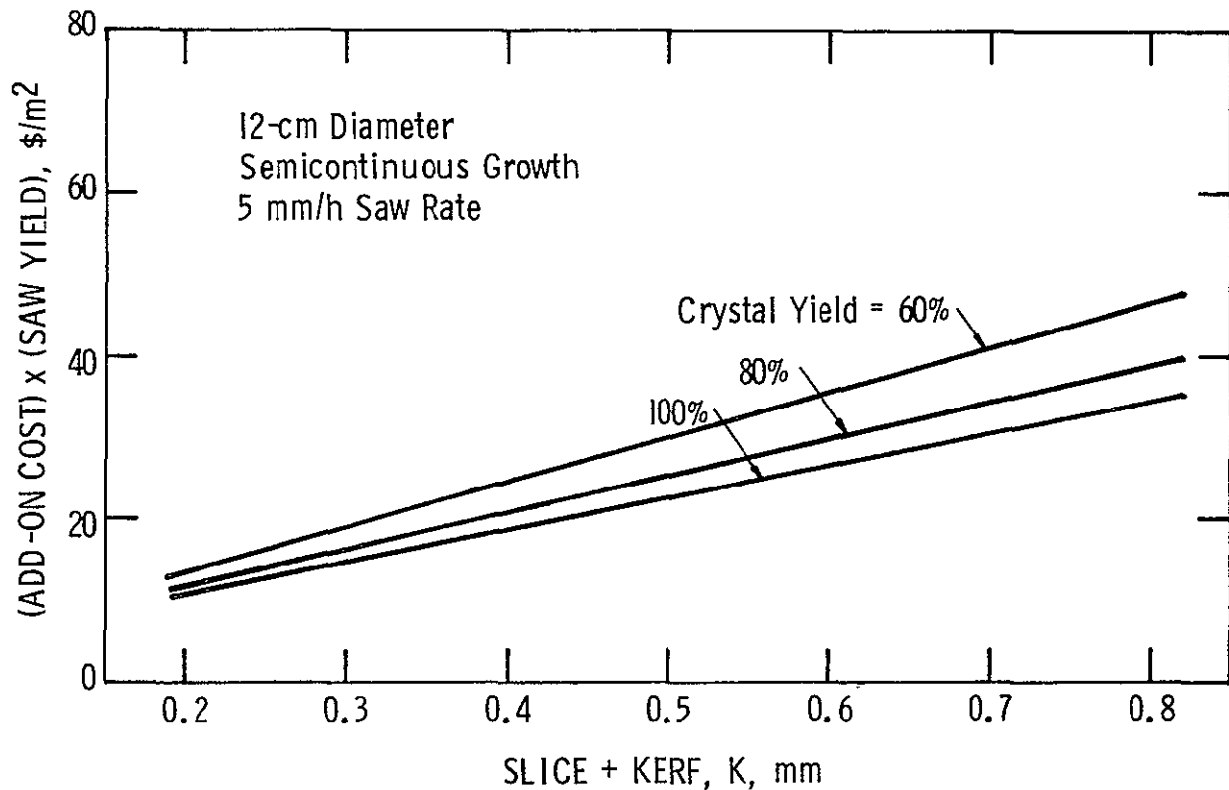


Figure 61. Czochralski Silicon Sheet Cost Exclusive of Polysilicon

The influence of crystal diameter on costs is depicted in Figures 62 and 63. In those figures the crystal costs are based on assumptions and models identical to the 12-cm cases presented in detail. The only variation is in the pull rate which was assumed to vary from the 12-cm case as the inverse square root of diameter. The add-on cost for 15-cm crystal (Figure 63) with a K of 0.5 mm is around \$18.50/m² compared to \$26/m² for 12-cm crystal.

Figures 60-63 do not include wafer clean or other costs derived in the preceding section. Thus, an additional cost of around \$1.80/m² must be added to include slice cleanup after sawing. However, the baseline process is believed to be somewhat conservative and improvements in yields, crystal pull rates, and sawing rates could compensate for some additional cost.

The cost models presented are projections based on an extrapolation of current Czochralski technology. Semicontinuous crystal pullers do not exist although there do not appear to be any overwhelming barriers to their development. Rapid sawing of 12-cm crystal into thin slices with high overall process yield is not presently a reality primarily because current technology does not utilize the multiblade saw for silicon slicing. Thus, benefit of an experience curve is not available. Also, techniques to enhance multiblade sawing such as crystal spinning have not been modeled but preliminary glances at the economics suggest that substantial sawing cost reductions on the order of \$5/m² might be possible. Crystal spinning would require a new concept in multiblade saw design although redesign of the current multiblade saw will be necessary to allow 28-cm long crystals and their attendant 500 or more blades.

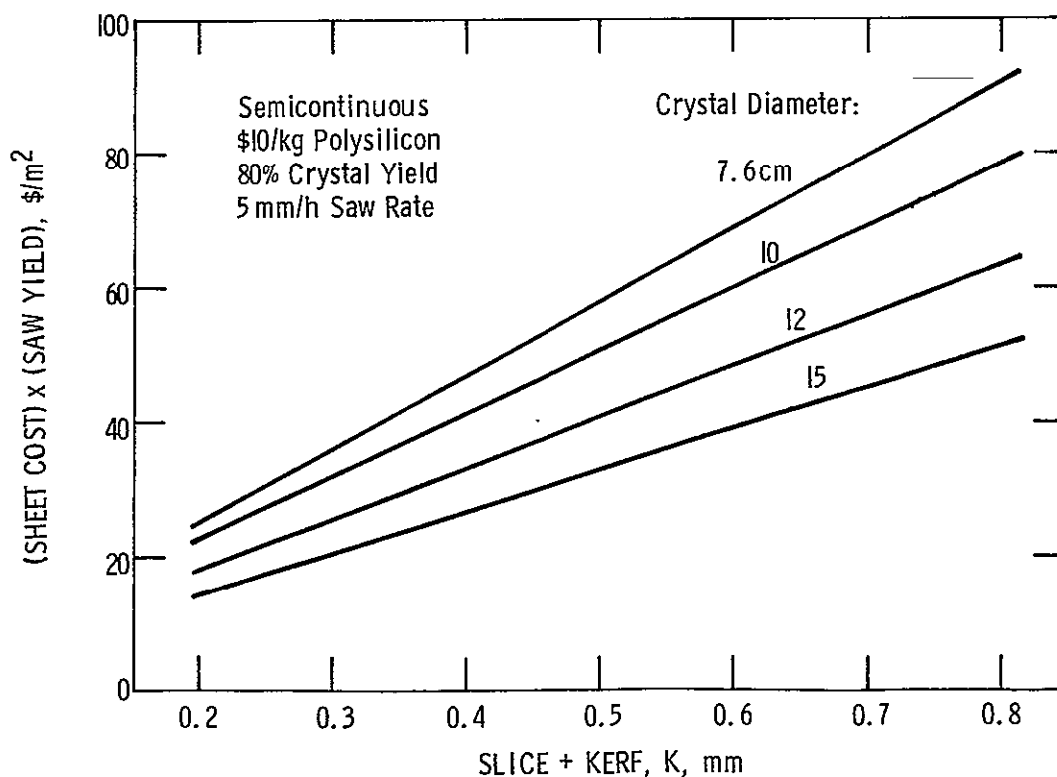


Figure 62. Czochralski Silicon Sheet Cost

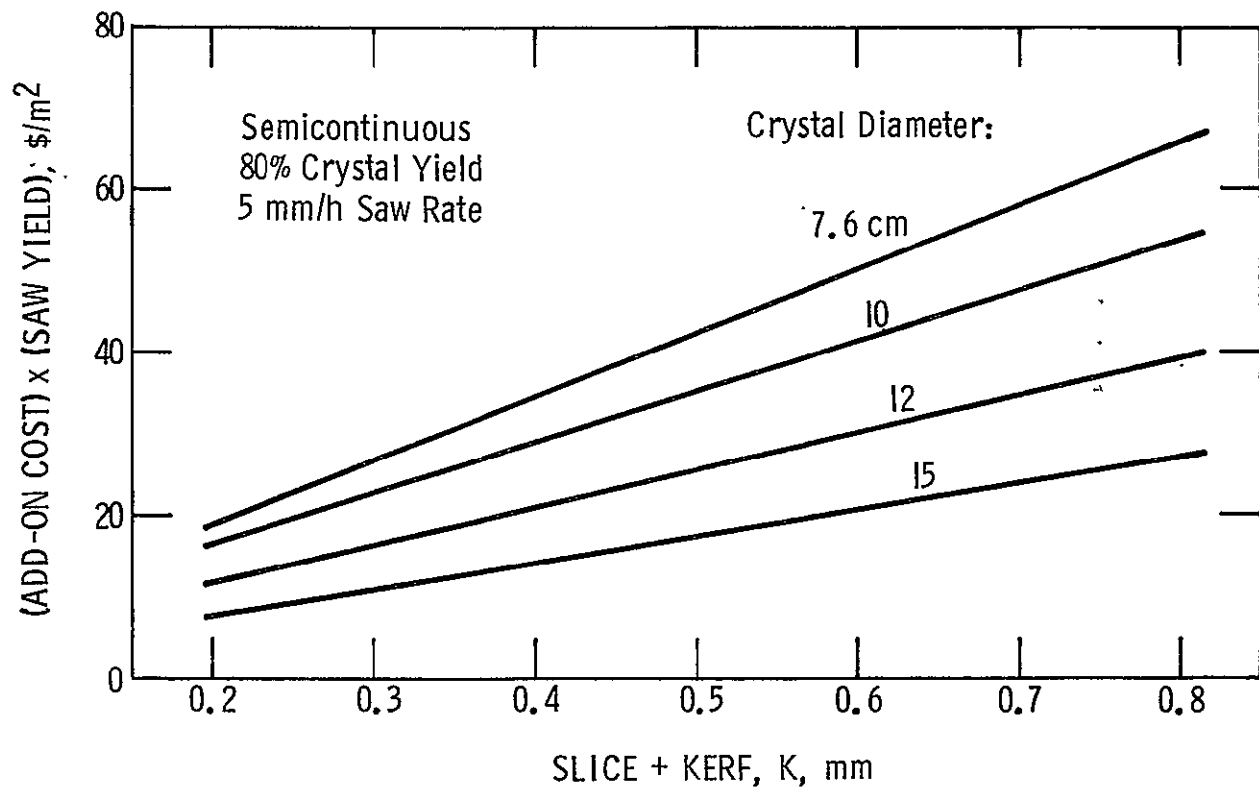


Figure 63. Czochralski Silicon Sheet Cost Exclusive of Polysilicon

ORIGINAL PAGE IS
OF POOR QUALITY.

SECTION III

CONCLUSIONS AND RECOMMENDATIONS

Crystal growth modeling and experimental work on this program indicated:

- 1) Pull rate enhancement techniques such as employing cold coils around the growing crystal or funneling ambient gas over the crystal have minor effects on the maximum pull rate possible.
- 2) The maximum pull rate varies inversely as the square root of crystal diameter.
- 3) The practical pull rate limit for single-charge pulls of 12-cm crystal is 10 cm/h.
- 4) Puller ambient temperature has a negligible influence on pull rate provided it is held below 600 K.
- 5) The maximum pull rate possible for 12-cm crystal pulled in a conventional vacuum RH (resistance heated) puller is approximately 17.5 cm/h assuming semicontinuous growth in which the melt level is maintained constant relative to the crucible lip.
- 6) Routine evaluation of 12-cm crystals indicates the quality to be equivalent to that of smaller crystal.
- 7) Multicharge crystal growth feasibility was demonstrated from an equipment standpoint but development work is required to improve the process and ensure high crystal yields. A major problem is carbon incorporation into the melt which must be minimized or else single crystal growth will be impossible.
- 8) Argon consumption on current vacuum RH Cz pullers is excessive and could become a major cost item. Development of a puller utilizing atmospheric pressure argon could provide several cost benefits: (1) decreased argon consumption, (2) capital and maintenance costs on large vacuum pumps would be eliminated, and (3) a slightly higher pull rate would be possible in a one-atmosphere ambient.

PRECEDING PAGE BLANK NOT FILMED

Experimental work on the multiblade slurry saw indicates it to be an attractive wafering approach for large diameter crystal. Slice thicknesses of 0.25 mm can be achieved with high saw yields. This slice thickness results in a slice plus kerf of 0.56 mm which, at this time, is the minimum practical consistent with 90% and higher yields. Other specific observations include:

- 1) Sawing rates are directly proportional to blade load and speed.
- 2) Cutting rates of 5 mm/h are obtainable with SiC abrasive and B₄C abrasive is about 2.5 times higher. However, the greatly higher cost of B₄C makes its use prohibitively expensive.
- 3) SEMs of new and used abrasive indicate minimal particle wear so that slurry mixtures can be reused. This was done with B₄C abrasive in one instance with no apparent degradation in cutting rate. Also, the multiple crystal sawing experiments indicate sawing rates are not a function of kerf volume being removed. Thus, recycling slurry mixtures is a distinct possibility and would result in a cost savings in the sawing economic model.
- 4) The best blade size is 0.2 X 6.35 mm. No problems were encountered in sawing 12-cm crystals with these blades. Thinner blades exhibit significantly lower saw yields due to slice breakage.
- 5) As-sawed slices have a lapped appearance and can be readily processed into solar cells after a texture etch. Saw damage depth increases with blade load with 33 μ m being maximum at 2.5 N loads.

The economics of the Czochralski process using realistic technical parameters indicate a sheet cost in the \$45/m² area for a semicontinuous puller and \$10/kg polysilicon. This represents an add-on cost in the neighborhood of \$30/m². A multicharge process could be onstream in the late 1970s with an add-on cost around \$40/m². These costs all assume successful development of a multiblade saw capable of handling 28-cm crystal lengths. Also, blade costs must be reduced to the \$0.03/blade area which is a theoretical lower limit assuming automated blade pack assembly.

SECTION IV
NEW TECHNOLOGY

No new technology was developed on this program.

SECTION V
REFERENCES

1. J. C. Brice, *J. Crystal Growth* 2, 395 (1968).
2. T. F. Ciszek, *J. Appl. Phys.* 47, 440 (1976).
3. W. R. Wilcox and R. L. Duty, *J. Ht. Trans* 88, 45 (1966).
4. V. H. S. Kuo and W. R. Wilcox, *J. Crystal Growth* 12, 191 (1972).
5. R. Siegel and J. R. Howell, *Thermal Radiation Heat Transfer*, McGraw-Hill, Chap. 8 (1972).
6. S. P. Timoshenko and J. M. Gere, *Theory of Elastic Stability*, McGraw-Hill, Chap. 6 (1961).
7. J. P. Den Hartog, *Advanced Strength of Materials*, McGraw-Hill, Chap. 8 (1952).
8. J. P. Den Hartog, *Mechanical Vibrations*, McGraw-Hill, Chap. 4 (1956).
9. J. W. Faust, Jr., *Electrochem. Tech.* 2, 339 (1964).
10. R. L. Meek and M. C. Huffstutler, Jr., *J. Electrochem. Soc.* 116, 893 (1969).

PRECEDING PAGE BLANK NOT FILMED

APPENDIX A THERMAL PROPERTY DATA

A. SILICON THERMAL CONDUCTIVITY

Table A-1 gives the values of silicon thermal conductivity used in the thermal analysis of Section II.A. The data in the table are basically those of Glassbrenner and Slack.¹

The conductivity data in Table A-1 were least squares curve-fit for use in the differential equations describing the crystal temperature distribution. By defining a normalized temperature $T_1 = T/1600$ with T in Kelvin, the following eighth-order equation fits the data in Table A-1 within 3%:

$$k = P_0 + P_1 T_1 + P_2 T_1^2 + P_3 T_1^3 + P_4 T_1^4 + \dots + P_8 T_1^8 \quad (1)$$

with

$$P_0 = 1.00412 \text{ E}01$$

$$P_1 = -1.12996 \text{ E}02$$

$$P_2 = 6.15319 \text{ E}02$$

$$P_3 = -1.92369 \text{ E}03$$

$$P_4 = 3.68613 \text{ E}03$$

$$P_5 = -4.40809 \text{ E}03$$

$$P_6 = 3.21316 \text{ E}03$$

$$P_7 = -1.30749 \text{ E}03$$

$$P_8 = 2.27842 \text{ E}02$$

ORIGINAL PAGE IS
OF POOR QUALITY

Table A-1. Silicon Thermal Conductivity

Temperature K	Conductivity W/cm-K	Temperature K	Conductivity W/cm-K
300	1.47	1100	0.288
400	0.994	1200	0.261
500	0.764	1300	0.251
600	0.617	1400	0.236
700	0.511	1500	0.233
800	0.423	1600	0.225
900	0.360	1685	0.220
1000	0.311		

The thermal conductivity, k , in Eq. (1) is in W/cm-K. The rather high order fit in Eq. (1) was necessary to obtain sufficient accuracy on the first derivative of k with respect to temperature.

B. SILICON SPECIFIC HEAT

Shanks,² et al., present silicon specific heat data as a function of temperature reproduced in Table A-2. In the thermal analysis work of Section II.A a mean value of specific heat, c , was used given by Runyan³ of 9.17 E02 J/kg-K. This value represents the specific heat at 1023 K.

Table A-2. Silicon Specific Heat

Temperature K	Specific Heat J/kg-K	Temperature K	Specific Heat J/kg-K
273	6.91 E02	873	8.98 E02
373	7.70	973	9.13
473	8.25	1073	9.27
573	8.48	1173	9.42
673	8.65	1273	9.59
773	8.81	1373	9.82

C. SILICON EMISSIVITY

The total emissivity as a function of temperature was estimated using ref. 4 combined with measurements made at Texas Instruments at the melting point and room temperature. Figure A-1 shows the idealized emissivity curve used in the thermal analysis.

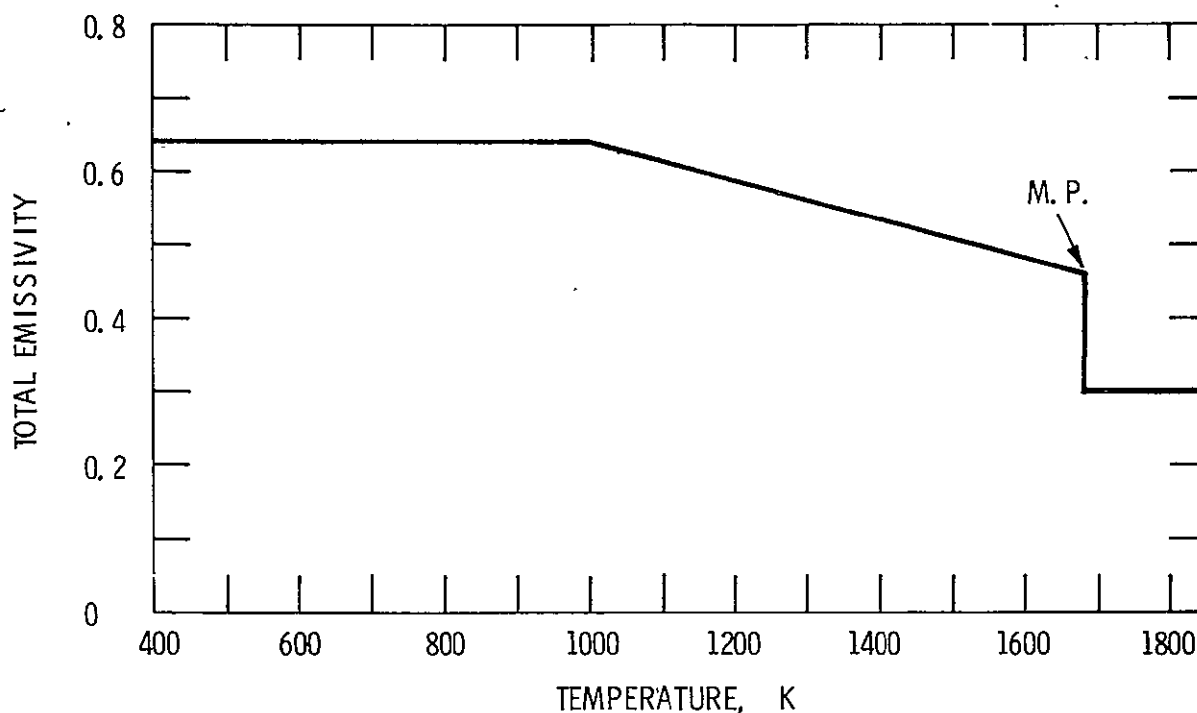


Figure A-1. Estimated Total Emissivity of Silicon

D. FUSED SILICA EMITTANCE

The crucible liners used in Czochralski crystal growth are made from fused silica. Reference 5 gives a value for total normal emittance at 1200 K of 0.60. In radiation heat transfer analyses employing the diffuse-gray assumption, the total emittance is desired. Reference 6 gives the correction factor to be applied to convert normal emittance to total emittance for dielectrics. The correction factor in the case of fused silica is approximately 0.99. Therefore, the total emittance used in the thermal analyses for the quartz liner was $0.99 (0.60) = 0.59$.

E. ARGON THERMAL CONDUCTIVITY

In order to compute the effects of thermal convection on cooling a growing crystal, the transport properties of the ambient gas must be known. The thermal conductivity of argon at higher temperatures is given by:⁷

$$k = \frac{1.61 \sqrt{T} \text{ E-05}}{1 + (178.8/T)} \text{ W/cm-K} \quad (2)$$

where T is the gas temperature in Kelvin.

ORIGINAL PAGE IS
OF POOR QUALITY

F. ARGON SPECIFIC HEAT

Reference 8 indicates that the specific heat at constant volume is constant for argon from 0-2000°C. Then, the thermodynamic relation $c_p - c_v = R$ implies that the constant pressure specific heat is constant also over this temperature range. Thus,

$$c_v = 0.0746 \text{ cal/g-K} = 312 \text{ J/kg-K}$$

$$c_p = 0.124 \text{ cal/g-K} = 519 \text{ J/kg-K}$$

G. ARGON VISCOSITY

The absolute viscosity, μ , as a function of temperature is given in Table A-3.⁹

The kinematic viscosity is determined by dividing the absolute viscosity in Table A-3 by the density.

Table A-3. Absolute Viscosity of Argon

Temperature K	Viscosity Pa-s	Temperature K	Viscosity Pa-s
273	2.10 E-05	674	4.12 E-05
293	2.22	766	4.48
373	2.70	857	4.82
473	3.22	987	5.26
575	3.69	1100	5.63

H. HELIUM THERMAL CONDUCTIVITY

Helium thermal conductivity is given in Table A-4.⁹

Table A-4. Helium Thermal Conductivity

Temperature K	Conductivity W/cm-K	Temperature K	Conductivity W/cm-K
300	1.50 E-03	850	3.21 E-03
400	1.80	900	3.35
500	2.11	1000	3.63
600	2.47	1100	3.89
700	2.78	1200	4.16
800	3.07	1500	4.94

I. HELIUM VISCOSITY

Absolute helium viscosity is given in Table A-5.⁹

Table A-5. Absolute Viscosity of Helium

Temperature K	Viscosity Pa-s	Temperature K	Viscosity Pa-s
293	1.94 E-05	759	3.71 E-05
373	2.28	879	4.09
473	2.67	949	4.30
555	2.99	1090	4.71
680	3.44		

J. HELIUM SPECIFIC HEAT

The specific heat of helium is constant over a wide range of temperatures:¹⁰

$$c_v = 0.746 \text{ cal/g-K} = 3120 \text{ J/kg-K}$$

$$c_p = 1.24 \text{ cal/g-K} = 5190 \text{ J/kg-K}$$

K. REFERENCES

1. C. J. Glassbrenner and G. A. Slack, *Phys. Rev.* 134, A1058 (1964).
2. H. R. Shanks, P. D. Maycock, P. H. Sidles, G. C. Danielson, *Phys. Rev.* 130, 1743 (1963).
3. W. R. Runyan, *Silicon Semiconductor Technology*, McGraw-Hill, 213 (1965).
4. Ibid., p. 200.
5. S. Katzoff, ed., *Symposium on Thermal Radiation of Solids*, NASA SP-55, 251 (1965).
6. R. Siegel and J. R. Howell, *Thermal Radiation Heat Transfer*, McGraw-Hill, 104 (1972).
7. F. G. Keyes, *Trans. ASME* 77, 1395 (1955).
8. E. S. R. Gopal, *Specific Heats at Low Temperatures*, Plenum Press, 137 (1966).
9. R. C. Weast, ed., *Handbook of Chemistry and Physics*, 55th ed., CRC Press (1974).
10. E. R. G. Eckert and R. M. Drake, Jr., *Heat and Mass Transfer*, McGraw-Hill, 504 (1959).

APPENDIX B

CRYSTAL THERMAL CONVECTION

Thermal convection between a growing crystal and its ambient environment is governed by the natural convection relation.¹

$$Nu = 0.638 [GrPr^2/(0.861 + Pr)]^{1/4} \quad (1)$$

where

$$Nu = \text{Nusselt number} = hL/k \quad (2)$$

$$Gr = \text{Grashof number} = g \beta (T_w - T_a) L^3/\nu^2 \quad (3)$$

$$Pr = \text{Prandtl number} = \mu c_p/k \quad (4)$$

Once the right side of Eq. (1) is determined, the average heat transfer coefficient, h , is computed by Eq. (2). This heat transfer coefficient governs the rate of heat removal from the crystal surface to its environment and is the "h" in the differential equation describing the temperature distribution along the crystal.

An examination of Eqs. (1-4) shows that h is a function of crystal and ambient temperatures, puller pressure, and the crystal length. The puller pressure enters through the Grashof number which is proportional to the pressure squared. As the puller interior pressure decreases, Gr decreases and, hence, h decreases. Thus, crystals pulled under partial vacuum have a lower average h than ones pulled at atmospheric pressure.

Equation (1) holds only for values of $GrPr > 10^4$. At lower values of the Grashof-Prandtl product there is no convection and crystal cooling is only by thermal radiation. In practice this limitation means that below certain pressures convection ceases, the critical convection pressure depending upon the particular ambient gas. Specific cases will be computed below.

¹W. M. Rohsenow and H. Choi, *Heat, Mass, and Momentum Transfer*, Prentice-Hall, 159 (1961).

ORIGINAL PAGE IS
OF POOR QUALITY

The gas properties μ (viscosity), c_p , k (conductivity), ν (μ/ρ), and β ($1/T$ for a perfect gas) are all computed at the average temperature between the crystal surface (T_w) and the ambient temperature (T_a). Since the crystal surface temperature varies along its length, h will therefore vary but it is usually sufficiently accurate to assume some nominal temperature at which to evaluate properties and, thereby, fix a value of h . This h will, however, hold for only one value of L . In the following calculations it is assumed that the average gas temperature is 850 K.

A. ARGON

At 850 K, from Appendix A,

$$k = 3.88 \text{ E-04 W/cm-K}$$

$$\mu = 4.79 \text{ E-05 Pa-s}$$

$$c_p = 519 \text{ J/kg-K}$$

$$Pr = c_p \mu / k = 0.641$$

From Eq. (1),

$$Nu = 0.461 Gr^{1/4} \quad (5)$$

To complete the evaluation of h , the Gr number must be computed and used in Eq. (5). Assume a puller pressure of 10 mm Hg (1330 Pa). At this pressure, the argon density is 0.00754 kg/m^3 for 850 K. With a ($T_w - T_a$) of 500 K, the product $\beta(T_w - T_a) = 0.588$. Then, from Eq. (3) $Gr = 1140$ and the product $GrPr = 733$ which is below the threshold value of 10^4 for convection to exist. Thus, at 10 mm Hg puller pressure there is no convection cooling of the crystal. A quick calculation indicates that a minimum puller pressure of 37 mm Hg (4930 Pa) is required in this case to support natural convection. At 37 mm Hg pressure the Gr number is $1.56 \text{ E}04$ and from Eq. (5)

$$Nu = 5.15$$

and

$$h = 5.15 (k/L) = 10^{-4} \text{ W/cm}^2\text{K}.$$

By examining various limiting cases of crystal length, pressure and temperature, it is possible to map out a domain of the heat transfer coefficient and such a range of h is shown in Figure B-1. Generally, the heat transfer coefficients are quite low in argon unless the puller is operating at ambient pressures near atmospheric. The longer the crystal the lower the ambient pressure which will support convection cooling. However, long crystals exhibit very low values of h ($6 \times 10^{-5} \text{ W/cm}^2\text{K}$) at normal puller operating pressures of 10-30 mm Hg. For perspective, such heat transfer coefficients are two orders of magnitude lower than those of air-cooled circuit boards.

B. HELIUM

Helium is used in some instances as an ambient environment for Czochralski crystal growth. Heat transfer coefficients for helium are computed in exactly the same way as those for argon given above. Again, for an assumed average temperature of 850 K:

$$k = 3.21 \text{ E-03 W/cm-K}$$

$$\mu = 4.00 \text{ E-05 Pa-s}$$

$$c_p = 5190 \text{ J/kg-K}$$

$$\text{Pr} = 0.647$$

From Eq. (1),

$$\text{Nu} = hL/k = 0.463 \text{ Gr}^{1/4} \quad (6)$$

With the criterion that $\text{GrPr} > 10^4$, it is possible to compute a nominal domain of heat transfer coefficients for helium similar to that for argon. Figure B-1 includes this helium domain along with that for argon.

C. DISCUSSION

Figure B-1 indicates that helium is a better heat transfer medium than argon at ambient pressures near atmospheric. However, the effectiveness of helium diminishes rapidly with decreasing pressure. At typical puller pressures of 10-30 mm Hg helium is out of the convection range entirely.

Heat transfer coefficients given by Eq. (1) and shown in Figure B-1 are a fairly weak function of temperature. Thus, the results presented here for 850 K average gas temperature are representative of average Czochralski puller conditions.

ORIGINAL PAGE IS
OF POOR QUALITY

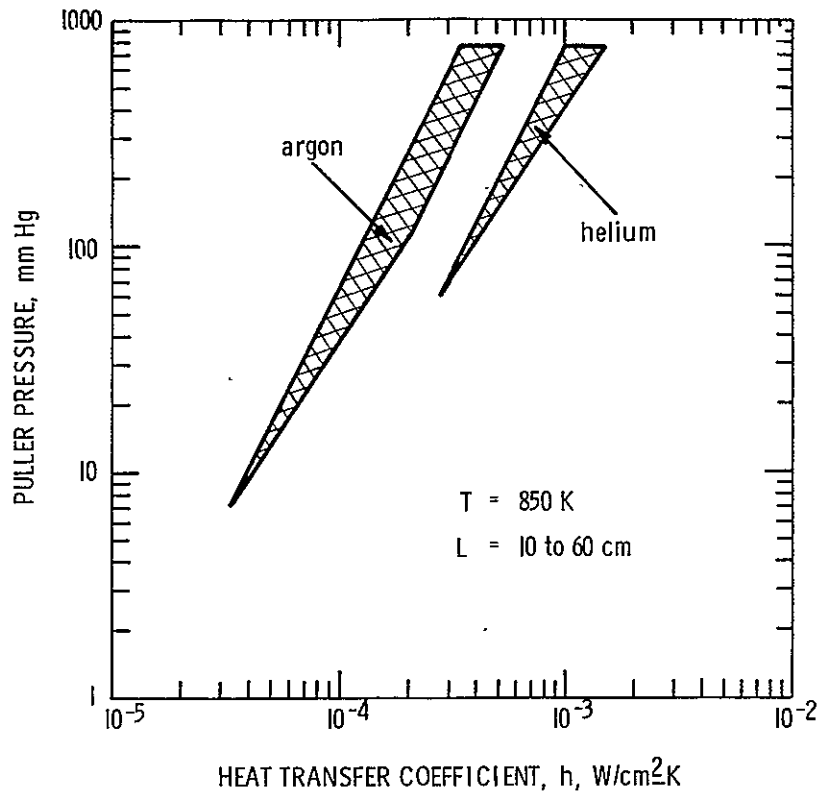


Figure B-1. Crystal Heat Transfer Coefficients

Direct gas impingement can increase the heat transfer coefficients by a factor of 10 and funneling the gas over the crystal can effect increases of two to three. However, the low overall magnitude of the coefficients at operating puller pressures indicate that such augmentation techniques would not be worthwhile for increasing pull rates. This conclusion is borne out by the analytical results shown in Section II.A of this report. For vacuum conditions, it is safe to assume no thermal convection between ambient gas and crystal and that the heat transfer from the crystal is governed entirely by thermal radiation between the crystal, crucible, and chamber walls.

APPENDIX C
METHOD FOR COMPUTING RADIATION VIEW FACTORS FOR
CYLINDRICAL GEOMETRIES

The following reprint describes a methodology for computing radiation view factors for cylindrical geometries. These view factors are necessary in formulating the equations describing heat transfer between a growing crystal and its melt and crucible. Figure 2 in the reprint depicts the crystal and its melt surface and configuration I in Figure 1 with $B = 0$ is an idealized representation of the crystal/crucible combination.

ORIGINAL PAGE IS
OF POOR QUALITY.

Rapid Method for Determining Concentric Cylinder Radiation View Factors

Samuel N. Rea*

Texas Instruments Incorporated, Dallas, Texas

Nomenclature

F_{di-j}	= view factor from elemental area i to surface j
F_{i-j}	= view factor from surface i to surface j
$F_{(Y-a)}$	= shorthand notation for cylinder-disc view factor, Fig. 3, with $t/r = (Y-a)/r$, etc.
r	= inner cylinder radius
R	= outer cylinder radius

Introduction

CONCENTRIC cylinders are among the more common configurations encountered in radiation heat transfer analyses, being descriptive of assemblies ranging from infrared telescopes to tube furnaces. In performing thermal analyses on such structures with finite-element computer programs, it is often necessary to break the shell and tube into various concentric ring elements and compute radiation view factors between these elements. Figure 1 depicts a collection of concentric cylindrical geometries. In general, the tube-shell view factors of Fig. 1 can be determined using available computer programs which numerically integrate over the areas involved. However, these programs are cumbersome, thereby limiting their casual usage.

A recent paper by Reid and Tennant¹ numerically analyzed configuration IV in Fig. 1 for the special case where $L=Y$. The more general case, along with the other configurations in Fig. 1, is not in the open literature, although the equal-length case is given in Ref. 2. The novelty of the method presented in this Note lies in the utilization of the cylinder-disk view factor F_{i-2} of Figs. 2 and 3. By combining various cylinder-disk view factors, for any of the structures in Fig. 1 F_{i-3} can be determined in closed form where it is the diffuse view factor from the outer curved surface of the inner tube to the outer cylinder. The view factors from the ends of the inner cylinder to the outer cylinder in configurations II, III, and IV are not considered since they can be determined using disk-disk relations² as can the shell-shell view factors.¹ Of course, F_{3-4} can be readily computed from F_{1-3} using reciprocity.

Analysis

A literature survey indicates that the cylinder-disk view factor is not explicitly available so it is derived first and then applied to the Fig. 1 structures. By definition,³ with the geometry of Fig. 2:

$$F_{1-2} = \frac{1}{l} \int_0^l F_{d1-2} dx \quad (1)$$

where F_{d1-2} can be derived from Ref. 4:

$$2\pi F_{d1-2} = \cos^{-1} \frac{x^2 - R^2 + r^2}{x^2 + R^2 - r^2} - \left(\frac{x}{r} \right) \left[\frac{x^2 + R^2 + r^2}{\{(x^2 + R^2 + r^2)^2 - 4R^2r^2\}^{1/2}} \times \cos^{-1} \frac{r(x^2 - R^2 + r^2)}{R(x^2 + R^2 - r^2)} - \cos^{-1} \left(\frac{r}{R} \right) \right]$$

Received February 3, 1975; revision received March 28, 1975.
Index category, Radiation and Radiative Heat Transfer.

*Engineering Supervisor.

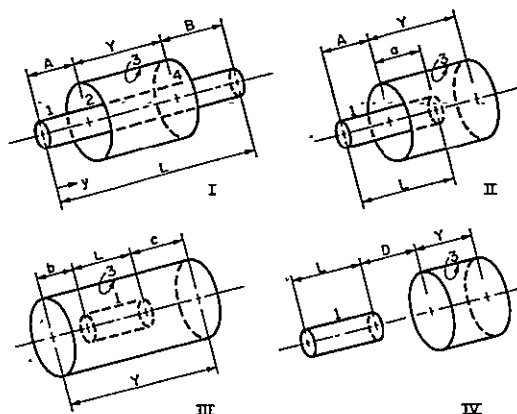


Fig. 1 Concentric cylinder configurations.

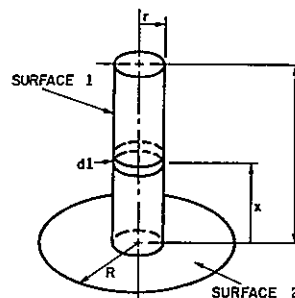


Fig. 2 Cylinder-disk view factor geometry.

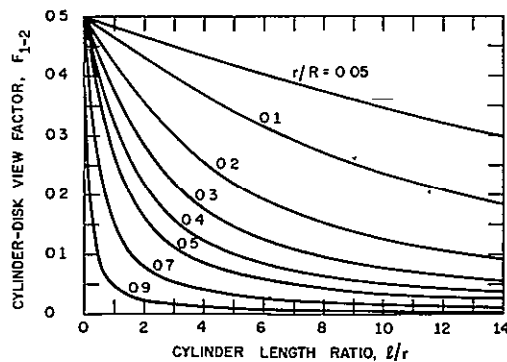


Fig. 3 Cylinder-disk view factors.

The integration in Eq. (1) is given by

$$2\pi F_{1-2} = \cos^{-1} \frac{l^2 - R^2 + r^2}{l^2 + R^2 - r^2} - \left(\frac{r}{2l} \right) \left[\left[\frac{(l^2 + R^2 + r^2)^2}{r^4} - 4 \left(\frac{R}{r} \right)^2 \right]^{1/2} \times \cos^{-1} \frac{r(l^2 - R^2 + r^2)}{R(l^2 + R^2 - r^2)} + \left[\frac{l^2 - R^2 + r^2}{r^2} \right] \sin^{-1} \left(\frac{r}{R} \right) - (\pi/2) \left[\frac{l^2 + R^2 - r^2}{r^2} \right] \right] \quad (2)$$

The cylinder-disk view factor F_{1-2} given by Eq. (2) is presented in parametric form in Fig. 3.

The view factors F_{1-3} for the various structures in Fig. 1 are presented in the following. The derivation for configuration I is shown in some detail to illustrate the procedure. In all cases L is the length of the inner cylinder and Y is the

length of the outer cylinder. Other dimensions are shown in Fig. 1.

Configuration I

Again, by definition³ and referring to Fig. 1

$$L F_{1-3} = \int_0^L F_{d1-3} dy \quad (3)$$

By introducing appropriate view factor algebra, Eq. (3) can be written

$$L F_{1-3} = \int_0^A (F_{d1-2} - F_{d1-4}) dy + \int_{A+Y}^L (F_{d1-4} - F_{d1-2}) dy \quad (4)$$

In Fig. 1 and Eq. (4), surfaces 2 and 4 are imaginary annular disks covering the ends of the outer cylinder. A term-by-term comparison of the integrations indicated in Eq. (4) with the cylinder-disk definition, Eq. (1), shows that the solution of Eq. (4) can be written immediately in terms of the cylinder-disk view factors given in Fig. 3 or by Eq. (2). After some algebraic manipulation

$$L F_{1-3} = Y + A F_A + B F_B - (A + Y) F_{(A+Y)} - (B + Y) F_{(B+Y)} \quad (5)$$

A view factor shorthand notation is used in Eq. (5) and below where, for instance, F_A is the cylinder-disk view factor F_{1-2} with $t/r = A/r$.

Configuration II

$$L F_{1-3} = A F_A + a(I - F_a) + (Y - a) F_{(Y-a)} - (A + Y) F_{(A+Y)} \quad (6)$$

Configuration III

$$L F_{1-3} = L + b F_b + c F_c - (L + b) F_{(L+b)} - (L + c) F_{(L+c)} \quad (7)$$

Configuration IV

$$L F_{1-3} = (L + D) F_{(L+D)} + (Y + D) F_{(Y+D)} - D F_D - (L + D + Y) F_{(L+D+Y)} \quad (8)$$

Discussion

A quick check on the validity of the previous equations can be obtained by examining some limiting cases. Configurations I and III reduce to the identical result when $A = B = b = c = 0$ in which case both Eqs. (5) and (7) give $F_{1-3} = 1 - 2 F_L$, the equal-length concentric cylinder case. Equations (5) and (6) agree when $B = 0$ and $a = Y$ as do Eqs. (6) and (8) with $a = D = 0$. Also, Eq. (8) agrees with results computed in Ref. 1.

Any of the view factors given by Eqs. (5-8) can quickly be determined by reading the cylinder-disk factors from Fig. 3. Comparisons with computer programmed results for several of the configurations have indicated that 2-significant-figure accuracy or better can be obtained consistently using Fig. 3 plotted on graph paper. The technique presented here is also applicable to a concentric inner cylinder and outer truncated cone with slight modification.

References

- Reid, R. L. and Tennant, J. S., "Annular Ring View Factors," *AIChE Journal*, Vol. 11, Oct. 1973, pp. 1446-1448.
- Siegel, R. and Howell, J. R., *Thermal Radiation Heat Transfer*, McGraw-Hill, New York, 1972, Appendix C.
- Siegel, R. and Howell, J. R., *Thermal Radiation Heat Transfer*, McGraw-Hill, New York, 1972, p. 187.
- Leuenberger, H. and Person, R. A., "Compilation of Radiation Shape Factors for Cylindrical Assemblies," ASME Paper 56-A-144, 1956.

ORIGINAL PAGE IS
OF POOR QUALITY

APPENDIX D

MULTIBLADE SAWING RATES WITH CRYSTAL ROTATION

Total elapsed cutting time in multiblade slurry sawing is proportional to relative travel between the blades and workpiece. The faster the blades move relative to the workpiece, the higher the cutting rate and the lower the saw cycle time. The Varian multiblade saw head is limited to a maximum blade speed of about 68 cm/s and little can be done to increase the blade head reciprocation rate due both to inherent mechanical problems in accelerating the massive head (100 kg) and to saw vibration problems at high reciprocation rates. The only alternative for significantly increasing relative blade speed is to rotate the crystal. At 500 rpm, the peripheral speed of a 12-cm crystal is 314 cm/s which is almost eight times a typical blade speed of 40 cm/s. Thus, crystal rotation should enhance the cutting rate thereby reducing saw cycle time.

Let the blade head reciprocation rate be denoted by ω_b (cycles/min), the crystal spin rate by ω_s (rpm), and the blade stroke by d (cm). There exists a critical radius, r_o , below which crystal spin will produce no net beneficial effect due to cancellation of relative blade motion each half cycle. This critical radius is:

$$r_o = (\omega_b / \omega_s) d / \pi \quad (1)$$

As an example, assume the blade head reciprocation rate is 60 cycles/min, the crystal is spinning at 500 rpm, and blade stroke length is 20 cm. Then, from Eq. (1):

$$r_o = (60/500) (20) / \pi = 0.76 \text{ cm}$$

In general, r_o is fairly small indicating that crystal spinning is beneficial over most of the crystal radius. Once the cutting radius reaches r_o , the crystal rotation should be stopped and the remaining core sawed through with the crystal stationary.

For each complete blade head cycle, the relative blade travel ΔT is given by:

$$\Delta T = (\pi r \omega_s + \omega_b d) \tau + \pi r \omega_s - \omega_b d \tau \quad (2)$$

where r is the instantaneous cutting radius and τ is the blade head period equal to $1/\omega_b$. Equation (2) is of interest only for $r > r_0$ and can be simplified to:

$$\Delta T = 2\pi r (\omega_s/\omega_b) \quad (3)$$

Now, define:

$$r = R - bT \quad (4)$$

where R is the crystal outer radius and b is a constant of proportionality determined from static sawing experiments:

$$b = c/2\omega_b d \quad (5)$$

In Eq. (5), c is the empirically determined static cutting rate in mm/h, mm/min, or any other consistent units to make b in Eq. (5) dimensionless. Typical values of c are in the range 5 to 12 mm/h, depending on many factors such as blade force, abrasive, grit size, slurry mixture, slurry flow rate, etc.

In the limit, Eq. (3) can be written in differential form:

$$dT/dn = 2\pi (R - bT) (\omega_s/\omega_b) \quad (6)$$

where n is the number of blade head cycles and Eq. (4) has been substituted for r in Eq. (3). Equation (6) can be integrated to give the number of cycles n_0 for the blades to move into the crystal to radius r_0 at which point the crystal spin is turned off:

$$n_0 = \frac{1}{2\pi b} \left(\frac{\omega_b}{\omega_s} \right) \ln \left[\frac{\pi R}{d} \left(\frac{\omega_s}{\omega_b} \right) \right] \quad (7)$$

The time t_0 required for n_0 blade cycles is simply:

$$t_0 = n_0/\omega_b \quad (8)$$

and the total time t to saw through the crystal is:

$$t = t_0 + 2 r_0/c \quad (9)$$

ORIGINAL PAGE IS
OF POOR QUALITY

or, using Eqs. (7) and (8) in Eq. (9) with r_0 given by Eq. (1):

$$t = \frac{d}{\pi c} \left(\frac{\omega_b}{\omega_s} \right) \left[\ln \left(\frac{\pi R}{d} \frac{\omega_s}{\omega_d} \right) + 2 \right] \quad (10)$$

In nondimensional form, Eq. (10) can be written

$$\frac{\pi c t}{d} = \left(\frac{\omega_b}{\omega_s} \right) \left[\ln \left[\frac{\pi R}{d} \frac{1}{(\omega_b/\omega_s)} \right] + 2 \right] \quad (11)$$

Equation (11) is shown plotted in Figure D-1.

As an example, let $R = 6$ cm, $d = 15$ cm, $\omega_b = 60$ cycles/min, $\omega_s = 500$ rpm. Then from Eq. (11)

$$\pi c t / d = 0.303$$

With $c = 5$ mm/h, a value obtainable with either SiC or B_4C abrasive,

$$t = (0.303) (15) / \pi (0.5) = 2.9 \text{ h}$$

Without crystal spinning, the cutting time would be given by:

$$t (\text{no spin}) = 12 \text{ cm} / 0.5 \text{ cm/h} = 24 \text{ h}$$

Thus, in this contrived example, crystal spinning would reduce the cutting time by a factor of 8.

It should be noted that Eq. (1) defines the minimum crystal rpm for spinning to be effective. By letting $r_0 = R$, for spinning to offer an advantage,

$$(\omega_s / \omega_b) > \frac{d}{\pi R} \quad (12)$$

Equation (12) defines the plateaus in Figure D-1.

Figure D-2 compares some experimental cutting rates with crystal spin to stationary crystal rates. Improvements in cutting speed of 3 to 5 times over those of stationary crystals are indicated in Figure D-2 in general agreement with the theory presented here.

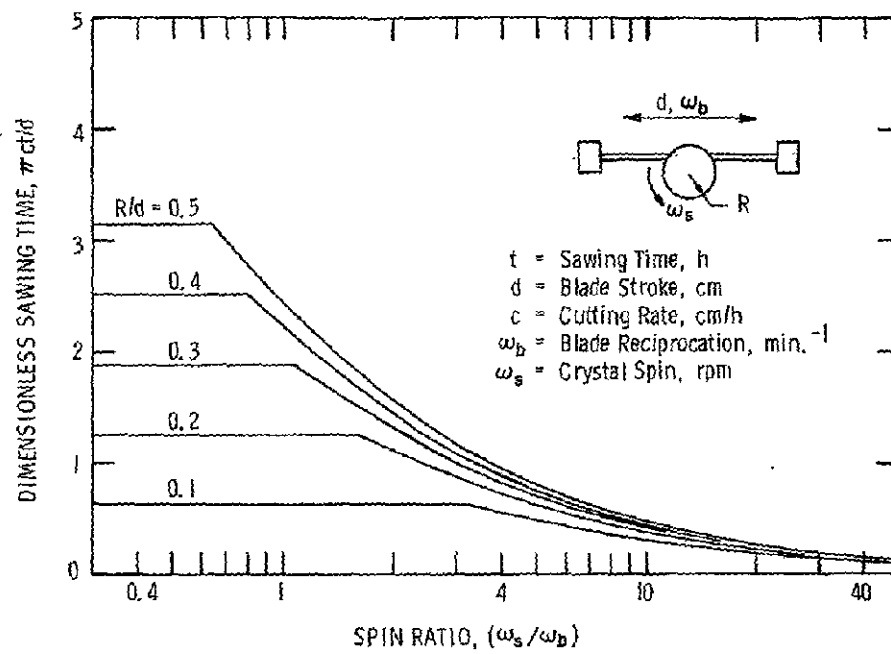


Figure D-1. Theoretical Effect of Crystal Spin-on Sawing Time

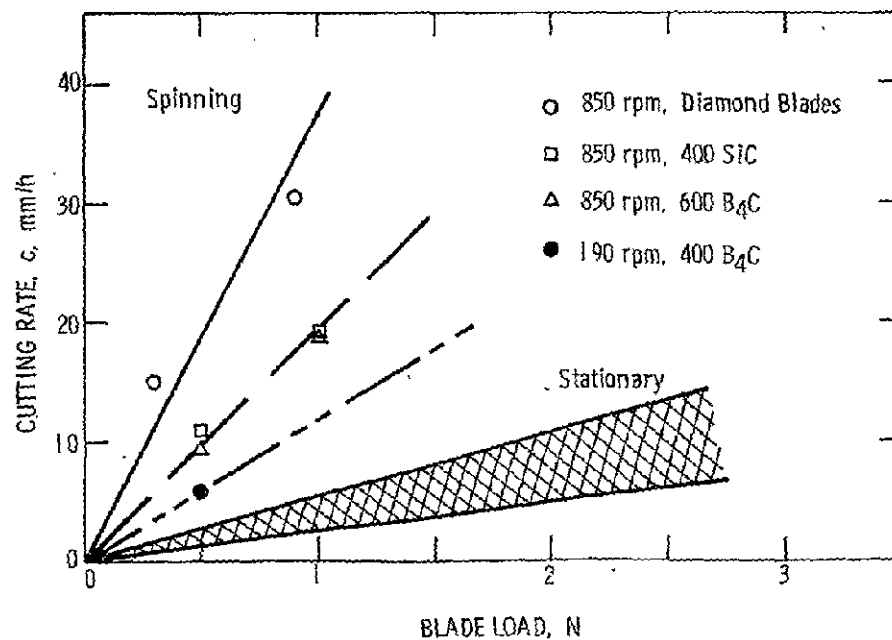


Figure D-2. Multiblade Saw Silicon Cutting Rates

APPENDIX E

SAW BLADE MECHANICAL PROPERTIES

The standard blades for the Varian multiblade saw are made from hardened 1095 steel. Knoop hardness and stress-strain measurements were made to characterize the mechanical properties of the blades.

A. KNOOP HARDNESS

Knoop hardness was measured on five different blade samples. Results were:

$$\text{Knoop hardness} = 618 \pm 21.$$

For comparison, Knoop values for other materials of interest are:

Silicon	1000
SiC	2470
B ₄ C	2750
Diamond	7000

B. TENSILE TESTS

Twelve different blade samples were tested on an Instron testing machine. Ultimate strength, Young's modulus, and yield strength of the blades were determined. Results were:

$$\text{ultimate strength} = 1.90 \pm 0.07 \text{ GPa} (275,000 \pm 10,000 \text{ psi})$$

$$\text{Young's modulus} = 190 \pm 7 \text{ GPa} (27.5 \pm 1.0 \times 10^6 \text{ psi})$$

$$\text{yield strength} = 1.72 \text{ GPa} (249,000 \text{ psi})$$

Figure E-1 shows a typical stress-strain curve measured for the hardened 1095 steel blades. The curve is characteristic of a hard steel in that there is a pronounced knee with no peak, ultimate strength is only slightly greater than the yield point, and there is little plastic deformation before breaking.

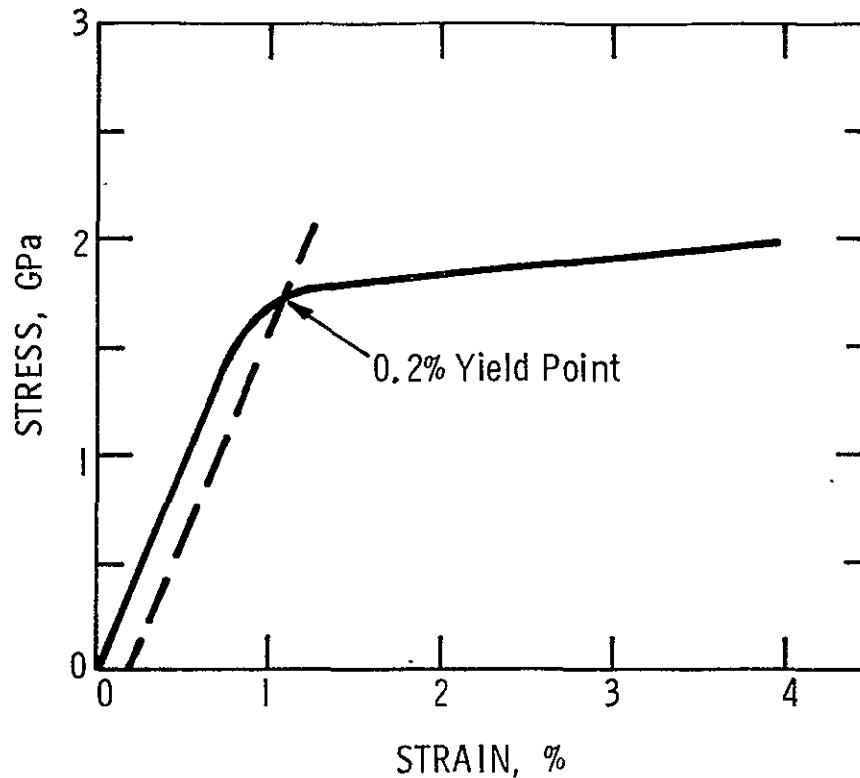


Figure E-1. Typical Measured Stress-Strain Curve of Hardened 1095 Steel Saw Blades

In practice, blades are usually tensioned to a 0.7% strain. Figure E-1 indicates that at this strain the blade stress is 1.35 GPa (197,000 psi). At this stress level the force exerted by each blade on the blade head is 1780 N (400 lb) depending on blade dimensions. Consequently, if the blade head contains 500 blades, a sizable force on the order of 8.8×10^5 N (200,000 lb) would be exerted on the head. The present Varian head is not designed to carry a load of this magnitude and redesign is necessary to provide the required strength to carry a large number of blades.

It has been assumed in economic modeling that the multiblade saw could be extended to handle 28-cm long crystal sections. A slice plus kerf thickness of 0.5 mm would result in 560 blades in the head. The tensioning force for this extended blade head could be in the neighborhood of 10^6 N (224,000 lb) and careful consideration of the head design would be required to handle this load.

C. BLADE STATIC DEFLECTION

The saw blades can be approximated as thin rectangular beams having fixed ends. Figure E-2 represents a blade loaded at the midpoint which is the location of maximum deflection. The deflection y at location x is governed by the differential equation:

$$EI y'' = M + Ty - P/2 x \quad (1)$$

with boundary conditions

$$x = 0: \quad y = y' = 0 \quad (2)$$

$$x = L/2: \quad y' = 0 \quad (3)$$

The solution to this set of equations for the midspan deflection is.

$$y_{\max} = \frac{PL^3}{192 EI} \left[\frac{12 (2 - 2 \cosh u + u \sinh u)}{u^3 \sinh u} \right] \quad (4)$$

where

$$u = (L/2) \sqrt{T/EI} \quad (5)$$

and

I = moment of inertia of the blade about the flexure axis

= $th^3/12$ for vertical loads

= $ht^3/12$ for lateral loads

E = Young's modulus.

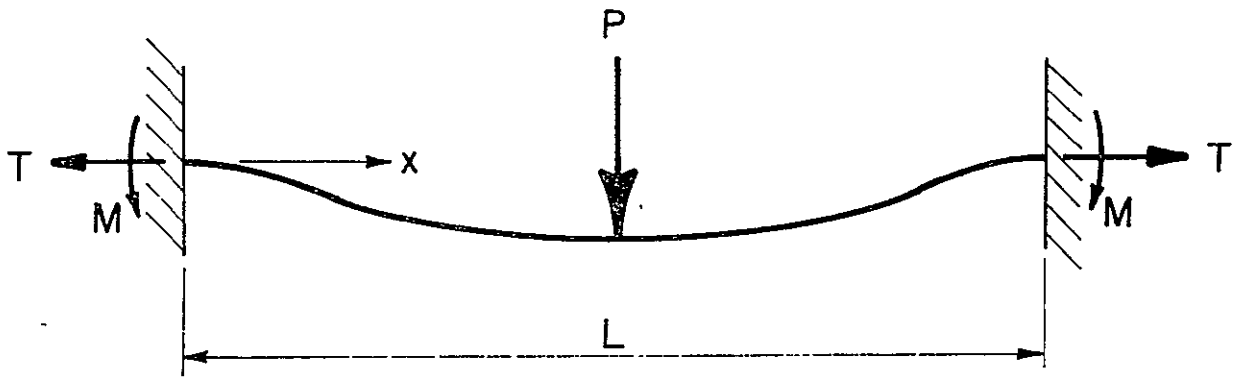


Figure E-2. Fixed-End Beam with Axial Tension

If $u = 0$ (no axial tension) Eq. (4) reduces to the usual fixed-end beam equation with the bracketed term in Eq. (4) equal to one. For u infinitely large, y_{\max} approaches zero. With the usual 1.35 GPa axial stress and 0.20 X 6.35 mm blades, u for the vertical direction is 8.8 and the bracketed term in Eq. (4) equals 0.12. The maximum deflection in this case with a 2 N blade load is 0.08 mm.

APPENDIX F

PULLER HOT ZONE COSTS

Table F-1 lists major parts used in a Varian 12-kg puller hot zone. Many of the parts are graphite and their costs fluctuate from one buy to the next so the costs shown are approximate only. The number of furnace runs are estimated or observed based on experience in single-charge pulls of 12-cm crystals. It is somewhat difficult to extrapolate this experience to multicharge runs, however, it is believed that multicharge costs would not be significantly higher than those shown. The lifetime of many of the items in Table F-1 is governed by breakage incurred in the removal or replacement necessitated by cleaning after each run. Also, the structural integrity of some of the graphite parts is affected by repeated heating cycles so that a multicharge run in which the hot zone stays hot for an extended period should not degrade the structural soundness any faster than single-charge runs. It is estimated that multicharge or semicontinuous runs would be about 30% higher than the costs shown in the table. Thus, in the economic models the following miscellaneous parts costs were used:

Single charge:	\$54/run
Multicharge:	\$70/run
Semicontinuous:	\$70/run

Of the costs listed in Table F-1, four items: crucible shaft, crucible top, heater, and vacuum pump filters make up almost 60% of the total. Provided adequate water flow is maintained to the crucible shaft and no spills occur, it should last indefinitely. Thus, the \$9/run for this item could be conservative. The crucible top is a fragile graphite part which is easily broken during use from careless handling and expansion of the crucible liner against the crucible top enlarges it with each run so that it eventually becomes oversize and must be discarded. There is no obvious way to reduce this part cost. The heater is a fairly complex machined graphite structure which slowly degrades with use and is subject to breakage from handling. The \$10/run cost is a reasonable estimate based on experience. The current vacuum pump filters are inadequate for the volume of gases and particulates handled per run. A redesign of the filter holder to utilize larger filters could effect some cost reduction, perhaps as much as 50%.

Overall, an aggressive cost-cutting campaign which would involve some redesign and puller hot zone modifications could effect at least a 15% reduction in the miscellaneous parts costs.

Table F-1. 12-kg Puller Miscellaneous Parts Costs

	Part (Quantity)	Cost	No. Runs	Cost/Run
1.	Crucible shaft	\$900	100	\$9.00
2.	Pedestal plate	48	20	2.40
3.	Pedestal insulator	42	50	0.84
4.	Crucible bottom	56	25	2.24
5.	Crucible top	72	8	9.00
6.	Seed holder	25	50	0.50
7.	Seed clamp screw	3	20	0.15
8.	Seed shaft	600	600	1.00
9.	Heater connectors (3)	7	50	0.14
10.	Heater adapters (3)	48	50	0.96
11.	Graphite units (3)	10	40	0.25
12.	Heater screws (6)	9	10	0.90
13.	Heater	250	25	10.00
14.	Graphite heat shield	200	75	2.67
15.	Graphite felt insulation	150	50	3.00
16.	Heat shield top	28	75	0.37
17.	Shield support rings (2)	56	30	1.87
18.	Outer stainless reflector	200	100	2.00
19.	Shield reflector rings (2)	75	75	1.00
20.	Shaft seals (4)	20	20	1.00
21.	Vacuum pump filters	9	3	3.00
22.	Vacuum pump oil	15	10	1.50
Total.				\$53.79/run

ORIGINAL PAGE IS
OF POOR QUALITY

APPENDIX G

CRYSTAL GROWTH POWER REQUIREMENTS

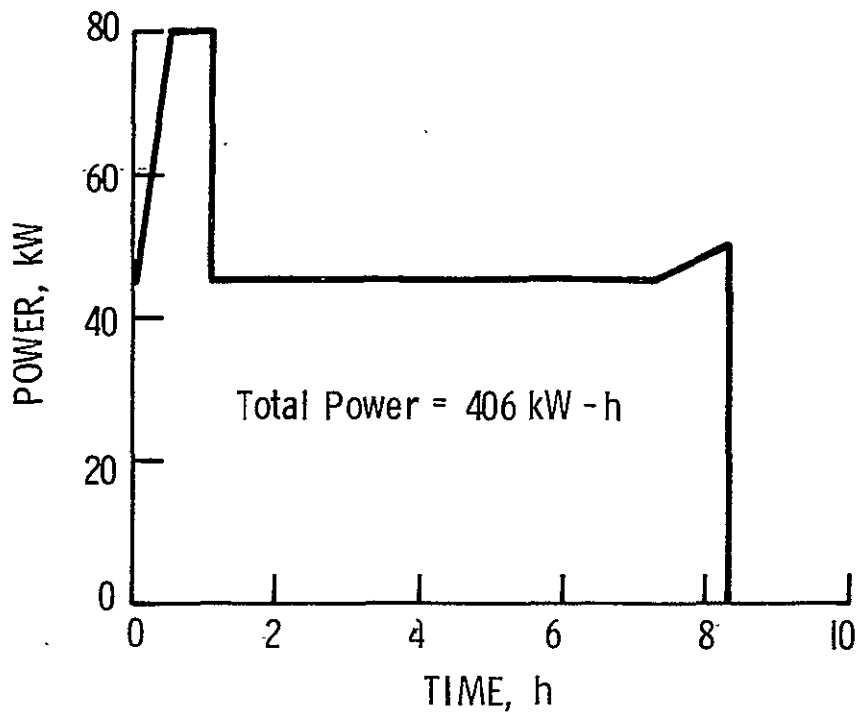
Power consumption measured in the 12-cm runs conducted during this investigation was used as a basis for estimating puller power for the various economic models presented in Section II.E. Figures G-1 and G-2 depict idealized cycle power for four cases. Figure G-1(a) corresponds to the experimental single-charge pulls performed using a 12-kg crucible. The other cases assume 18-kg crucibles.

Full power is not applied instantaneously when a puller is turned on but is ramped up over a 30-min interval. This procedure minimizes problems associated with differential thermal expansions between the various hot zone components and is believed to prolong the lives of the components. Once the polysilicon is fully melted, the power is reduced abruptly to its nominal running value, 45 kW, and the melt temperature is allowed to stabilize. During the pull, the power fluctuates about this average but these fluctuations are ignored in the idealized power curves. In the bottom taper operation the melt temperature is increased as is the pull rate and this is the reason for the small ramps in the figures. The power curves are only approximate and assume no melt-backs are required. Melt-backs can increase the total power requirements by 20-30%.

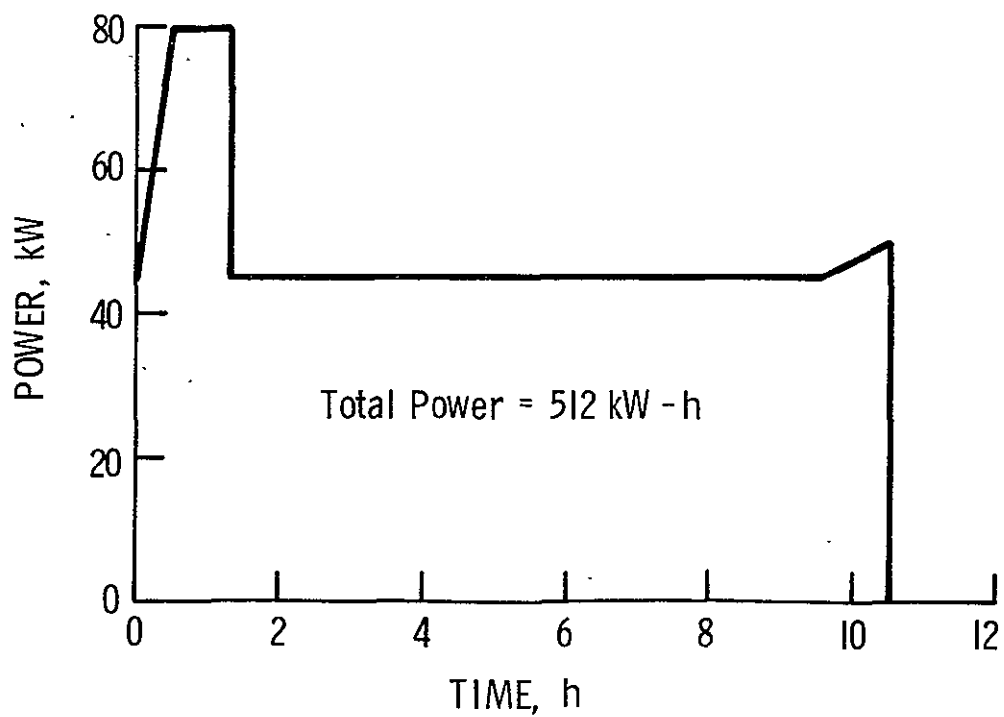
It is of some interest to estimate the energy payback of the crystal growth portion of the total solar cell process. Assume:

- 1) Daily insolation = 5 kW-h/m²
- 2) Crystal growth yield = 85%
- 3) Sawing yield = 95%
- 4) Slice + kerf = 0.56 mm
- 5) Solar cell efficiency = 13%

These assumptions along with the energy consumptions in Figures G-1 and G-2 result in the paybacks in Table G-1. The payback for the single charge 56-cm length is the same as that for the multicharge (3 X 56 cm = 168 cm) case. This indicates that longer crystals should be grown in a multicharge pull to decrease the high-power dead time occurring during taper, charge, melt, and crystal removal. Crystal costs are, of course, advantageous for multicharge operation because of the increased puller, liner, and materials utilization. These factors greatly outweigh the energy cost.

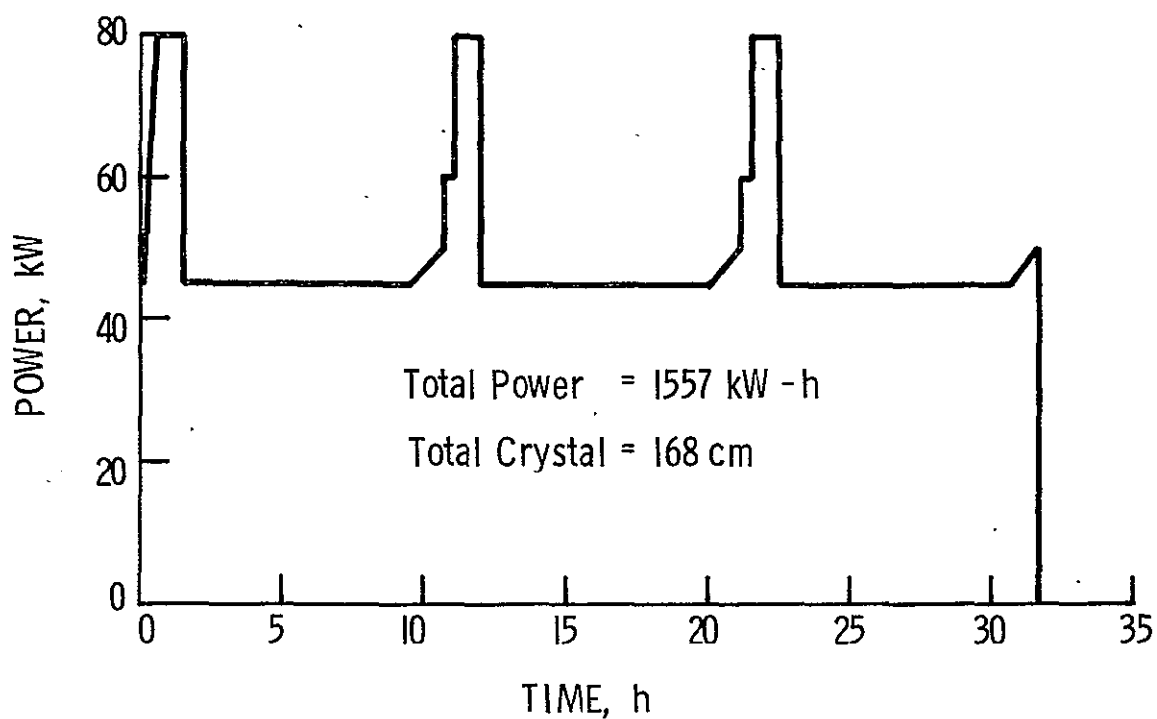


(a) 11.6-kg Single Charge, 38-cm Crystal

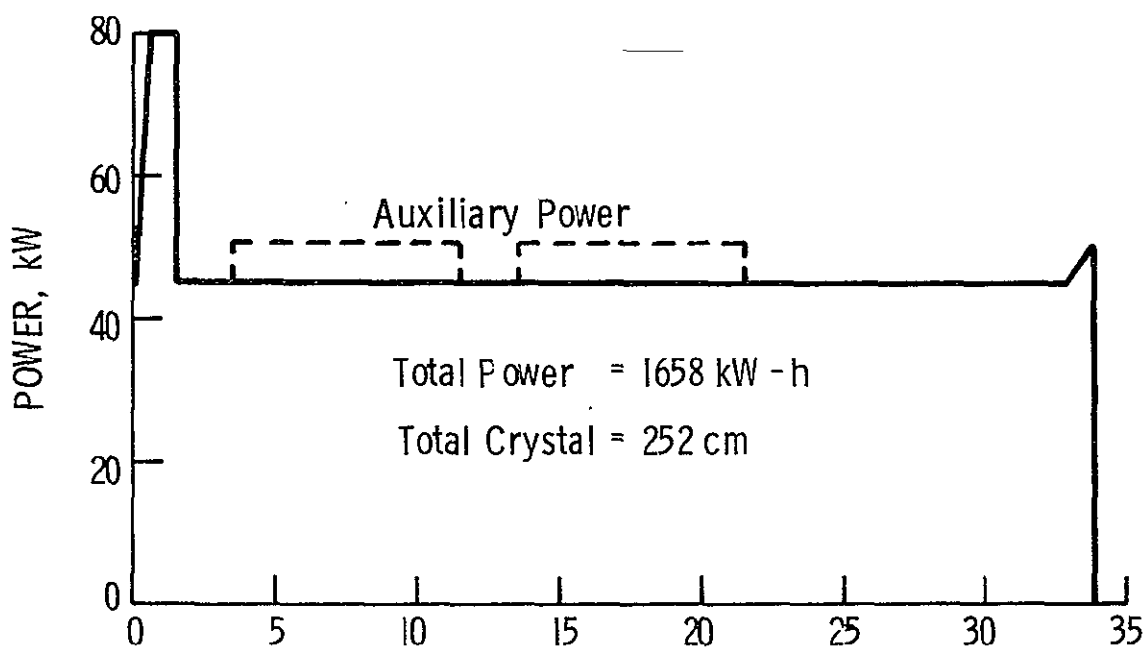


(b) 16.3-kg Single Charge, 56-cm Crystal

Figure G-1. 12-cm Diameter Crystal Growth Power Requirements



(a) Multicharge Run - 3 Crystals



(b) Semicontinuous Run - 3 Crystals

Figure G-2. 12-cm Diameter Crystal Growth Power Requirements

Table G-1. Crystal Growth Energy Payback Periods

Growth Mode	Payback
1. Single charge, 38 cm	101 days
2. Single charge, 56 cm	86
3. Multicharge, 168 cm	87
4. Semicontinuous, 252 cm	62

The auxiliary power indicated in Figure G-2(b) is that required to melt sufficient polysilicon to maintain constant melt level. The exact amount of auxiliary power necessary is highly dependent on semicontinuous puller design and cannot be determined precisely at this time. For estimation purposes, auxiliary power was assumed to be four times the energy necessary to melt 44.46 kg of silicon, the combined weight of the first two crystals.

APPENDIX H

SELECTED METRIC CONVERSION FACTORS

With a few minor exceptions, all units in this report conform to the SI measurement system. An excellent guide to the SI system is standard ANSI/ASTM E380-76. Listed below are a few of the more unusual conversions encountered during the course of this investigation. In these conversions, to obtain the SI units on the left, perform the operation indicated on the right side of the equality.

Force

$$\begin{aligned}\text{Newtons (N)} &= \text{grams}/101.97 \\ \text{Newtons (N)} &= (\text{pounds}) \times (4.4482)\end{aligned}$$

Pressure or Stress

ORIGINAL PAGE IS
OF POOR QUALITY

$$\begin{aligned}\text{Pascal (Pa)} &= \text{N}/\text{m}^2 \\ \text{Pascals (Pa)} &= (\text{atm}) \times (1.0133\text{E}05) \\ \text{Pascals (Pa)} &= (\text{mm Hg}) \times (133.32) \\ \text{Pascals (Pa)} &= (\text{psi}) \times (6894.8)\end{aligned}$$

The Pascal is a very small unit so it is common to use mega- or giga-Pascals. Thus, 1 atmosphere = 0.1 MPa.

Specific Heat

$$\begin{aligned}\text{J/kg-K} &= (\text{cal/g-}^\circ\text{C}) \times (4184) \\ \text{W-s/g-K} &= (\text{cal/g-}^\circ\text{C}) \times (4.184)\end{aligned}$$

Thermal Conductivity

$$\begin{aligned}\text{W/cm-K} &= (\text{cal/s-cm-}^\circ\text{C}) \times (4.184) \\ \text{W/cm-K} &= (\text{BTU/h-ft-}^\circ\text{F}) \times (0.017307)\end{aligned}$$

Viscosity

$$\text{Pa-s} = (\text{centipoise}) \times (1.0\text{E-}03)$$